INFORMATION TO USERS

This manuscript has been reproduced from the microfilm master. UMI films the text directly from the original or copy submitted. Thus, some thesis and dissertation copies are in typewriter face, while others may be from any type of computer printer.

The quality of this reproduction is dependent upon the quality of the copy submitted. Broken or indistinct print, colored or poor quality illustrations and photographs, print bleedthrough, substandard margins, and improper alignment can adversely affect reproduction.

In the unlikely event that the author did not send UMI a complete manuscript and there are missing pages, these will be noted. Also, if unauthorized copyright material had to be removed, a note will indicate the deletion.

Oversize materials (e.g., maps, drawings, charts) are reproduced by sectioning the original, beginning at the upper left-hand corner and continuing from left to right in equal sections with small overlaps.

Photographs included in the original manuscript have been reproduced xerographically in this copy. Higher quality 6" x 9" black and white photographic prints are available for any photographs or illustrations appearing in this copy for an additional charge. Contact UMI directly to order.

ProQuest Information and Learning
300 North Zeeb Road, Ann Arbor, MI 48106-1346 USA
800-521-0600

Medical Ultrasound Algorithm for Noninvasive High Intensity Ultrasound Applications

Francesco Pasquale Curra

A dissertation submitted in partial fulfillment of the requirements for the degree of

Doctor of Philosophy

University of Washington

2001

Program Authorized to Offer Degree: Bioengineering

In presenting this dissertation in partial fulfillment of the requirements for the Doctoral degree at the University of Washington, I agree that the Library shall make its copies freely available for inspection. I further agree that extensive copying of the dissertation is allowable only for scholarly purposes, consistent with "fair use" as prescribed in the U.S. Copyright Law. Requests for copying or reproduction of this dissertation may be referred to Bell and Howell Information and Learning, 300 North Zeeb Road, Ann Arbour, MI 48106-1346, to whom the author has granted "the right to reproduce and sell (a) copies of the manuscript in microfilm form and/or (b) printed copies of the manuscript made from microfilm."

Signature 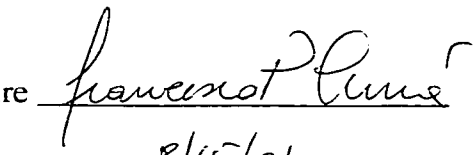

Date 8/15/01

University of Washington
Graduate School

This is to certify that I have examined this copy of a doctoral dissertation by

Francesco Pasquale Curra

And I have found that it is complete and satisfactory in all respects,
and that any and all revisions required by the final
examining committee have been made.

Chair of Supervisory Committee:

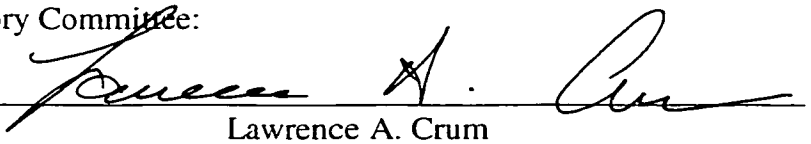

Lawrence A. Crum

Reading Committee:

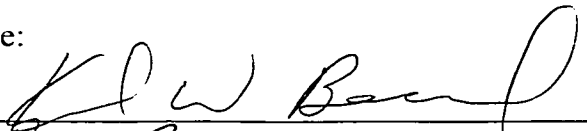

Kirk W. Beach

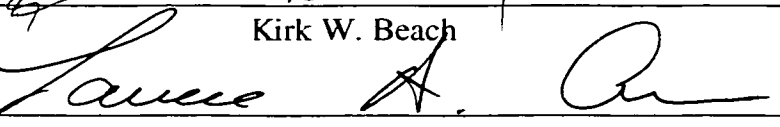

Lawrence A. Crum

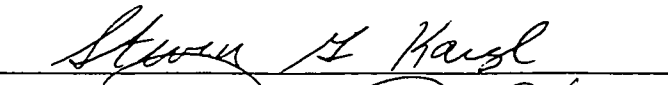

Steven G. Karg

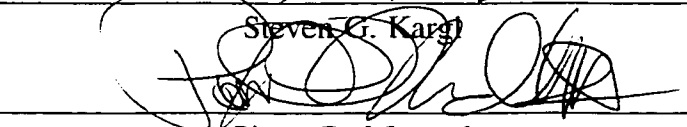

Pierre D. Mourad

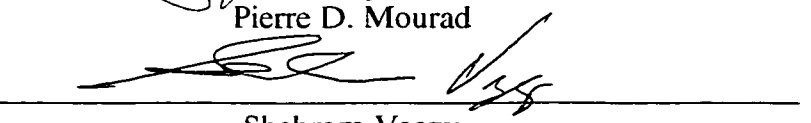

Shahram Vaezy

Date : August 6, 2001

University of Washington

Abstract

Medical Ultrasound Algorithm for Noninvasive High Intensity Ultrasound Applications.

Francesco P. Curra

Chair of Supervisory Committee:
Professor Lawrence A. Crum
Bioengineering

In order to simulate ultrasound propagation and subsequent thermal effects in biological media in which blood vessels and other structures may be present, a 3-dimensional model has been developed that eliminates the need for symmetry constraints.

The model is based on the coupled solution of the full-wave nonlinear equation of sound in a lossy medium with the bioheat equation for tempearture predictions. The algorithm includes nonlinear sound propagation, arbitrary frequency power laws for attenuation, is capable of treating material inhomogeneities and explicit modeling of large blood vessels. Unlike other models based on parabolic approximations, it is not restricted to near-axis solutions and can account for reflection and backscattered fields. The software is validated against known analytical solutions and *in vitro* experimental results in turkey breast. Very good agreement is found between experimental measurements and numerical prediction.

Table of Contents

List of Figures

List of Tables

Acknowledgements

I wish to thank Professor Lawrence A. Crum for his guidance, support, and dedication during the past five years. If I am at this point today, rather than few years down the road I owe it to you. Thank you for keeping me focused. I am also grateful to Dr. Pierre D. Mourad for introducing me to the field of numerical modeling and for his insights and suggestions along the way. I am greatly indebted to Dr. Steven G. Kargl for his time and dedication in helping me understand the physics of nonlinear acoustics. I would like to thank Drs. Robin O. Cleveland, Vera A. Khokhlova, and Oleg Sapozhnikov. I enjoyed the time spent with you and I will treasure your teachings. A special thank you goes to Drs. Peter Kaczkowski and Cyril Lafon for allowing me to use their experimental setup and for actively helping me with the experiments. I am also grateful to Drs. Kirk W. Beach and Shahram Vaezy for sharing ideas, suggestions and enthusiasm during the past years. I would also like to acknowledge the Office of Naval Research and the Defense Advanced Research Project Agency for funding this project, the Center for Industrial and Medical Ultrasound group for valuable discussions and insights. Finally, I would like to warmly thank my family, the only true fixed point in my universe. Although geographically far away, their support and encouragement were always there.

July, 2001

Dedication

ad maiorem dei gloriam

CHAPTER 1

Introduction

The objective of the research in this dissertation is to theoretically investigate the propagation and the absorption of finite-amplitude sound in dissipative media such as biological media and in particular soft tissue. This research is motivated by the need to better understand the physical processes that take place during exposure to high intensity focused ultrasound (HIFU) in biomedical applications and to develop a software tool for broad investigations of HIFU applications and treatment planning. Although the major intended application is in medicine for diagnosis, hyperthermia, noninvasive surgery, and acoustic hemostasis, the results of the research are general and could be applied as well in other areas; for example, underwater acoustics and ocean acoustics.

By using a focused ultrasonic beam, intense mechanical energy is delivered to a small region of tissue with little or no effect to the surrounding areas. Here absorption processes raise the tissue temperature to relatively high values causing thermal coagulation and ablation of cells. In order to predict and quantify tissue response to focused ultrasound it is important to take into consideration the specific behavior of sound waves and heat transfer as well as the particular characteristics of the biological structures contained in the region of interest.

When ultrasonic transducers are driven to produce high focal intensities in tissue the acoustic wave is, in many cases, influenced by nonlinear propagation (Carstensen *et al*, 1982, Swindel, 1985; Hynynen, 1987; Bacon and Carstensen, 1989; Christopher and

Carstensen, 1996). At finite-amplitudes, the local sound speed becomes "supersonic" during the compression phase of the wave and "subsonic" during the rarefaction phase and the finite-amplitude wave is distorted as it propagates generating higher frequency components. The appearance of higher harmonics has a direct effect on the amount of energy that is absorbed by the tissue, especially in the focal area. In this respect, it has been a well-known experimental fact that the small-signal absorption coefficient of tissue roughly follows the power law $\alpha_0(\omega) \propto \omega^b$, where b ranges from 1.0 to 1.4 in the frequency range from 1 to 10 MHz (Goss et al., 1978; Frizzell et al., 1979; Lyon and Parker, 1988).

Biological systems are also composed by many structures with differing acoustic and thermal characteristics and their response to ultrasound can influence the way the acoustic wave is propagated and absorbed. The geometry of tissue layers, for instance, will induce reflections and scattering at their interfaces or might focus or defocus the sound if the layers have curvature. Blood, on the other hand, is a poor absorber of ultrasound; it can constitute an excellent sink of heat from surrounding tissue and also, because of flow, can convect the heat away.

There exist a number of theoretical and numerical approaches for the modeling of wave propagation (Christopher and Parker, 1991; Lee and Hamilton, 1995;Jensen, 1996). Each of those methods, however, implies some sort of approximation in the behavior of the sound field and can be applied only for problems of specified characteristics. For instance: the methods of Christopher and Parker, based on the spatial impulse response

convoluted with a modified Hankel transform, cannot account for multiple reflections; the KZK-based time domain code of Lee and Hamilton is developed for progressive quasi-plane waves and restricted to a limited diffraction angle from the symmetry axis; and the code by Jensen only models linear acoustic propagation.

Similarly for the prediction of temperature dynamics, in most previous models the effect of blood perfusion on heat transfer in the bioheat equation is accounted for by adding a relaxation term that removes heat uniformly throughout the tissue (Nyborg, 1988; Baish, 1992). The amount of heat removed is determined by averaging the effect of blood perfusion over all the tissue, that is, the localized effect of single vessels is neglected. This "homogenization" of perfusion is probably appropriate for tissue that consists of extended capillary beds, however, it is not valid when the dimension of the blood vessel is of the same order of the focal spot of the ultrasound beam.

In this document we present the development of a numerical scheme for the solution of the propagation of ultrasound and its related temperature effects in a general 2-D and 3-D domain. The model includes nonlinear acoustic propagation, inhomogeneous media, frequency dependent attenuation laws, heat generation and transfer, and explicit modeling of large blood vessels.

CHAPTER 2

Derivation of the Nonlinear Wave Equation[1]

In this chapter, the basic equations for the propagation of finite-amplitude acoustic waves in media with frequency-dependent multiple relaxation losses are presented. We start our approach by presenting the derivation of the governing equations for a lossless fluid[2] in Sec 2.1-2.3. Attenuation losses are then introduced and discussed in Sec. 2.4 by means of relaxation mechanisms. The treatment of the frequency-dependent behavior of the media, in Sec. 2.5, concludes the chapter.

2.1 Basic equations in a lossless fluid

The propagation of sound waves in a lossless fluid is governed by Euler's equations, which express the conservation of mass (continuity equation) and the transfer of momentum (momentum equation) in a fluid volume, together with a thermodynamic equation of state (Pierce, 1989). The continuity equation is

$$\frac{D\rho}{Dt} + \rho\nabla \cdot \mathbf{v} = 0 \tag{2.1}$$

the momentum equation is

$$\rho\frac{D\mathbf{v}}{Dt} + \nabla P = 0 \tag{2.2}$$

1The discussion is based on Pierce (1989) Chap. 1 and Blackstock and Hamilton (1998) Chap. 2-3 to which the reader is referred for a wider and more detailed treatment of the subject.

2 Tissue is commonly modeled as a fluid for sound propagation.

and the equation of state is

$$P = P(\rho, s) \tag{2.3}$$

where ρ is the mass density, $\mathbf{v}$ is the fluid's particle velocity, P is the thermodynamic pressure in terms of density and entropy (s), and $\frac{D}{Dt} = \frac{\partial}{\partial t} + \mathbf{v} \cdot \nabla$ is the total or material time derivative. Equations 2.2 and 2.3 can be written explicitly as

$$\frac{\partial \rho}{\partial t} + (\mathbf{v} \cdot \nabla)\rho + \rho \nabla \cdot \mathbf{v} = 0 \tag{2.4}$$

and

$$\rho \frac{\partial \mathbf{v}}{\partial t} + (\mathbf{v} \cdot \nabla)\mathbf{v} + \nabla P = 0 \tag{2.5}$$

when the material derivative is used.

In general, the equation of state, 2.3, can be expanded in a Taylor series about the ambient values, ρ_0, P_0, and s_0. This yields

$$P - P_0 = \left(\frac{\partial P}{\partial \rho}\right)_{s,0} (\rho - \rho_0) + \frac{1}{2!}\left(\frac{\partial^2 P}{\partial \rho^2}\right)_{s,0} (\rho - \rho_0)^2 + \ldots. \tag{2.6}$$

Equations 2.4-2.6 constitutes a system of three equations in three unknowns (P, ρ and $\mathbf{v}$), which determines the state of the fluid both in space and in time.

In acoustics, we are concerned with the fluctuations of the thermodynamical variables (acoustic disturbances), which are considered to be small compared to their ambient values, around their static (ambient) state. Given this, we can then write, density, pressure, and particle velocity as

$$\rho = \rho_0 + \rho' \tag{2.7}$$

$$P = P_0 + p' \tag{2.8}$$

and

$$\mathbf{v} = \mathbf{v}' \tag{2.9}$$

where acoustic fluctuations have been denoted by the prime superscript and are a function of both space and time, while the corresponding variables in ambient state have been denoted by the subscript zero and are only a function of space. Equations 2.7-2.9 assume that the fluid is in thermal equilibrium and at rest, i.e. $\mathbf{v}_0 = 0$.

Substituting Eqs. 2.7-2.9 into Eqs. 2.4-2.6, we can obtain a system of governing equations of various order. Equations 2.4-2.6 then become

$$\frac{\partial \rho'}{\partial t} + \rho_0 \nabla \cdot \mathbf{v}' + \rho' \nabla \cdot \mathbf{v}' + \mathbf{v}' \cdot \nabla \rho' + \mathbf{v}' \cdot \nabla \rho_0 = 0 \tag{2.10}$$

$$\rho_0 \frac{\partial \mathbf{v}'}{\partial t} + \rho' \frac{\partial \mathbf{v}'}{\partial t} + \frac{1}{2}\rho_0 \nabla \mathbf{v}'^2 + \frac{1}{2}\rho' \nabla \mathbf{v}'^2 - \rho_0 \mathbf{v}' \times \nabla \times \mathbf{v}' - \rho' \mathbf{v}' \times \nabla \times \mathbf{v}' + \nabla P = 0 \tag{2.11}$$

and

$$p' = \left(\frac{\partial P}{\partial \rho}\right)_{s,0} \rho' + \frac{1}{2!}\left(\frac{\partial^2 P}{\partial \rho^2}\right)_{s,0} \rho'^2 + \ldots. \tag{2.12}$$

To arrive at Eq. 2.11, we used the vector identity $(\mathbf{v}' \cdot \nabla)\mathbf{v}' = \frac{1}{2}\nabla \mathbf{v}'^2 - \mathbf{v}' \times \nabla \times \mathbf{v}'$.

Equation 2.12 can also be written in a simpler form as

$$p' = A\frac{\rho'}{\rho_0} + \frac{B}{2!}\left(\frac{\rho'}{\rho_0}\right)^2 + \frac{C}{3!}\left(\frac{\rho'}{\rho_0}\right)^3 + \ldots. \tag{2.13}$$

where

$$A = \rho_0 \left(\frac{\partial P}{\partial \rho} \right)_{s,0} \equiv \rho_0 c_0^2 \tag{2.14}$$

$$B = \rho_0^2 \left(\frac{\partial^2 P}{\partial \rho^2} \right)_{s,0} \tag{2.15}$$

$$C = \rho_0^3 \left(\frac{\partial^3 P}{\partial \rho^3} \right)_{s,0} \tag{2.16}$$

and

$$c_0^2 = \left(\frac{\partial P}{\partial \rho} \right)_{s,0} \tag{2.17}$$

with c_0 denoting the small-signal sound speed.

2.2 Ordering Scheme and Linear Wave Equation

As described in the previous section, fluctuations of the acoustic variables are small compared to their ambient values. In this respect, disturbances due to the acoustic wave p', ρ', and $\mathbf{v}'$ are considered to be of order ε or "first order", $O(\varepsilon)$, where $\varepsilon = \frac{|\mathbf{v}'|}{c_0}$ is the acoustic Mach number and much smaller than one. The adequacy of ε as an ordering parameter is expressed by its value; for example, in water a value of 10^{-2} for ε would correspond to 264 dB (re 1 μPA) or roughly to 200 MPa. Differential changes of the acoustic variables, along with the ambient values, P_0, ρ_0, and c_0, are assumed to be

order one or "zeroth order", $O(1)$. On the other hand, differential changes of ambient values are of order ζ, $O(\zeta)$, where ζ is comparably small to ε and therefore "first order".

In the ordering scheme, the following rule applies to each term: the order of the product of two factors is equal to the algebraic sum of their individual orders; which makes the product of zeroth order terms a zeroth order term, the product of a zeroth order term and a first order term a first order term, the product of first order terms a second order term, and so on.

The lowest order of approximation is order one or linear approximation. By only retaining first order terms in Eqs. 2.10, 2.11, and 2.13 we obtain

$$\frac{\partial \rho'}{\partial t} = -\rho_0 \nabla \cdot \mathbf{v}' \tag{2.18}$$

$$\frac{\partial \mathbf{v}'}{\partial t} = -\frac{1}{\rho_0} \nabla p \tag{2.19}$$

and

$$p' = c_0^2 \rho' \tag{2.20}$$

This system of equations, denoting first order relationships between the acoustic variables, governs the linear propagation of sound waves.

2.3 The Nonlinear Wave Equation

Acoustic nonlinearity is primarily due to the constitutive relationship between pressure and density. Starting from the equations of fluid mechanics Eq. 2.10

(continuity), Eq. 2.11 (momentum), and Eq. 2.13 (equation of state), we only retain terms of up to second order to obtain:

$$\frac{\partial \rho'}{\partial t} + \rho_0 \nabla \cdot \mathbf{v}' + \rho' \nabla \cdot \mathbf{v}' + \mathbf{v}' \cdot \nabla \rho' + \mathbf{v}' \cdot \nabla \rho_0 = 0 \tag{2.21}$$

$$\rho_0 \frac{\partial \mathbf{v}'}{\partial t} + \rho' \frac{\partial \mathbf{v}'}{\partial t} + \frac{1}{2} \rho_0 \nabla \mathbf{v}'^2 - \rho_0 \mathbf{v}' \times \nabla \times \mathbf{v}' + \nabla P = 0 \tag{2.22}$$

and

$$p' = A \frac{\rho'}{\rho_0} + \frac{B}{2!} \left(\frac{\rho'}{\rho_0} \right)^2 \equiv c_0^2 \rho' + \frac{c_0^2}{\rho_0} \frac{B}{2A} \rho'^2 \tag{2.23}$$

where we have used the identity

$$\frac{B}{A} = \frac{\rho_0}{c_0^2} \left(\frac{\partial^2 P}{\partial \rho^2} \right)_{s,0} \tag{2.24}$$

By using Eqs. 2.18-2.20 in the second order terms of Eq. 2.21 and Eq. 2.23 we can eliminate ρ'. The substitution is validated by a fluid mechanic corollary that states that first order acoustic-mode relations may be substituted into any second order term since the resulting errors are of third order. The continuity equation can therefore be rewritten as (Aanonsen et al., 1984)

$$\begin{aligned} \frac{\partial \rho'}{\partial t} + \rho_0 \nabla \cdot \mathbf{v}' &= \frac{p'}{\rho_0 c_0^4} \frac{\partial p'}{\partial t} - \rho_0 \frac{\mathbf{v}'}{c_0^2} \frac{\partial \mathbf{v}'}{\partial t} - \mathbf{v}' \cdot \nabla \rho_0 \\ &= \frac{1}{2 \rho_0 c_0^4} \frac{\partial p'^2}{\partial t} - \frac{\rho_0}{2 c_0^2} \frac{\partial \mathbf{v}'^2}{\partial t} - \mathbf{v}' \cdot \nabla \rho_0 \\ &= \frac{1}{\rho_0 c_0^4} \frac{\partial p'^2}{\partial t} + \frac{1}{c_0^2} \frac{\partial L}{\partial t} - \mathbf{v}' \cdot \nabla \rho_0 \end{aligned} \tag{2.25}$$

and the equation of state as

$$\rho' = \frac{p'}{c_0^2} - \frac{1}{\rho_0 c_0^4}\frac{B}{2A}p'^2 \tag{2.26}$$

The symbol L in Eq. 2.25 is called the Lagrangian density and defined as (*c.f.* Hamilton and Blackstock, 1998, Chapter 3):

$$L = \frac{1}{2}\rho_0 \mathbf{v}'^2 - \frac{1}{2}\frac{p'^2}{\rho_0 c_0^2} \tag{2.27}$$

Substituting the time derivative of Eq. 2.26,

$$\frac{\partial \rho'}{\partial t} = \frac{1}{c_0^2}\frac{\partial p'}{\partial t} - \frac{1}{\rho_0 c_0^4}\frac{B}{2A}\frac{\partial p'^2}{\partial t} \tag{2.28}$$

into Eq. 2.25, the acoustic density can be eliminated in terms of the acoustic pressure fluctuations producing:

$$\kappa\frac{\partial p'}{\partial t} = -\nabla\cdot\mathbf{v}' - \mathbf{v}'\cdot\frac{\nabla\rho_0}{\rho_0} - 2\left(1+\frac{B}{2A}\right)\kappa p'\nabla\cdot\mathbf{v}' + \kappa\frac{\partial L}{\partial t} \tag{2.29}$$

where we used the first order relation

$$\frac{\partial p'}{\partial t} = -\rho_0 c_0^2 \nabla\cdot\mathbf{v}' \tag{2.30}$$

and the derivative chain rule

$$\frac{\partial f^2}{\partial t} = 2f\frac{\partial f}{\partial t} \tag{2.31}$$

with

$$\kappa = \frac{1}{\rho_0 c_0^2} \tag{2.32}$$

being the compressibility of the fluid.

We apply the same procedure (Eq. 2.30, 2.31) to the momentum equation, Eq. 2.22, to obtain:

$$\begin{aligned}\rho_0 \frac{\partial \mathbf{v}'}{\partial t} + \nabla P &= -\frac{1}{2}\rho_0 \nabla \mathbf{v}'^2 + \frac{\nabla P^2}{2\rho_0 c_0^2} + \rho_0 \mathbf{v}' \times \nabla \times \mathbf{v}' \\ &= -\nabla L + \rho_0 \mathbf{v}' \times \nabla \times \mathbf{v}'\end{aligned} \tag{2.33}$$

with L indicating again the Lagrangian density as defined in Eq. 2.27.

Equation 2.29 and Eq. 2.33 constitute the system of equations governing the propagation of nonlinear acoustic waves in a lossless fluid. This representation is accurate to second order and includes both the vortex mode and the potential (acoustic) mode. The vortex mode is important in a thin layer close to the boundary (called the acoustic boundary layer) and decays exponentially away from it to eventually become insignificant in comparison with the acoustic mode contributions.[3] It is important to note, however, that the vortex mode is essential to the analysis of acoustic streaming (Tjøtta and Tjøtta, 1990), a dynamic property of the fluid due to the transfer of momentum from the acoustic wave to the fluid itself, which is not considered here. We can therefore neglect the vortex mode and set $\nabla \times \mathbf{v}' = 0$ in Eq. 2.33.

In the acoustic mode (second order approximation), the Lagrangian density L vanishes for progressive plane waves for which the relationship $p' = \rho_0 c_0 \mathrm{v}$ applies. Furthermore, Aanonsen et. al., (1984) and subsequently Tjøtta and Tjøtta (1987) showed that the Lagrangian density term can only produce local nonlinear effects that depend

solely on the local properties of the sound field at the point of interest and cannot lead to cumulative nonlinear effects that produce waveform steepening and distortion.
As a general rule, except within one wavelength away from the source, local effects can be ignored for problems involving directional sound beams. Therefore, we can also neglect the Lagrangian density and set $L = 0$ in both Eq. 2.29 and Eq. 2.33.

The governing first order sytem of equations for the nonlinear acoustic wave propagation in inhomogeneous lossless fluids then becomes:

$$\kappa \frac{\partial p'}{\partial t} = -\nabla \cdot \mathbf{v}' - \mathbf{v}' \cdot \frac{\nabla \rho_0}{\rho_0} - 2\left(1 + \frac{B}{2A}\right)\kappa p' \nabla \cdot \mathbf{v}' \tag{2.34}$$

$$\rho_0 \frac{\partial \mathbf{v}'}{\partial t} + \nabla P = 0 \tag{2.35}$$

2.4 Equations in a fluid with relaxation losses

In the previous section, the fluid irradiated by an acoustic wave has been assumed in thermodynamic equilibrium. There are situations, however, such as excitation of internal modes of motion in the molecules constituting the medium, whose processes are much slower than the acoustic time scale and cannot keep the pace with the rapid changes of state induced by the acoustic wave. During this time the fluid is in a nonequilibrium state. Irreversible processes can act at this time to return the system back to its

---

[3] A detailed discussion of the acoustic boundary layer theory can be found in Pierce (1989) and Tjøtta and Tjøtta (1990).

equilibrium, or "relaxed" state, and energy is dissipated. This results in the absorption of sound.

To account for attenuation and dispersion[4] in a fluid through relaxation processes, the equations governing the propagation of sound can be obtained by Eq. 2.35 and by a modified form of Eq. 2.34. This modification arises by introducing the time convolution operator "*"in the following manner (Szabo, 1994):

$$\kappa * \frac{\partial p'}{\partial t} = -\nabla \cdot \mathbf{v}' - \mathbf{v}' \cdot \frac{\nabla \rho_0}{\rho_0} - 2\left(1 + \frac{B}{2A}\right)(\kappa * p')\nabla \cdot \mathbf{v}' \tag{2.36}$$

For the general case of N independent relaxation processes, the fluid's compressibility κ can be expressed as (Nachman et al., 1990):

$$\kappa = \kappa_\infty \delta(t) + \sum_{i=1}^{N} \frac{\kappa_i}{\tau_i} e^{-\frac{t}{\tau_i}} u(t) \tag{2.37}$$

where κ_∞ is the compressibility in the limit as the acoustic frequency goes to infinity, τ_i and κ_i are the relaxation time and relaxation modulus for the ith process, and $\delta(t)$ and $u(t)$ are, respectively, the Dirac delta function and the Heaviside unit step function. Substitution of Eq. 2.37 into Eq. 2.36 with the aid of the convolution properties

$$\frac{\partial}{\partial t}[A(t) * B(t)] = \frac{\partial A(t)}{\partial t} * B(t) = \frac{\partial B(t)}{\partial t} * A(t) \tag{2.38}$$

and

$$\delta(t) * A(t) = A(t) \tag{2.39}$$

results in the following explicit form

$$-\kappa_\infty \frac{\partial p'}{\partial t} - \frac{\partial}{\partial t}\left(p' * \sum_{i=1}^{N} \frac{\kappa_i}{\tau_i} e^{-\frac{t}{\tau_i}} u(t) \right) = \nabla \cdot \mathbf{v} \left[1 + \left(2 + \frac{B}{A} \right) \left(\kappa_\infty p' + p' * \sum_{i=1}^{N} \frac{\kappa_i}{\tau_i} e^{-\frac{t}{\tau_i}} u(t) \right) \right] + \mathbf{v}' \cdot \frac{\nabla \rho_0}{\rho_0} \quad (2.40)$$

For a medium described by this type of relaxation mechanism, the phase velocity and attenuation satisfy the Kramers-Kronig relation and their response are therefore casual (O'Donnel et al. 1981; Nachman et al., 1990; Szabo, 1995).

The presence of the time domain convolution operator in Eq. 2.40 makes solving this equation on a computer an inefficient process. To solve this problem, Carcione et al. (1988) and subsequently Yuan et al. (1999) proposed the introduction of state variables which convert Eq. 2.40 into a system of simultaneous differential equations that do not involve explicit convolution integrals. Following their derivation, state variables S_i are introduced and defined by:

$$S_i = p' * \frac{\kappa_i}{\tau_i} e^{-\frac{t}{\tau_i}} u(t) , \qquad i = 1,\ldots,N \quad (2.41)$$

Taking the derivative of Eq. 2.41 with respect to time, and making use again of 2.38 and 2.39, results in:

$$\frac{\partial}{\partial t} S_i = -\frac{1}{\tau_i} S_i + \frac{\kappa_i}{\tau_i} p' , \qquad i = 1,\ldots,N. \quad (2.42)$$

Substitution of Eqs. 2.41 and 2.42 into Eq. 2.40 yields:

---

[4] The phase speed of the acoustic wave is no longer constant resulting in either widening or shortening of the wavelength. The acoustic wave looks like it is "breathing".

$$-\kappa_\infty \frac{\partial p'}{\partial t} - \sum_{i=1}^{N}\left(-\frac{1}{\tau_i}S_i + \frac{\kappa_i}{\tau_i}p'\right) = \nabla\cdot\mathbf{v}\left[1+\left(2+\frac{B}{A}\right)\left(\kappa_\infty p' + \sum_{i=1}^{N} S_i\right)\right] + \mathbf{v}'\cdot\frac{\nabla\rho_0}{\rho_0} \qquad (2.43)$$

Equation 2.43 together with Eqs. 2.42 and 2.35 are the governing laws for the nonlinear acoustic propagation in a fluid characterized by N independent relaxation processes, with Eq. 2.42 determining the dynamics of the state variables. The complete first order system is reported below for clarity:

$$\begin{aligned}
&-\kappa_\infty \frac{\partial p'}{\partial t} - \sum_{i=1}^{N}\left(-\frac{1}{\tau_i}S_i + \frac{\kappa_i}{\tau_i}p'\right) = \nabla\cdot\mathbf{v}\left[1+\left(2+\frac{B}{A}\right)\left(\kappa_\infty p' + \sum_{i=1}^{N} S_i\right)\right] + \mathbf{v}'\cdot\frac{\nabla\rho_0}{\rho_0}\\
&\frac{\partial}{\partial t}S_i = -\frac{1}{\tau_i}S_i + \frac{\kappa_i}{\tau_i}p' \qquad (2.44)\\
&\rho_0\frac{\partial \mathbf{v}'}{\partial t} + \nabla P = 0
\end{aligned}$$

2.5 Phase speed and attenuation due to relaxation processes

In absorptive media, both the attenuation and speed of sound are frequency dependent in order for the wave field to maintain casuality. Particularly, in biological tissue —the main interest in this document— acoustic attenuation and absorption loss is primarily dominated by relaxation mechanisms (Carstensen and Schwan, 1959) which give rise, for the loss of acoustic energy, to different frequency power laws (*cfr.* Chap. 1). In the case of nonlinear propagation, the frequency dependent characteristics of the speed of sound and especially attenuation become very important. The developing higher harmonics induce dispersion in the propagating wave and are absorbed more quickly and effectively by the fluid than the fundamental.

An expression for the frequency dependent attenuation and phase speed due to relaxation processes has been derived by Nachman et al. (1990) by relating the generalized frequency domain compressibility $\kappa(\omega)$ to the phase velocity $c(\omega)$ and the attenuation coefficient $\alpha(\omega)$ and reported hereafter:

$$c(\omega)=\sqrt{\frac{2}{\rho_0}}\frac{1}{\sqrt{\kappa_\infty+\sum_i\frac{\kappa_i}{1+\tau_i^2\omega^2}+\sqrt{\left(\kappa_\infty+\sum_i\frac{\kappa_i}{1+\tau_i^2\omega^2}\right)^2+\left(\sum_i\frac{\kappa_i\tau_i\omega}{1+\tau_i^2\omega^2}\right)^2}}} \tag{2.45}$$

$$\alpha(\omega)=\omega\sqrt{\frac{2}{\rho_0}}\sqrt{-\kappa_\infty-\sum_i\frac{\kappa_i}{1+\tau_i^2\omega^2}+\sqrt{\left(\kappa_\infty+\sum_i\frac{\kappa_i}{1+\tau_i^2\omega^2}\right)^2+\left(\sum_i\frac{\kappa_i\tau_i\omega}{1+\tau_i^2\omega^2}\right)^2}} \tag{2.46}$$

Values for the relaxation times τ_i and moduli κ_i are not readily accessible or easily found in the literature as compared with attenuation coefficients and their respective governing frequency dependent laws. To overcome this difficulty, a nonlinear least square fitting (NLSQ) procedure can be applied to Eq. 2.46 to choose model parameters for an optimal approximation over a specified frequency range (Wojcik et al., 1998). To institute the NLSQ fitting procedure, denote Eq. 2.46 by $Y(\mathbf{x})$ and denote with $y(\mathbf{x})$ the attenuation frequency power laws $\alpha(\omega)=\alpha_0\left(\frac{\omega}{\omega_0}\right)^b$ which we are interested to fit. Here α_0 is the attenuation value at $\omega_0=2\pi f_0$ and f_0=1 MHz. The task is to minimize the function

$$f(\mathbf{x})=\sum\frac{(y(\mathbf{x})-Y(\mathbf{x}))^2}{\sigma^2} \tag{2.47}$$

where σ^2 is the standard error and **x** is an N-dimensional vector.

To maintain physical significance for the parameters found from the NLSQ fit as well as to keep the phase speed values bounded, constraints to the feasible domain of existence of **x** are added to the fitting procedure. These constraints

$$\begin{aligned} c(\omega_c) &= c_c \\ \alpha(\omega_c) &= \alpha_c \\ \mathbf{x} &\geq 0 \end{aligned} \tag{2.48}$$

match the speed of sound and attenuation at the central frequency of the transducer and make sure that all the parameters are positive.

CHAPTER 3

Numerical Methods for Acoustic Wave Propagation

Time domain numerical solutions of the acoustic wave equation 2.44 involve step by step integration in time and evaluation of spatial derivatives at each time step. The solutions must include efficient radiation boundary conditions to limit the computational space without introducing fictitious and unphysical reflections from the computational boundary.

Over the years, several methods have been developed for the solution of wave propagation problems. The simplest and most commonly used approach is the finite-difference time-domain (FDTD) method in which both the spatial and temporal derivatives are approximated by the central difference operator based upon truncated Taylor-series representations (Yee, 1966; Kunz and Luebbers ,1993; Tavlove, 1995). In spite of its simplicity, FDTD methods require relative large numbers of points per minimum wavelength (usually 10 to 20 for linear propagation) in order to achieve a reasonably good accuracy. This requirement is dictated by the large linear phase error (dispersion) that would otherwise accumulate rapidly with time (Kreiss and Oliger, 1972; Zing, 2000). In the case of nonlinear acoustic and long range propagation the requirement is even more stringent (50-100 points per minimum wavelength are common) which becomes computationally overwhelming especially for 3D problems.

Another class of methods, spectral methods, have been developed and applied to solve partial differential equations over the past decades (Fornberg, 1975; Gottilieb and

Orzag, 1977; Canuto et al., 1988). These methods use trigonometric functions and/or Chebyshev polynomials to represent spatial derivatives and achieve superior accuracy at fewer number of points per wavelength when compared with standard FDTD methods. The numerical codes developed in this study are based on spectral methods for the approximation of spatial derivatives and interpolating polynomials for integration in time. Both methods are discussed in the following sections.

3.1 Spatial Domain: The Periodic Pseudospectral Method

The periodic pseudospectral (PS) method is based on the use of discrete Fourier transforms to evaluate the spatial derivatives of a function. The derivatives are represented by a trigonometric polynomial and defined over a uniform grid. Indicating with $f(x)$ a one-dimensional function in space and $\Delta x = L/N_x$ as the cell size with $x_j = 0, 1, \ldots, N_x-1$, the derivative of $f(x)$ can be written as:

$$\left[\frac{\partial f(x)}{\partial x}\right]_{x=x_j} = \frac{1}{L}\sum_{m=-\frac{N_x}{2}}^{\frac{N_x}{2}-1} ik_m \tilde{f}(m) e^{ik_m x_j} \tag{3.1}$$

where $k_m = 2\pi m/L$, and $\tilde{f}(m)$ is the Fourier series:

$$\tilde{f}(m) = \Delta x \sum_{j=0}^{N_x-1} f(x_j) e^{-ik_m x_j} \tag{3.2}$$

Each of the Fourier transforms in Eq. 3.1 and 3.2 can be obtained very efficiently on a computer by using the Fast Fourier Transform (FFT) algorithm of Cooley and Tukey

(1965) with just $O(N_x log_2 N_x)$ number of operation. From the Nyquist sampling theorem it follows that the derivative in Eq. 3.1 is exact as long as $\omega \leq \pi c_i/\Delta x$ or, equivalently, $\Delta x \leq \lambda/2$ with λ being the acoustic wavelength. Therefore, even with just two points per wavelength, the PS method has no phase error due to the spatial discretization in contrast with typical finite difference methods. Moreover, unlike uniform finite difference stencils that use local approximations to the spatial derivatives, the PS method uses global functions and yields a very high order of approximation. Fornberg (1996) has in fact shown that the accuracy of derivatives computed by the PS method on an N_x points grid is equivalent to the same derivatives computed by an N_x-order finite difference stencil. The N_x-order finite difference approximation to the derivative would however be many folds more expensive computationally than the FFT subroutine.

An easily implemented, three-step procedure is used to obtain values for the first derivatives by the periodic PS method (from Fornberg, 1996 pg. 185):

1. Perform a complex FFT on the data values at each grid point.

2. Multiply the output elements from this FFT,

$$[\hat{u}_0 \quad \hat{u}_1 \quad \hat{u}_2 \quad \ldots \quad \hat{u}_{N/2-1} \quad \hat{u}_{N/2} \quad \hat{u}_{N/2+1} \quad \ldots \quad \hat{u}_{N/2-2} \quad \hat{u}_{N-1}],$$

by

$$2/(b-a)*[0 \quad \pi i \quad 2\pi i \quad \ldots \quad (N/2-1)\pi i \quad 0 \quad -(N/2-1)\pi i \quad \ldots \quad -2\pi i \quad -\pi i],$$

where [a,b] is the spatial period and $i = \sqrt{-1}$

3. Perform a complex inverse FFT on the result.

Since the complex FFT is a linear function and will yield real data if the inputs are real data, the real and imaginary part of the FFT algorithm can be initialized with two independent real data sets -for example the x and y values in a 2-dimensional grid- and the derivatives of each in the real and imaginary outputs can be recovered simultaneously.

A practical disadvantage of the above method is its spatial periodicity: waves exit on one side and are "wrapped around", entering the computational field from the other side. Thus, an adequate implementation of numerical boundaries is required.

From the above discussion it is obvious that for partial differential equations (PDE) with constant coefficients the PS method represent a very efficient and accurate routine for spatial differentiation. However, when the PS method is used for PDEs with variable coefficients, numerical errors are introduced at material interfaces. Although a complete theoretical analysis of the extent of the errors is not available, numerical results (Liu, 1998) show advantages of the PS method over finite difference methods provided that higher spatial frequencies (i.e. more points per wavelength) are included to address the Gibbs phenomena. Wojcik et al., (1998) in their numerical study also demonstrated that for the low contrasts typical of soft tissue PS spatial derivatives are adequate at 6-8 points per wavelength.

3.2 Time domain: The Staggered Adam-Bashforth Method

The Adam-Bashforth method is a popular multistep method based on finite difference approximations for the solution of ordinary differential equations (ODE). The principle behind a multistep method is to utilize the past values of the derivatives to construct an interpolating polynomial that approximate the derivative function into the next interval. The number of past points that are used determine the degree of the polynomial and are therefore responsible for the extent of the truncation error. If three past points are used, the approximating polynomial will be quadratic; if four points are used than the polynomial will be cubic and so on. The order of accuracy of the method is equal to the degree of the interpolating polynomial increased by one and also to the power of the step size in the global error term of the formula (the global error is one order greater than the local error), as shown by Gerald, (1980).

To illustrate these concepts we write a model differential equation as:

$$\frac{dy}{dt} = f[t, y(t)] \equiv dy = f[t, y(t)]dt \tag{3.3}$$

and integrate between t and $t+\Delta t$. The results is

$$y_{t+\Delta t} - y_t = \int_t^{t+\Delta t} f[t, y(t)]dt \tag{3.4}$$

In order to integrate the right hand side of Eq. 3.4 a third order polynomial is used to approximate $f[t,y(t)]$. The polynomial, obtained by Newton's interpolation formula, is based on backward finite differences and yields

$$y_{t+\Delta t} = y_t + \Delta t(f_t + \frac{1}{2}\nabla f_t + \frac{5}{12}\nabla^2 f_t + \frac{3}{8}\nabla^3 f_t), \quad R = O(\Delta t^5) \tag{3.5}$$

where R is the local error term and ∇^n are the backward finite difference operators defined as:

$$\begin{aligned} \nabla f(t) &= f(t) - f(t-\Delta t) \\ \nabla^2 f(t) &= \nabla f(t) - \nabla f(t-\Delta t) \\ \nabla^3 f(t) &= \nabla^2 f(t) - \nabla^2 f(t-\Delta t) \end{aligned} \tag{3.6}$$

Rewriting Eq. 3.5 in terms of the derivative estimates instead of their backward differences produces the standard 4th-order Adam-Bashforth formula:

$$y_{t+\Delta t} = y_t + \frac{\Delta t}{24}(55f_t - 59f_{t-\Delta t} + 37f_{t-2\Delta t} - 9f_{t-3\Delta t}), \quad R = O(\Delta t^5) \tag{3.7}$$

Ghrist et al., (2000) recently introduced novel families of multistep methods for the solution of ordinary differential equations (ODEs) based on the concept of staggered time levels. To utilize the new methods, the requirement is that y and $\frac{\partial y}{\partial t}$ exist on interlaced time levels. This being the case, they derived a new stagger version of the 4th-order Adam-Bashforth routine with an error constant approximately nine times smaller and a stability domain almost three times larger than the standard version. These improvements allow the routine to be more accurate and to be stable for larger time steps, reducing the overall computational time. Following Ghrist et al. (2000) the 4th-order staggered Adam-Bashforth formula is expressed as

$$y_{t+\Delta t} = y_t + \Delta t\left(\frac{13}{12}f_{t+\frac{1}{2}\Delta t} - \frac{5}{24}f_{t-\frac{1}{2}\Delta t} + \frac{1}{6}f_{t-\frac{3}{2}\Delta t} - \frac{1}{24}f_{t-\frac{5}{2}\Delta t}\right), \quad R = O(\Delta t^5) \tag{3.8}$$

where the stencil coefficients can be found by Padé expansion (Fornberg, 1998).

In the solution of Eq. 2.44 the staggering in time is performed by having the pressure p' as well as the state variables S_i existing on integer time steps and interlacing to them the particle velocity $\mathbf{v}'$ at half time steps. At first the system may appear to be formed not by ODEs but by PDEs. However, arranging time derivatives on the left hand side and the remaining terms on the right hand side it can be noticed that the right hand side terms only involve values at previous time steps which are calculated using the PS method and are therefore known. The PDEs system is hence reduced to a system of ODEs which allows the use of the staggered Adam-Bashforth routine.

3.3 Perfectly matched layers (PML) absorbing boundary conditions

To simulate wave propagation and scattering in an unbounded medium, proper computational boundary conditions are required to avoid numerical reflections of the propagating wave at the edges of the computational domain as well as to absorb the outgoing waves. The need became even more apparent when in Sec. 3.1 we discussed the PS method with the intrinsic periodicity of Fourier transforms leading to "wrap around" effects. The problem is solved by the introduction of perfectly matched layers (PML) absorbing boundary conditions (BC). This particular BC formulation, recently developed by Berenger (1994) for a two-dimensional electromagnetic problem involving TE and

TM polarized waves, will attenuate the incident wave and at the same time will not introduce artificial reflections at these same boundaries.

The basic idea of the PML BC is to create a set of boundary layers at the edges of the computational domain and define a nonphysical new set of equations in the PML region. These equations are characterized by large attenuation values but no impedance mismatch with respect to the rest of the field and will not produce reflections for any angle of incidence.

To introduce the PML we apply the concept of complex coordinate stretching (Chew and Weedon, 1994; Chew et al., 1997; Liu and Tao, 1997, He and Liu, 1999) by the change of variables

$$\tilde{\zeta} = \int_0^{\zeta} s_{\zeta}(\zeta')\partial\zeta' \qquad \xi = \text{x, y, z} \tag{3.9}$$

$s_{\xi}(\xi)$ being the complex coordinate stretching variables, and the unphysical splitting of the scalar pressure and the state variables into three additive components

$$p' = \sum_{\zeta=x,y,z} p'^{(\zeta)} \quad \text{and} \quad S_i = \sum_{\zeta=x,y,z} S_i^{(\zeta)} \tag{3.10}$$

which will be related to the corresponding particle velocity components.

In the frequency domain, we define $s_{\zeta} = a_{\zeta} + i\frac{\omega_{\zeta}}{\omega}$ such that $\frac{\partial}{\partial\zeta} = \frac{1}{s_{\zeta}}\frac{\partial}{\partial\zeta}$ ($\xi = \text{x, y, z}$)

where a time dependence of $e^{-i\omega t}$ is implied. By introducing of the complex coordinates and splitting of the pressure and state variables (Eq. 3.10), the system of equations (Eq. 2.44) in the frequency domain becomes:

$$-\kappa_\infty(-i\omega p'^{(\zeta)})-\sum_{i=1}^{N}\left(-\frac{1}{\tau_i}S_i^{(\zeta)}+\frac{\kappa_i}{\tau_i}p'^{(\zeta)}\right)=\left(\begin{array}{l}\dfrac{1}{\left(a_\zeta+\dfrac{i\omega_\zeta}{\omega}\right)}\dfrac{\partial v'_\zeta}{\partial\zeta}\left[1+\left(2+\dfrac{B}{A}\right)\left(\kappa_\infty p'^{(\zeta)}+\sum_{i=1}^{N}S_i^{(\zeta)}\right)\right]+\\ +\dfrac{1}{\left(a_\zeta+\dfrac{i\omega_\zeta}{\omega}\right)}\dfrac{v'_\zeta}{\rho_0}\dfrac{\partial\rho_0}{\partial\zeta}\end{array}\right)$$

$$-i\omega S_i^{(\zeta)}=-\frac{1}{\tau_i}S_i^{(\zeta)}+\frac{\kappa_i}{\tau_i}p'^{(\zeta)} \qquad (3.11)$$

$$-i\omega\rho_0 v'_\zeta+\frac{1}{\left(a_\zeta+\dfrac{i\omega_\zeta}{\omega}\right)}\frac{\partial p'}{\partial\zeta}=0$$

In the system (3.11)—where $p'=p'(\zeta,\omega)$, $\mathbf{v}'=\mathbf{v}'(\zeta,\omega)$, and $S_i=S_i(\zeta,\omega)$— the real part $a_\zeta\geq 1$ is a scaling factor while the imaginary part $\omega_\zeta>0$ represents the loss in the PML region. The PML BC are constructed by defining an m samples thick layer around the computational domain in which the values of ω_ζ increase smoothly and monotonically from the inner to the outer layer from zero to a maximum value. To achieve an effective absorption of the incident wave a quadratic function is used over an ten-node PML boundary layer with the maximum attenuation set such to achieve a one-tenth amplitude reduction over a propagation distance of one spatial step. Yuan et al. (1997) demonstrated that such an implementation would reduce spurious reflections by approximately 80 to 90 dB. The inner, non-PML region, is characterized by $a_\zeta=1$ and $\omega_\zeta=0$ yielding regular cartesian coordinates computations.

Inverse Fourier transforming (Eq. 3.11) we obtain the time-domain system of equations that govern nonlinear acoustic propagation in inhomogeneous media with losses included

through relaxation mechanisms. Only including two relaxation mechanisms, which produces a good trade off between goodness of fit to the analytical frequency power law for attenuation and memory/execution speed on a computer, the system (Eq. 3.11) can be recast, after some algebra, as follows:

$$
\begin{aligned}
-\kappa_\infty a_\zeta \frac{\partial p'^{(\zeta)}}{\partial t} &= \omega_\zeta \kappa_\infty p'^{(\zeta)} - a_\zeta \left(\sum_{i=1}^{2} \frac{S_i^{(\zeta)}}{\tau_i} - \sum_{i=1}^{2} p'^{(\zeta)} \frac{\kappa_i}{\tau_i} \right) + \\
&\quad + \omega_\zeta \left(\sum_{i=1}^{2} \int_{-\infty}^{t} \frac{\kappa_i}{\tau_i} p'^{(\zeta)}(\zeta, t') dt' - \sum_{i=1}^{2} \int_{-\infty}^{t} \frac{S_i^{(\zeta)}(\zeta, t')}{\tau_i} \partial t' \right) + \\
&\quad + \left(1 + \beta \kappa_\infty p'^{(\zeta)} + \beta \sum_{i=1}^{2} S_i^{(\zeta)} \right) \frac{\partial v'_\zeta}{\partial \zeta} + \frac{v'_\zeta}{\rho_0} \frac{\partial \rho_0}{\partial \zeta} \qquad (3.12) \\
\frac{\partial}{\partial t} S_i^{(\zeta)} &= -\frac{1}{\tau_i} S_i^{(\zeta)} + \frac{\kappa_i}{\tau_i} p'^{(\zeta)} \\
a_\zeta \frac{\partial v'_\zeta}{\partial t} &= -\frac{1}{\rho_0} \frac{\partial p'}{\partial \zeta} - \omega_\zeta v'_\zeta
\end{aligned}
$$

where $\beta = 2 + \frac{B}{A}$. The integrals in (Eq. 3.12) account for the coupling of the loss in the PML region with the attenuation loss due to the relaxation mechanisms in the regular domain (Liu and Tao, 1997).

3.4 Nonlinear Least Square Fit (NLSQ) and the Nelder-Mead Simplex Method

Values for relaxation times and compressibility moduli are not easily found or commonly reported in the literature as compared with attenuation values and respective frequency power laws. As described in section 2.5, to overcome the problem a NLSQ fit

(*c.f.* Eq. 2.47) is performed, subject to predetermined constraints (Eq. 2.48), of the function describing the generalized frequency dependent attenuation, (Eq. 2.46 referred to as $Y(\mathbf{x})$) with the analytical expression $y(\mathbf{x})$ describing the frequency power law characteristic of a particular fluid or tissue. Before performing the optimization, the constrained minimization problem is transformed to an unconstrained one by the use of penalty functions. Unconstrained minimizations present a faster convergence rate and avoid the use of Lagrangian multipliers limiting the number of operation needed (Luenberger, 1973). Introducing the penalty functions, the constrained problem

$$\text{minimize} \quad f(\mathbf{x}) \qquad \text{subject to } \mathbf{x} \in S \tag{3.13}$$

is replaced by the unconstrained problem

$$\text{minimize} \quad f(\mathbf{x})+\mu P(\mathbf{x}) \tag{3.14}$$

where μ is a positive constant. The continuous penalty function, P, is greater than zero for all $\mathbf{x}$ in the feasible domain, and it is exactly zero if and only if $\mathbf{x} \in S$. Given the constraints in the form:

$$\mathbf{x} : g_i(\mathbf{x}) \le 0,\ i = 1,2,\ldots,p \tag{3.15}$$

a very useful penalty function is:

$$P(\mathbf{x}) = \sum_{i=1}^{p} (\max[0, g_i(\mathbf{x})])^2 \ . \tag{3.16}$$

The minimization of Eq. 3.14 is performed by the Nelder-Mead Simplex method, sometimes referred to as the "amoeba algorithm" (Nelder and Mead, 1965). Here we only present the general concepts of the algorithm. For a more detail treatment and an

outline of the numerical implementation the reader is referred to the work of Lagarias et al. (1998) and to the well know handbook *Numerical Recipes* (Flannery et al., 1988). The Nelder-Mead algorithm, in the class of direct search methods, attempts to minimize a scalar-valued nonlinear function of n real variables by only using function values, without any derivative information. At each step it creates a geometric figure in n dimensions of nonzero volume bounded by $n+1$ vertices called a *simplex*. Each iteration in the search method begins with a simplex created by the guessed values and specified by its $n+1$ vertices and the associated function values. One or more test points are computed, along with their function values, and the iteration terminates with the generation of a new (different) simplex such that the function values at its vertices satisfy some form of descent condition compared to the previous simplex. The Nelder-Mead algorithm is very fast and parsimonious in function evaluations and typically only requires two function evaluations to construct a new simplex

CHAPTER 4

Transducer Arrays and Sources

In this chapter we introduce the idea of acoustic sources which are used to initialize the propagation of the sound wave. We start with a brief description of the concept of a point source in Sec. 4.1, followed by a more relevant discussion on commonly used physical transducers and the concepts of focusing and steering. Section 4.2 is devoted to line arrays and 1-D arrays while Sec.4.3 focuses mainly on 2-D arrays.

These acoustic sources are included in the numerical methods as internal initial conditions of either pressure or velocity values over specified grid points.

4.1 Point Sources

An acoustic source whose dimensions are much smaller than a wavelength of the signal at which it is driven is commonly considered being of zero dimensions, to maintain spherical symmetry, and it is known as a point source. The acoustic field generated by such a source in an unbounded, lossless medium spreads equally in all directions with its amplitude decaying proportionally to the distance traveled. If the source is impulsive the resulting sound field is described by the *free-space Green's function*,

$$G(x \mid x_s) = \frac{e^{ikR}}{R} \tag{4.1}$$

with $R=|x-x_s|$ being the distance from the source at position x_s. The Green's function is in fact the spatial impulse response solution of the linearized wave equation presented in Chap. 2.

Point sources are in general extremely important, as we will see in the following sections, because they provide the building blocks for the development and analysis of more general and complicated acoustic radiators commonly used in modern ultrasound applications. Furthermore, a point source approximation for transmitters and receivers is widely used in ocean acoustics where the interest is mainly on long distance propagation at relatively low frequencies. A numerical example of the acoustic field generated by such a source in a layered model of the ocean is shown in Figure 1.

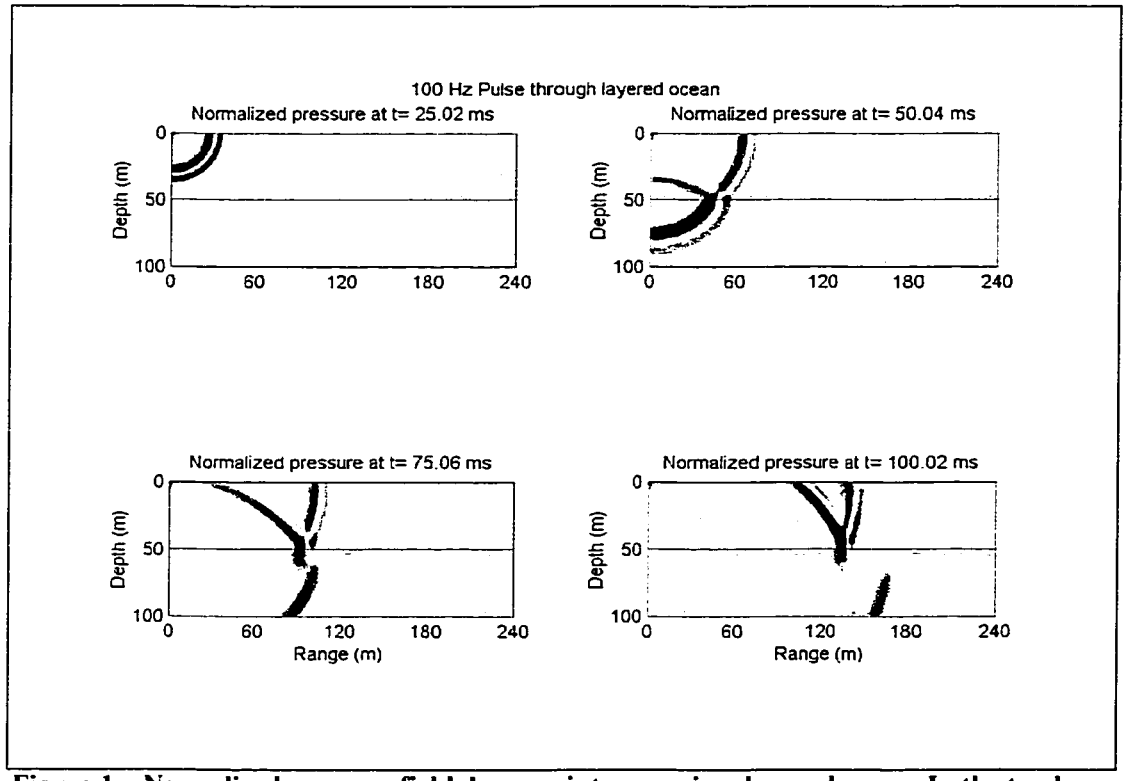

Figure 1 – Normalized pressure field due a point source in a layered ocean. In the top layer c=1500m/s; in the bottom layer c=2500 m/s

4.2 Line Arrays and 1-D Array

The simplest distribution of a source with multiple elements is the line array. In this conformation N point sources are distributed, usually equally spaced, along a line. This type of source no longer produces a spherically diverging acoustic field due to constructive and destructive interference of the individual sources fields. In linear acoustics, the total acoustic pattern produced by the line array can be predicted by using the principle of superposition together with Eq. 4.1. Fig. 2 shows a schematic of such a field when all the point sources are equally excited.

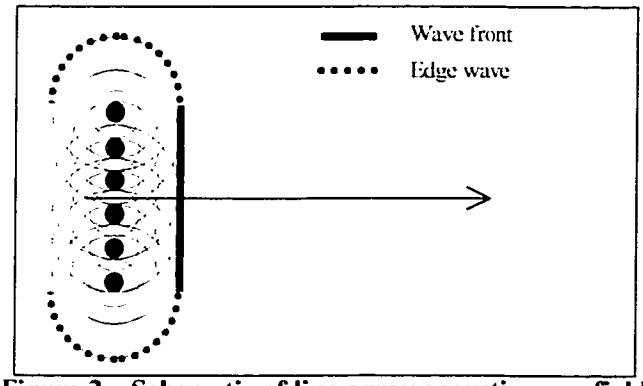

Figure 2 – Schematic of line array acoustic wave field

When enough point sources are included such that the spacing between them is virtually decreased to zero, the line array collapses into a single linear element source of length L with the same field characteristics as in Fig. 2.

An extremely important advantage of arrays with multiple elements, normally used in ultrasound machines, is that the individual elements can be driven separately with different strengths and time delays. This strategy leads to the concepts of beam steering

and focusing for the theory and applications of which a wide body of literature exists (Von Ramm and Smith, 1983; Turnbull and Foster, 1991).

Beam steering refers to the property of "aiming" the main wave front to propagate along a direction other than normal to the face of the array. It is accomplished by linearly delaying the firing time of each element from one side of the array to the other. The necessary time delays to steer the acoustic beam at an angle θ are found by the linear relationship

$$t_{delay}^{n} = n\frac{d}{c}\sin(\theta) + T \tag{4.2}$$

where n indicates the element in the array, d the separation distance between elements, c is the speed of sound, and T refers to some time delay.

Focusing can be interpreted as a direct consequence of beam steering. In this case, however, a quadratic variation in the time delays is applied to the array elements such that along the axis, on the region of total convergence, maximum constructive interference is achieved. The localized region, known as the focal area, presents an amplified acoustic intensity in space, time, or both. The focusing feature is greatly exploited in ultrasound applications both for imaging purposes and, most of all, for therapeutic goals in the field of high intensity ultrasound.

Beam steering and focusing can also be combined to obtain a focusing wave front propagating off-axis. In this case, Von Ramm and Smith (1983) proposed the following functional form for the necessary time delays

$$t_{delay}^{n} = \frac{F}{c}\left(1-\left[1+\left(\frac{nd}{F}\right)^{2}-2\frac{nd}{F}\sin(\theta)\right]^{1/2}\right)+T \qquad (4.3)$$

with the new variable, F, being the focal distance.

It should be noted that both beam steering and focusing can also be accomplished by different spatial distributions of the point sources when they are all driven in phase (i.e. at the same time). For example, if all the sources were to be positioned along an arc length of a circle and fired at the same instant, the wave front would converge to the geometrical focus (i.e. the center of the circle).

Ultrasound transducers are manufactured by mounting several single elements of length L and width δ on a housing case. Each element in the array is driven by an independent channel that controls both the power applied and the firing time. In 1-D imaging arrays it is usually the case that $L >> \delta$. Some sketched examples of 1-D arrays used in commercial ultrasound machines are shown in Figure 3.

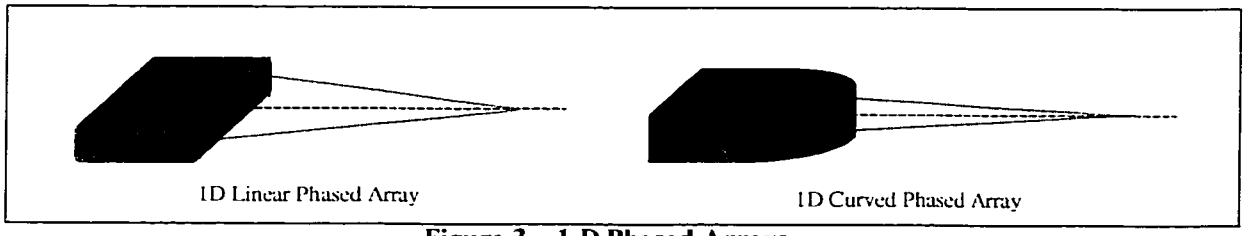

Figure 3 – 1-D Phased Arrays

This type of transducer has two degrees of freedom; it can dynamically move the focusing position off-axis in the plane of the transducer and, at the same time, change the focusing depth.

One-dimensional arrays are very similar to line arrays except for the finite length of the elements in the elevation direction. This will introduce an additional diffraction pattern to the acoustic field whose strength is proportional to the length L of the elements. The characteristics of the added diffraction, the so called mechanical focus of the transducer, are fixed at the time of manufacture of the array and, depending on the region of interest, may or may not affect the beam pattern generated electronically. In particular, if the region interrogated by the sound is far away from the region of the mechanical focus, then the acoustic field is primarily due to the electronic focus characteristics and the array can be modeled in 2-D as a line array. On the other hand, if the transducer was designed with a strong mechanical focus and the interest is in the overlapping region, a full 3-D simulation is required to correctly capture the spatial and temporal beam patterns. Figure 4 shows a numerical example of a line array/1-D array focusing off-axis.

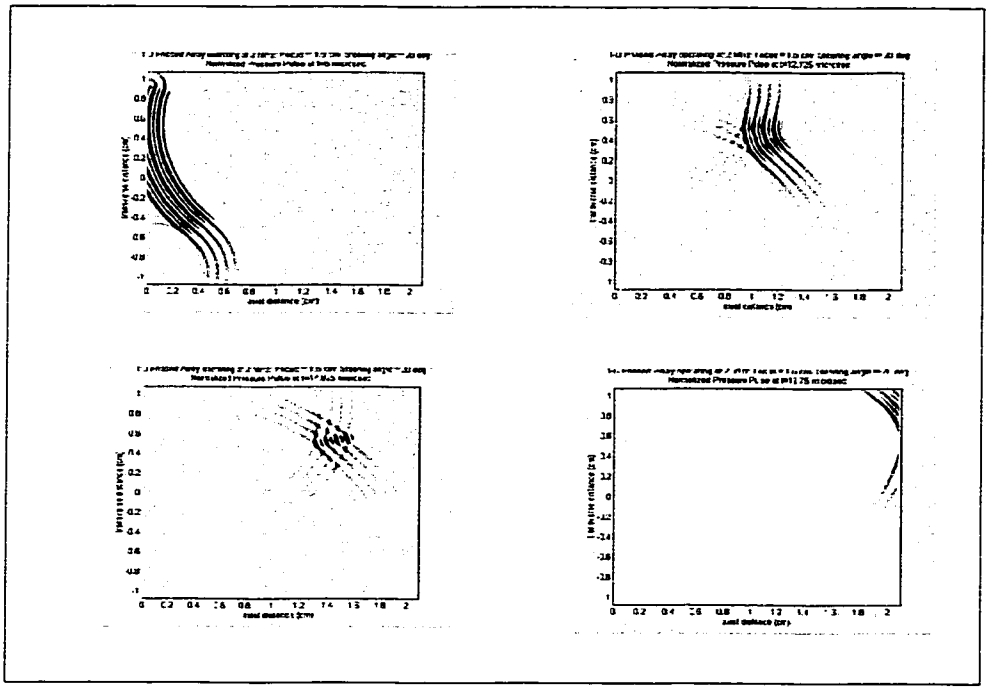

Figure 4 – Propagating pulse from line array/1-D phased array steered at 20 degrees angle

4.3 2-D Arrays

A two-dimensional array transducer is composed of N by M elements, each element usually of equal length and width, arranged in a matrix form on a particular substrate. This type of transducer is the most versatile of all and has a total of three degrees of freedom. Its capabilities include dynamical movement of the focusing position off-axis in the transverse plane, the elevation plane, and the depth plane at the same time. In other words, given a finite volume, the 2-D array is capable of targeting (almost) any point in the volume. The increased versatility is achieved at the expense of extended and more complicated electronics needed to drive the array. Figure 5 shows some examples of 2-D phased arrays and Figure 6 depicts a numerical result of a 16 by

16 elements planar array phased to produce eight simultaneous foci equally spaced around a circle.

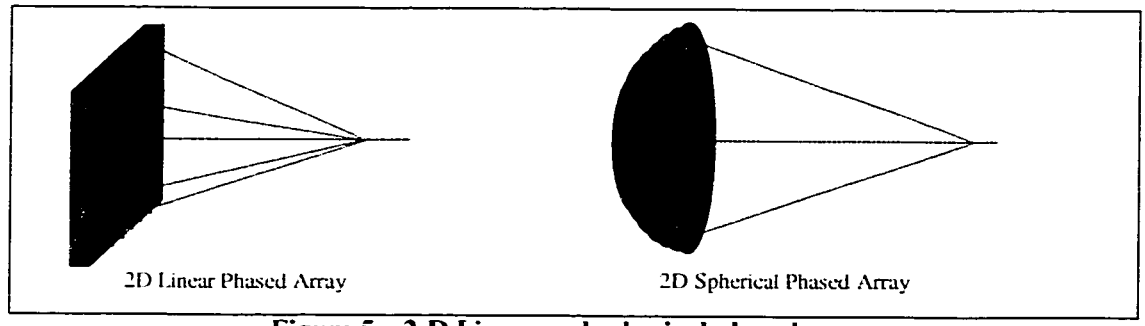

Figure 5 – 2-D Linear and spherical phased arrays

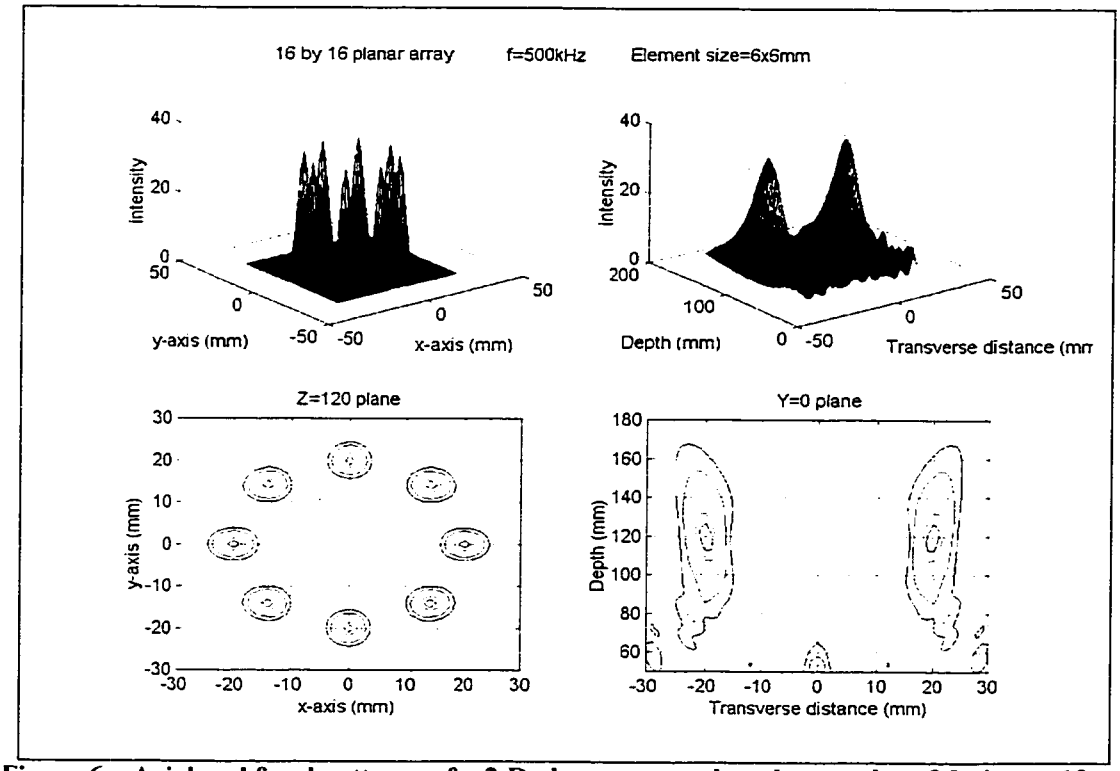

Figure 6 – Axial and focal patterns of a 2-D planar array phased to produce 8 foci at z=12 cm

CHAPTER 5

Absorbed Energy and Temperature Rise

In this chapter, we focus on the transfer of acoustic energy that occurs when a sound wave propagates in an absorbing medium and in particular on the mechanisms and effects of acoustic heating. We start by presenting an analysis of the terms involved in the transformation from acoustic energy to thermal energy in Sec. 5.1. Successively, in Sec. 5.2, the discussion is centered on the governing law for heat transfer and, specifically, as it applies to biological tissue. We conclude the chapter with a discussion in Sec. 5.3 concerning the numerical methods used to solve the time-dependent bio-heat equation.

5.1 Acoustic Intensity and Heat Rate

The energy involved in the propagation of acoustic waves through a fluid medium is of two forms, the kinetic energy of the moving particles and the potential energy of the compressed fluid. As the fluid expands and compresses during the transmission of the sound wave, energy is transferred from a fluid volume to an adjacent one. In the second order of approximation (Makarov, 1996), this acoustic energy flux describes the work of the pressure p on the fluid and is expressed as

$$\mathbf{J}_a = p\mathbf{v} \tag{5.1}$$

with the subscript a indicating the acoustic mode, and the primes on the acoustic variables (cfr. Chap. 2) are suppressed.

The acoustic intensity **I** of a sound wave is then defined as the average rate of flow of energy through a unit area normal to the direction of propagation (Kinsler and Frey, 1982),

$$\bar{\mathbf{J}}_a = \mathbf{I} = \frac{1}{t_{av}} \int_{-t_{av}/2}^{t_{av}/2} p\mathbf{v}\partial t \tag{5.2}$$

where the overbar indicates the time average and the averaging time t_{av} can be chosen to fit the specified problem. For periodic waves, t_{av} equals the period. For nonperiodic waves, on the other hand, it can be chosen to be a long enough time interval such that the calculated intensity converges to a value independent of t_{av}. For progressive, time harmonic, and linearly propagating waves in attenuating media, intensity can be expressed as a function decaying exponentially with distance

$$I = I_x = I_0 e^{-2\alpha_0 x} \tag{5.3}$$

where I_0 indicates the initial intensity of the wave and α_0 the small-signal attenuation coefficient per unit distance. This no longer holds true for the propagation of nonlinear waves due to the formation of shocks, and the intensity needs to be computed directly from Eq. 5.2.

Acoustic waves propagating in an attenuating medium lose both their energy and their momentum. As a consequence, two other modal fields appear with the acoustic mode, acoustic streaming and acoustic heating. Following the reasoning we used in the

derivation of the nonlinear wave equation (*c.f.* Sec. 2.3), we do not treat acoustic streaming because it is a direct consequence of the vortex mode which we discarded assuming that the fluid is irrotational.

The total energy conservation law in an absorbing fluid is given by

$$\frac{\partial E_a}{\partial t} + \frac{\partial E_h}{\partial t} + \nabla \cdot \mathbf{J}_a + \nabla \cdot \mathbf{J}_h = 0 \tag{5.4}$$

Here, we expanded the total energy in two parts correlating the two different modal fields: the acoustic mode with subscript a and the heating mode with subscript h. The energy conservation law, as expressed by Eq. 5.4 describes the instantaneous changes and balances of the total energy in the system. However, our interest is focused primarily upon the energy transfer on a much larger time scale. We achieve this goal by time-averaging Eq. 5.4. Note that the quantity $\frac{\partial \overline{E}_a}{\partial t}$ is identically equal to zero, which is a consequence of the periodicity condition of the acoustic field[5]. It follows that

$$\frac{\partial \overline{E}_h}{\partial t} + \nabla \cdot \overline{\mathbf{J}}_h = -\nabla \cdot \overline{\mathbf{J}}_a \tag{5.5}$$

Furthermore, acoustic heating is usually considered to be a quasi-steady effect in comparison with the rapidly oscillating sound field such that we may safely omit the time average on the left-hand side of Eq. 5.5 and rewrite the energy conservation law as

$$E_h + \nabla \cdot \mathbf{J}_h = Q = -\nabla \cdot \overline{\mathbf{J}}_a \tag{5.6}$$

---

[5] Note that if a quantity f is periodic in time then $\frac{\partial \bar{f}}{\partial t} = 0$

The quantity $-\nabla \cdot \bar{\mathbf{J}}_a$ is interpreted as a source per unit volume of the "non-acoustic" energy. From Eq. 5.6, this source is exactly zero for wave propagation in lossless fluids where only the acoustic mode exists. On the other hand, if wave attenuation becomes significant due to shock waves or simply lossy media, this term is no longer zero. In general, this divergence assumes a negative value which describes irreversible losses of the acoustic energy and its transformation to heat (Nyborg, 1981). Hence, a distributed thermal source appears in the domain covered by the sound field whose density per unit volume is equal to

$$Q = -\nabla \cdot \mathbf{I} \tag{5.7}$$

where we used the definition of acoustic intensity of Eq. 5.2.

This thermal source is responsible for the temperature increase in media exposed to acoustic waves and is the coupling term between sound propagation and temperature dynamics in the following section.

5.2 Temperature Rise in Tissue

The basic law that describes the relationship between the heat flow and the temperature gradient, based on experimental observation, was derived by and named after the French scientist Joseph Fourier (1822). In its general, differential form, the heat transfer law is expressed as

$$\rho C \frac{\partial T}{\partial t} = \nabla \cdot (k \nabla T) + f \tag{5.8}$$

where ρ is the density of the material, C and k its heat capacity and conductivity, T is temperature, and f a distributed source term.

In biological systems, the main concern of this document, Eq. 5.8 cannot be applied directly due to the complexity and dynamic characteristics of the system itself. However, the source function f in Eq.5.8 can be expanded as a linear summation of various heat sources and heat sinks. In tissue there are several heat sources and sinks. For example, metabolic processes add energy to the system and tend to increase the tissue's temperature. On the other hand, cooling processes such as conduction, convection, and advection tend to decrease the overall system's temperature. Conduction occurs when a temperature gradient is established inside the medium and it is expressed by Eq. 5.8. Convection takes place by the blood flow of capillary beds and it is believed to be one of the most important cooling process in the human body. This process, in the medical field, is usually referred to as perfusion. Advection, on the other hand, is manifested only in the presence of much larger vessels, where the blood carries heat away from a specific location and dissipates it along the direction of the flow.

By taking into account all of the above mentioned processes, we extend Eq. 5.8 to apply specifically in biological systems. This extended law is commonly referred to as the *bio-heat transfer equation* (BHTE) (Pennes, 1948)

$$\rho C \frac{\partial T}{\partial t} = \nabla \cdot (k \nabla T) - wC(T - T_{\infty}) - \rho C(\mathbf{u} \cdot \nabla T) + Q + Q_{m} \tag{5.9}$$

where ρ, C, and k are the density, specific heat capacity and thermal conductivity of the tissue, T_{∞} refers to the temperature at large distances from the acoustically-induced

thermal lesion which corresponds to the initial condition value of body temperature at 37°C. The first term on the right hand side of Eq. 5.9 accounts for heat diffusion, the second term is responsible for blood perfusion losses with w being the perfusion rate. The perfusion term in the BHTE assumes that blood reaches the capillaries at the temperature of the supply vessel and thermally equilibrates with the surrounding instantaneously. In contrast, the third term on the right hand side of Eq. 5.9 captures the advection of heat created by the flow of blood with velocity **u** in a larger vessel where instantaneous equilibrium of temperature is no longer valid. The source term Q and Q_m are the heat rate generated by the acoustic field (*c.f.* Eq. 5.7) and the metabolic processes. The average heating rate generated by metabolic processes by a 100 kg person on a regular diet is on the order of 1000 W/m^3 or, equivalently 10^{-3} W/cm^3 (Carstersen, 1987 pag. 88). This figure is much smaller of the heat rates, usually of the order of tens to hundreds of W/cm^3, generated by the acoustic field in high intensity applications. In this respect, the Q_m term can be omitted without loss of accuracy and generality.

5.3 Numerical solution of the BHTE

The BHTE is solved numerically in a manner analogous to the solution of the wave equation. In this case, however, the spatial derivatives are computed by standard finite difference methods as opposed to the pseudospectral method and the order of the time integration routine is reduced to third.

Equation 5.9, in comparison with the nonlinear wave equation (Eq. 2.44), is a parabolic diffusive type equation with smooth and slow varying profiles both in space

and time. Standard second-order finite difference approximation of the spatial derivatives has been shown to be very satisfactory in terms of accuracy for parabolic type of equations (Ozisik,1980) and it is faster to compute than FFT-based derivatives. To solve the governing equation, the computational field in which the solution is sought needs to be discretized to form a grid. The discretization, for a 3-D problem in Cartesian coordinates with time dependence, is performed as follows: the space dimensions x, y, and z, as well as the time variable t, are written using indexes i, j, k, n, as $x_i = i\Delta x$, $y_j = j\Delta y$, $z_k = k\Delta z$, $t_n = n\Delta t$ with $i = 0,1, \ldots, N_x$, $j = 0,1, \ldots, N_y$, $k = 0,1, \ldots, N_z$, and $n = 0,1, \ldots, N_t$, where Δx, Δy, Δz, and Δt are respectively the x, y, z, and t increments. Using a second order Taylor series expansion at a given time n, the spatial first derivatives are approximated as

$$\begin{aligned}
\frac{\partial T^n_{i,j,k}}{dx} &= \frac{T^n_{i-1,j,k} - T^n_{i-1,j,k}}{\Delta x} \\
\frac{\partial T^n_{i,j,k}}{dy} &= \frac{T^n_{i,j-1,k} - T^n_{i,j+1,k}}{\Delta y} \\
\frac{\partial T^n_{i,j,k}}{dz} &= \frac{T^n_{i,j,k-1} - T^n_{i,j,k+1}}{\Delta z}
\end{aligned} \tag{5.10}$$

and the second derivatives as

$$\begin{aligned}
\frac{\partial^2 T^n_{i,j,k}}{dx^2} &= \frac{T^n_{i-1,j,k} - 2T^n_{i,j,k} + T^n_{i+1,j,k}}{\Delta x^2} \\
\frac{\partial^2 T^n_{i,j,k}}{dy^2} &= \frac{T^n_{i,j-1,k} - 2T^n_{i,j,k} + T^n_{i,j+1,k}}{\Delta y^2} \\
\frac{\partial^2 T^n_{i,j,k}}{dz^2} &= \frac{T^n_{i,j,k-1} - 2T^n_{i,j,k} + T^n_{i,j,k+1}}{\Delta z^2}
\end{aligned} \tag{5.10}$$

The time integration is carried out with a standard third order Adam-Bashforth method as described in Sec. 3.2. The integration routine then becomes

$$y_{t+\Delta t} = y_t + \Delta t(\frac{23}{12} f_t - \frac{4}{3} f_{t-\Delta t} + \frac{5}{12} f_{t-2\Delta t}),\ R = O(\Delta t^4) \tag{5.11}$$

CHAPTER 6

The High Intensity Focused Ultrasound Experiments and Data Analysis

The High Intensity Focused Ultrasound (HIFU) system currently includes focused ultrasound sources, 3-D positioning and calibration devices, degassing systems, sample holders, data analysis apparatus, as well as electrical drive and monitoring equipment. The entire system is complemented by a commercial diagnostic ultrasound machine (ATL, HDI1000, Bothel, WA). Apart from commercially available items (i.e. function generators, power amplifiers, etc), the system was fully designed and developed in-house at the Center for Industrial and Medical Ultrasound, Applied Physics Laboratory, University of Washington by Peter Kaczkowski, Cyril Lafon, and Fran Olson and it is shown in Figures 7 and 8. This system allows us to produce and monitor ultrasound-induced lesions with high accuracy and also to determine acoustic parameter values that will be used to initialize and validate the computer model.

6.1 Treatment experimental setup and methods

The experimental setup for HIFU treatment is illustrated in Figure 7. The holding tank (6) is filled with degassed water and maintained at a constant temperature of 37 °C by a heater. A needle PVDF hydrophone (NTR, Seattle, WA) is mounted on the fixed reference base (7) and the 3-D positioning system (5) is used to position the treatment

transducer (2) (3.5 MHz, 23 mm diameter, 35 mm focal length by Sonic Concepts, Woodinville, WA) such that the hydrophone signal corresponds to the transducer's focal spot. The treatment transducer is driven at low amplitude by a function generator (HP 33120A, Loveland, CO) through a power amplifier (ENI, 400B, Rochester, NY). Between the power amplifier and the treatment transducer a power meter is used to monitor the electrical power applied. After positioning is completed, the PVDF hydrophone is removed and replaced by the sample holder (1) (5x5x7cm) filled with fresh tissue. In this configuration, the focal area of the treatment transducer corresponds roughly to the middle of the sample holder.

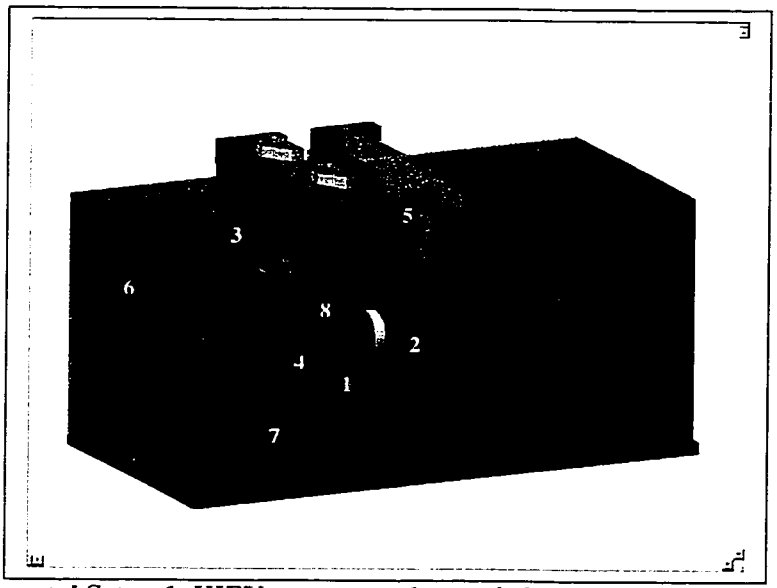

Figure 7 – Experimental Setup 1: HIFU treatment. 1-sample holder; 2-HIFU transducer; 3-imaging transducer through top transmission window; 4-lateral transmission window and needle thermocouples housing; 5-positioning system; 6-holding tank; 7- fixed reference base; 8-calipers mounted transducers.

Before HIFU treatment is commenced, the caliper mounted transducers (8) are placed in contact with the tissue through the lateral transmission window (4). Values of acoustic velocity and attenuation are obtained for the specific tissue sample from time of flight and amplitude data acquired by the transmitted signal of the caliper mounted transducers and stored. These values are used as input parameters to the numerical algorithm. The caliper mounted transducers are then removed and needle thermocouples are inserted in the sample again through the lateral window (4). Time dependent temperature data from the thermocouples are collected during the HIFU treatment and stored. An imaging probe (3) is also placed in contact with the tissue through the top transmission window to provide image feedback of the treatment focal region.

HIFU treatment is applied at 95% duty cycle (practically continuous wave) and temperature is continuously monitored by the needle thermocouples. The short time window in the duty cycle is used to avoid acoustic interference from the treatment transducer while the imaging probe interrogates the tissue sample. The goal is twofold: on one hand we are interested in monitoring the lesion development in time during treatment; on the other hand we aim to determine the appearance and formation of gas bubbles in the sample from hyper echoic regions in the ultrasound image. After the HIFU treatment is completed and the lesion formed, the sample holder (1) is removed from the treatment system and either cut immediately or placed in the freezer for about 50 to 60 minutes to freeze.

6.2 Lesion analysis setup

Analysis of the HIFU lesion is performed using two different procedures. The first procedure applies to tissue samples containing a single lesion and consists in removing the tissue from the sample holder immediately after the HIFU treatment is delivered. The tissue is then cut with a microtome blade along both the axial and transverse direction and the lesion exposed. A digital photograph of the lesion is acquired and stored for shape comparison. The lesion's length and width are also measured by a metric ruler and recorded for statistical analysis (*cfr.* Sec. 6.4). This procedure was applied to 12 samples.

The second procedure uses the setup shown in Figure 8 and applies to tissue samples containing multiple lesions (usually 4). The semi-frozen tissue[6] in the sample holder (1) is arranged in the sample holder housing (5) in front of the digital camera (4). The push rod (2) is inserted and used to advance the tissue inside the sample holder by a given distance (1 mm per full turn of the push rod). Finally, the tissue is sliced by the circular saw (3) and a picture of the remaining block of tissue is taken after each slice by the digital camera (4) and stored sequentially. This procedure was applied to 4 samples.

---

[6] A note of caution regarding the freezing step of this procedure should be in place. It has been our experience that if the tissue (fresh turkey breast in our case) was left in the freezer for a prolonged time, usually much longer than one hour, when the slicing was performed no apparent lesion was present. Since the lesion is defined as a well defined discoloration (white) area compared with the normal surrounding tissue and in light of the results from the first procedure, we speculate that when the tissue is hard-frozen its light diffraction properties change rendering the lesion "invisible". We tested this hypothesis by freezing one of the lesions from procedure one after we recorded it. After the sample froze, no lesion was distinguishable. However, after thawing the sample the lesion reappeared. In this respect, we derived the 50-60 minutes freezing time; in this period the tissue becomes hard enough to be finely cut by the circular saw and at the same time it maintains visibility of the lesion.

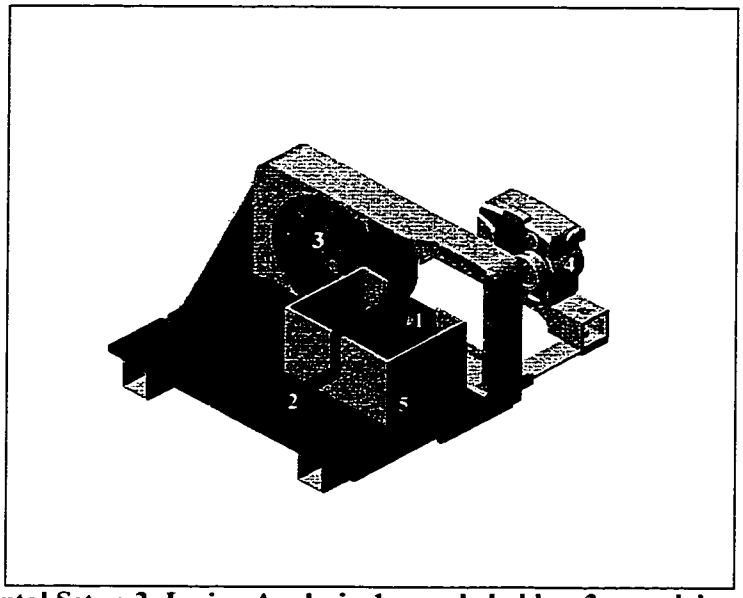

Figure 8 – Experimental Setup 2: Lesion Analysis. 1-sample holder; 2-sample's push rod; 3-circular saw; 4-digital camera; 5- sample holder housing.

6.3 Image processing and visualization

All the images acquired by the second procedure are digitally processed to extract the lesion boundaries. First the image contrast is enhanced and equalized by the application of a sliding median filter to "homogenize" the background and by subtracting it from the original image; then image morphology is applied to detect the lesion's contours.

Image morphology is a technique for image processing based on shapes. The value of each pixel in the output image is based on a comparison of the corresponding pixel in the input image with its neighbors. By choosing the size and shape of the neighborhood, a morphological operation that is sensitive to specific shapes in the input image can be constructed. The two fundamental morphological operations are dilation

and erosion. Dilation adds pixels to the boundaries of objects in an image, while erosion removes pixels on object boundaries. In the dilation operation the value of the output pixel is the maximum value of all the pixels in the input pixel's neighborhood, while in the erosion operation the value of the output pixel is the minimum value of all the pixels in the input pixel's neighborhood. The number of pixels added or removed from objects in the image depends on the size and shape of the structuring element used to probe and process the image. A two-dimensional structuring element consists of a matrix of zeros and ones and it is typically much smaller than the size of the image on which it is applied. The pixels containing ones define the neighborhood of the structuring element and the center pixel identifies the pixel being processed in the image. In this document, the input image size was 512x256 pixels and the structuring element was an 8x8 matrix as shown in Figure 16. An interactive code was written in Matlab, based on Matlab's Image Processing Toolbox, to perform the morphology operations. It also allows the user, by input-output image comparison, to discard reconstructed objects derived from inherent structures of the tissue and not related to the HIFU lesions.

0	0	0	0	0	0	0	0
0	0	0	1	1	0	0	0
0	0	1	1	1	1	0	0
0	1	1	1	1	1	1	0
0	1	1	1	1	1	1	0
0	0	1	1	1	1	0	0
0	0	0	1	1	0	0	0
0	0	0	0	0	0	0	0

Figure 9 – Structural element for image morphology

6.4 Confidence interval estimate

In the analysis of the HIFU lesions using the first procedure, the lesion's dimensions are described by a normally distributed random variable of unknown mean and variance that can be expressed in the form

$$\mathbf{x} = \eta + \mathbf{e} \tag{6.1}$$

where η is the random variable true mean and **e** is the measurement error. In our procedure only a finite number n (n=12) of experiments were performed and the measured dimensions yielded

$$x_n = \hat{\eta} + e_n \tag{6.2}$$

In this case, it cannot be concluded with certainty that the point estimated mean

$$\hat{\eta} = \frac{1}{n}\sum x_n \tag{6.3}$$

equals the true mean η. However, it can be concluded with near certainty that $\hat{\eta}$ equals η within specified tolerance limits. These limits are the endpoints of a confidence interval (η_1, η_2) of η if the probability function

$$\mathbf{P}\{\eta_1 < \eta < \eta_2\} = 1 - \gamma \tag{6.4}$$

where 100γ is the percent confidence level (Papoulis, 1991 chap. 9).

To compute the confidence interval, since the true distribution variance is not known, the sample variance is formed from the data[7]

$$s^2 = \frac{1}{n-1}\sum_{i=1}^{n}(x_i - \hat{\eta})^2 \tag{6.5}$$

From the normal distribution properties of the random variable, it follows that the ratio

$$\frac{\hat{\eta} - \eta}{s/\sqrt{n}} \tag{6.6}$$

has a Student-t distribution with n-1 degrees of freedom. Denoting with t_u its u percentile, the probability function 6.4 can be expressed as

$$\mathbf{P}\left\{-t_u < \frac{\hat{\eta} - \eta}{s/\sqrt{n}} < t_u\right\} = u = 1 - \frac{\gamma}{2} \tag{6.7}$$

which yields the confidence interval

$$\eta_1 \equiv \hat{\eta} - t_{1-\gamma/2}\frac{s}{\sqrt{n}} < \eta < \hat{\eta} + t_{1-\gamma/2}\frac{s}{\sqrt{n}} \equiv \eta_2 \tag{6.8}$$

In this document all confidence intervals are computed at the 95% level; for which the Student-t value with 11 degrees of freedom is $t_{1-\gamma/2}$=1.796.

---

[7] The sample variance s^2 is an unbiased estimate of the true variance, and it will tend to the true value of the variance as the number of samples n tends to infinity

CHAPTER 7

Acoustic Results and Validation

This chapter presents numerical solutions, solved by the algorithms described in Chap 3 and in Sec. 5.3, for the propagation of finite-amplitude acoustic waves in arbitrary media. The numerical solutions are compared both to existing analytical solutions and to experimental results to validate the correctness and accuracy of the algorithm.

Initially, results for the relaxation coefficient in different biological materials as obtained by the NLSQ fitting algorithm are presented. Then solutions for the propagation of plane waves in a homogeneous infinite medium are shown and the effects of nonlinearity and relaxation on the acoustic wave propagation described. Successively, attention is posed to classes of finite aperture transducers and arrays that can be modeled either in a 2-D or 3-D domain. A discussion on the differences, and their importance, between linear and nonlinear acoustic propagation concludes the chapter.

7.1 Material Properties and Relaxation Coefficients

As mentioned in Sec. 2.5, relaxation values for biological media are uncommon to find reported in the literature compared with those for attenuation and its frequency power laws. Values of these parameters at the frequency of 1 MHz for different media (Duck, 1990) which are used to perform the NLSQ fit to obtain the relaxation coefficients needed by the simulation are reported in Table 1. Figure 10 shows the results of the

nonlinear fit on attenuation parameters and the consequence on the phase speed of the acoustic wave for the same materials.

Table 1 – Material acoustic properties

	Water	Skin	Fat	Blood	Muscle
Sound Speed (m/s)	1500	1590	1430	1560	1570
Density (Kg/m^3)	1000	1100	928	1060	1040
Nonlinear Coefficient (B/A)	5.17	7.87	10.0	6.0	7.5
Attenuation at 1 MHz (Np/m)	0.02	28.0	7.0	2.4	6.4
Frequency Power Law $(\omega/\omega_0)^b$	2.0	1.0	1.1	1.2	1.0

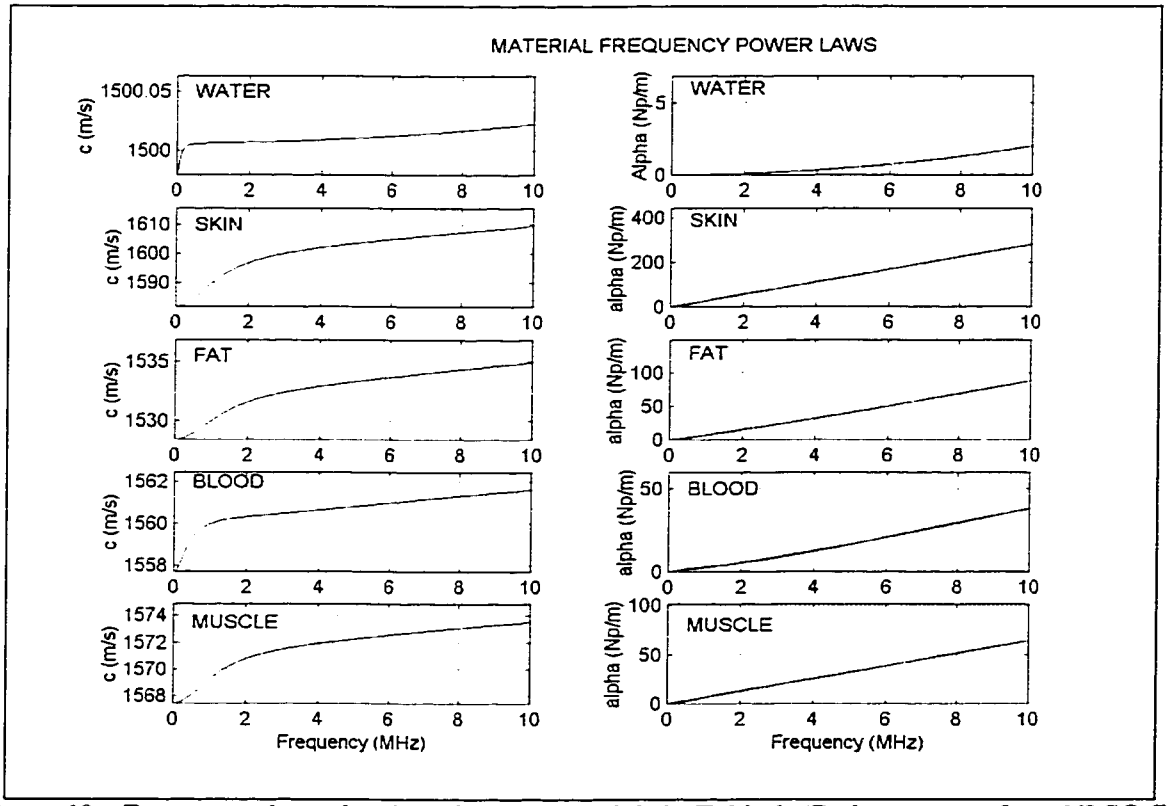

Figure 10 – Frequency dependent laws for the materials in Table 1. (Red curves are from NLSQ fit, Blue curves in the attenuation plots refers to analytical functions $\alpha(\omega) \propto \omega^b$)

7.2 Plane Waves

A plane traveling wave is defined such that all acoustic field quantities vary with time on a specified direction of propagation s but are independent of position along planes normal to the s direction (Pierce, 1989 pag.20). Hence their propagation is reduced to a one-dimensional problem ignoring both diffraction and focusing effects.

Nonlinear propagation of plane waves is governed by the well known classical Burgers Equation (Burgers, 1948)

$$\frac{\partial p}{\partial z} = Np\frac{\partial p}{\partial t} - L\{p\} \tag{7.1}$$

where L is a linear operator accounting for propagation losses and N a scaling factor for the nonlinear term. Analytic solutions to the Burgers equation can be found by using *weak shock theory* (Hamilton and Blackstock, 1998, chapter 4). When propagation losses are negligible (such as propagation in water) and the region of interest is limited to one shock distance[8] x_s, the pressure can be expanded in a Fourier series

$$p\left(\frac{x}{x_s}, t\right) = \sum_{n=1}^{\infty} B_n\left(\frac{x}{x_s}\right)\sin nt \tag{7.2}$$

where the amplitude of each harmonic component B_n can be expressed as

---

[8] The propagation distance x_s is defined as the distance where the wavefront begins to have an infinite slope, i.e. $\frac{\partial p}{\partial t} = \infty$. For a sinusoidal source, $x_s = \frac{\omega_0 \rho_0 c_0}{\beta p_0}$; it is proportional to the source frequency ω_0 and inversely proportional to the nonlinear parameter β and source pressure p_0.

$$B_n\left(\frac{x}{x_s}\right)=\frac{2}{n\frac{x}{x_s}}J_n\left(n\frac{x}{x_s}\right) \tag{7.3}$$

where J_n is the Bessel function of integer order n. In this region, B_n is basically a monotonically increasing function, with the only exception of $B_{n=1}$ which decreases from unity to a small value. This means that as the wave propagates farther from the source, harmonics are generated at the cost of the energy from the fundamental frequency component. When more harmonics grow, the waveform is distorted until the formation of a shock at $x \sim x_s$. Figure 11 shows a solution of the lossless Burgers equation for a Gaussian shaded 3.5 MHz pulse in water.

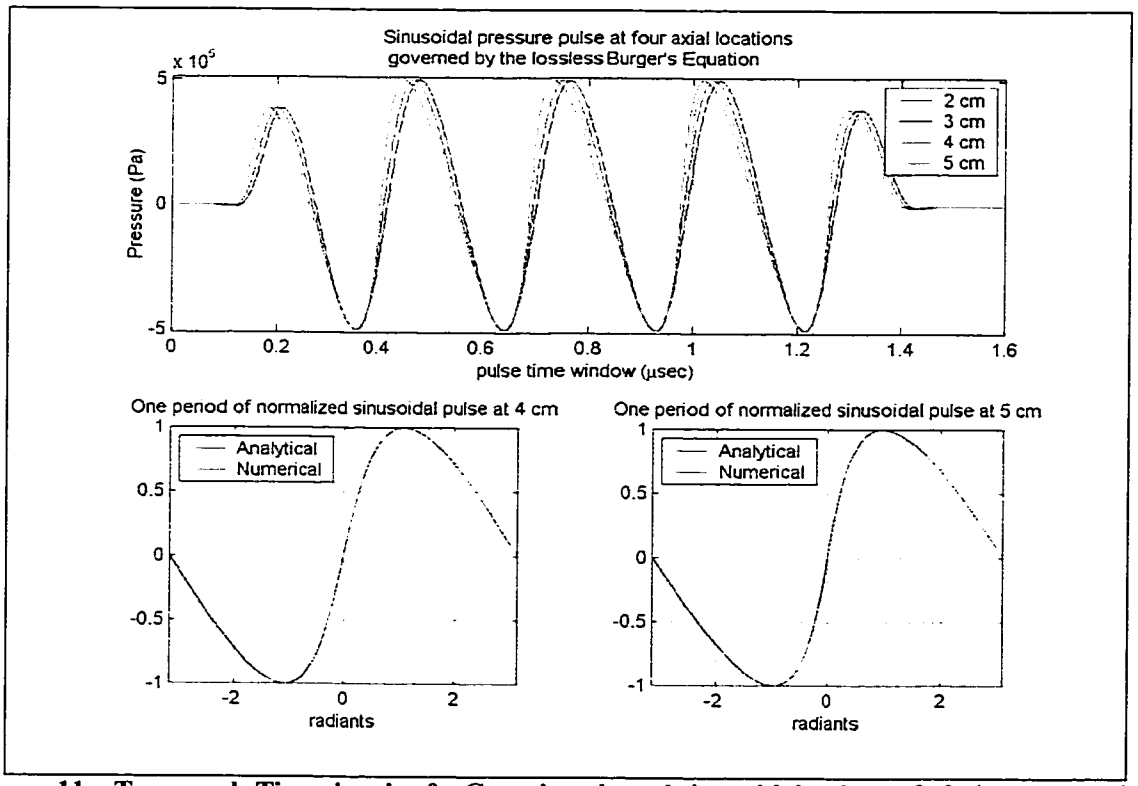

Figure 11 – Top panel: Time signals of a Gaussian shaped sinusoidal pulse at 2, 3, 4, and 5 cm from the transducer. Bottom panels: Analytical and numerical comparison of one period of the top panel signal at 4 and 5 cm on axis.

The top panel shows overlapped numerical solutions of the pulse's time signals at different distances from the source and illustrates the progressive steepening of the wavefront. The bottom panels present a single period of the pulse at 4 and 5 cm from the source and compare the analytical solutions to the numerical for validation of the nonlinear algorithm. As illustrated, the two solutions coincide well indicating the algorithm is accurate in predicting the nonlinear behavior.

A more interesting case is shown in Figure 12 where a few cycles of an infinite 4 MHz plane wave are reported after they propagated in muscle for 1.95 cm for three different cases. The first case (blue curve) is nonlinear propagation with no attenuation. The second case (black curve) is linear propagation when attenuation due to relaxation processes is considered. The third case (red curve) combines both nonlinear and attenuation processes. In the first case nonlinearity has significantly steepened the wave; however, the wave conserves its symmetry, and the amplitude (normalized to its initial value) remains constant due to the lack of any attenuation.[9] The second case, being linear, does not present any wave steepening and it is only reduced in amplitude because of the relaxation losses. Symmetry is also maintained as expected from linearity. In both cases the phase speed of the acoustic wave is fixed to the small-signal sound speed and the two waves arrive at the given distance in phase. When nonlinear propagation and relaxation

---

[9] It should be notice that for nonlinear propagation well beyond the shock formation distance the amplitude of the wave will decrease with distance even in the absence of attenuation. This results from the fact that the energy is transferred from the fundamental harmonic component to higher harmonics to maintain the shock front (c.f. Hamilton and Blackstock (1998) Chap.4)

processes are combined the third and most interesting case is obtained. The wave is reduced in amplitude, less distorted, no longer symmetric around the zero value, and propagates faster than the small-signal sound speed. These effects can be analyzed by referring to the phase speed and attenuation curves in Fig. 10. Both wave speed and attenuation increase with frequency and when the wave distorts and higher harmonics develop, these components move at a faster rate than the fundamental and are absorbed more effectively due to the increased attenuation of muscle at higher frequencies. The dispersion effects on the propagation of sound lead to the asymmetry in the wave, while the augmented attenuation on higher harmonics counteracts the tendency of the wave to steepen. In the purely nonlinear case, although we have harmonic generation, relaxation mechanisms are not included and therefore the speed at which the wave propagates is unaffected. In the purely attenuative case, relaxation is present but there is no change in the frequency content of the signal for the processes to act upon and affect the phase speed. Figure 13, showing the power spectral densities of the time signals, reinforces these concepts. In fact, it can be seen that only the fundamental frequency is present for linear propagation as expected. When comparing the nonlinear cases Fig. 13 shows indeed that in the presence of relaxation processes the higher harmonics are more strongly absorbed as indicated by the steeper negative slope associated with the peak values of the harmonic components. These results are in good agreement with those expected from theory (cfr. Hamilton and Blackstock, 1998 chap. 5 pag. 157).

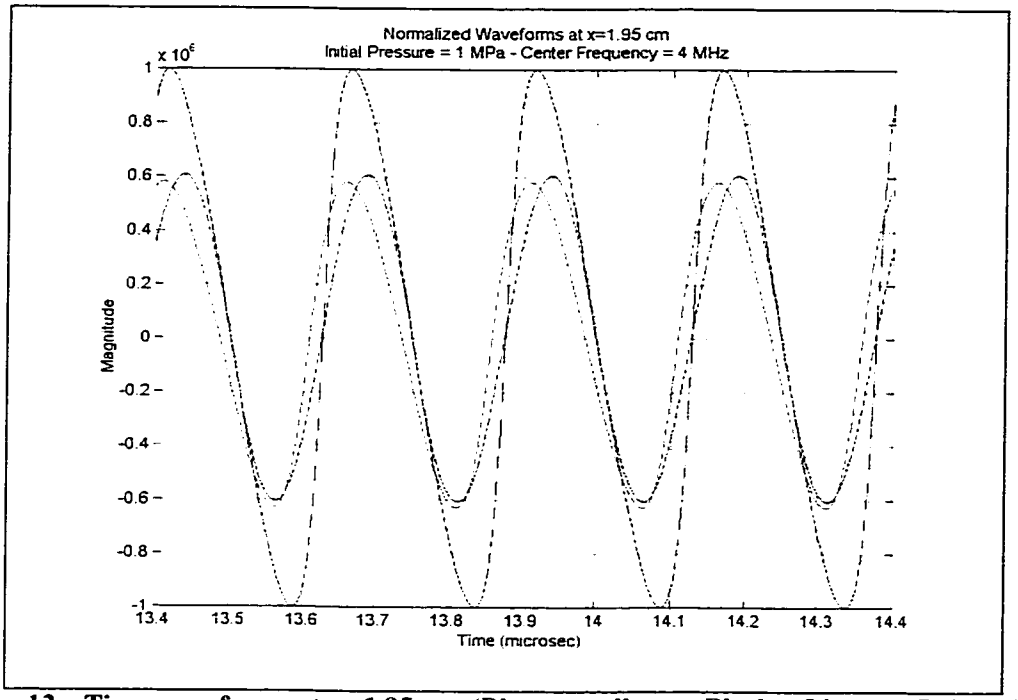

Figure 12 – Time waveforms at z= 1.95 cm. (Blue = nonlinear; Black = Linear + Relaxation; Red = Nonlinear + Relaxation)

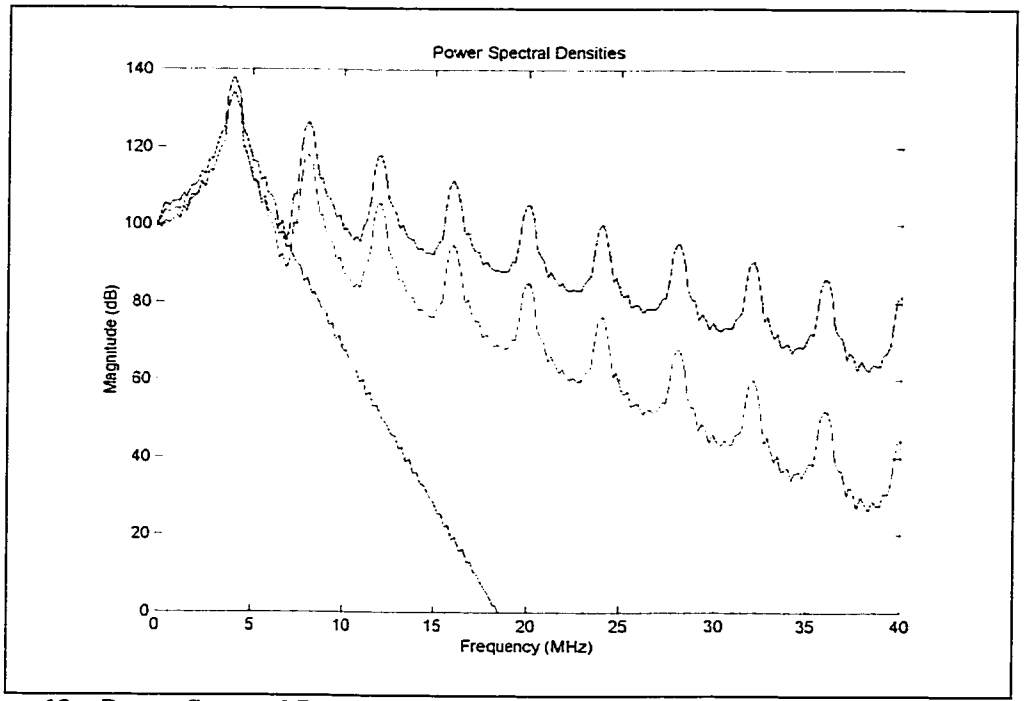

Figure 13 – Power Spectral Densities of the time signals presented in Figure 12. (Blue = nonlinear; Black = Linear + Relaxation; Red = Nonlinear + Relaxation)

7.3 Finite Aperture Transducers and Arrays

Modeling ultrasound propagation from finite transducers involves the specification of several classes of parameters. The characteristics of the transducer (i.e. driving frequency, aperture, phasing, number of elements, etc.) as well as the characteristic of the medium (i.e. homogeneous/inhomogeneous, geometric features, nonlinear behavior, etc.) need to be designated. Different combinations of these values lead to different acoustic propagation fields and effects and make each case a unique one. Although we investigated several propagation problems, here we present details only for selected cases. The choice of the particular cases is based on the application of interest (imaging or therapeutic) and on the extended complexity of the problem, which requires the use of most of the topics discussed in previous chapters.

7.3.1 1-D Arrays

One dimensional arrays are commonly used in commercial ultrasound machines for imaging purposes. As described in chapter 4, the 1-D array's element height is usually small compared with the length of the full array and, if the mechanical focus is relatively far from the region of the electronic focus, they can be model in a two dimensional domain. An important imaging modality that has gained much popularity in recent years is tissue harmonic imaging. This technique exploits the nonlinear propagation characteristics of the sound wave to improve both the axial and lateral

resolution of the ultrasound image by only processing the second harmonic component of the received signal. The developed acoustic model is fully capable of simulating such scenarios and to provide important information about possible maximum image resolution and its location. As an example, Figure 14 shows the numerically obtained spatial beam patterns associated with the first three harmonics for a 2 cm aperture linear array driven at 1 MHz and electronically focused at 3 cm.

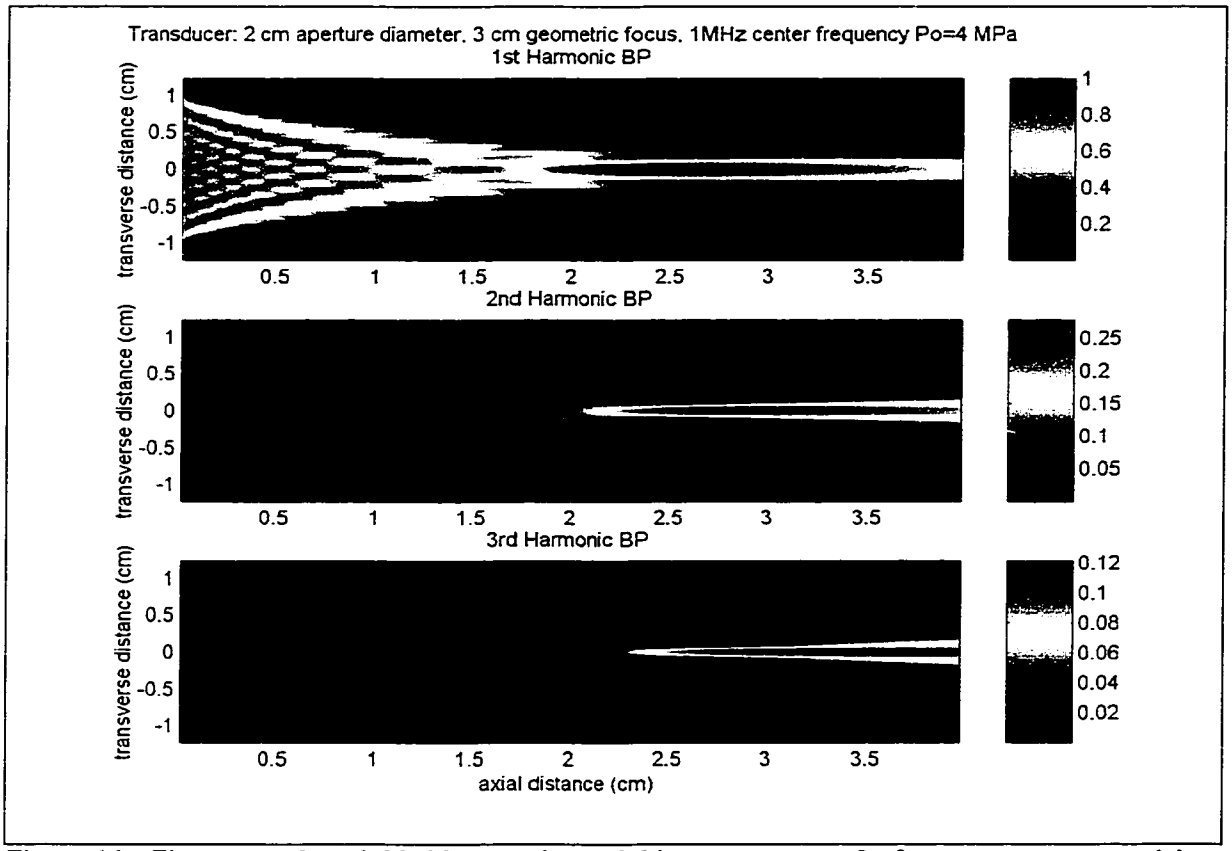

Figure 14 – First, second, and third harmonic spatial beam patterns of a 2 cm aperture array driven at 1MHz normalized to maximum value of the fundamental.

Three main features are immediately evident: first, the beam patterns associated with the higher harmonics are more tightly focused with respect to the fundamental and both their

lateral and axial dimensions become successively smaller. This feature is responsible for the augmented resolution in the image. Second, most of the higher harmonics start developing near the focal region and are well localized; and third, their patterns do not present the strong "finger-like" characteristic found in the pattern for the fundamental frequency, thus providing a much "cleaner" point spread function with greatly reduced side lobes.

In the introduction to this section, the uniqueness of every nonlinear propagation problem and its dependence on many variables was mentioned. Some of these variables are directly related to the characteristics of the physical arrays used and are fixed at the time of manufacture. The simulation software developed in this document can be an excellent tool for the planning and development of transducer arrays specifically optimized to take full advantage of the acoustic nonlinear properties.

7.3.2 2-D Arrays

Two-dimensional arrays find their major employment in the field of therapeutic ultrasound. The transducers' dimensions, contrary to 1-D arrays, are comparable to each other and therefore this type of arrays provides a much greater focusing gain that makes them especially well suited for high intensity applications.

Two interesting areas of high intensity ultrasound that have in recent years gained much popularity are acoustic hemostasis, whether extracorporeal or *in situ*, and noninvasive treatment and/or ablation of localized tumors. The following numerical

examples of the predicted acoustic field variables, shown in Figure 15 through Figure 18, are related to these particular applications.

Figures 15 and 16 refer to the acoustic hemostasis case. The transducer, a spherical section single element, has an aperture of 15 mm in diameter, its radius of curvature is also 15 mm, and it operates at 1 MHz. Propagation is through liver tissue where a 2 mm in diameter blood vessel is present. Inside the vessel, blood flows at 6 cm/s with a parabolic profile. The spatial distribution of the time-averaged intensity (Figure 15) and heat rate (Figure 16) are presented for the two orthogonal planes on the transducer's axis. It is interesting to notice that in the y-z planes (horizontal cuts, upper panels in the figures) the vessel is acting as a converging lens because of its curvature and impedance mismatch with the liver tissue. In fact, both the time-averaged intensity and especially the heat rate are narrower than their profiles in the x-z planes (vertical cuts, lower panels in the figures) where the vessel is linear. Furthermore, although acoustic power is present inside the vessel, the absorption coefficient of blood is very small (blood is composed of many red blood cell that scatter most of the acoustic energy) and as a result the heat rate distribution inside the vessel is also minimal. These occurrences underline the importance of biological structures in the field of propagation of the ultrasound beam.

Acoustic simulations for noninvasive treatment of tumors are presented in Figure 17 and Figure 18. In this example, multi layers propagation is used to simulate prostate cancer treatment (layer types are specified in the figures). The transducer, a 4 MHz

spherical section single element of 30 mm aperture diameter and 30 mm focal length, is situated in the rectum and coupled to the rectum wall through a layer of water. In this case, the layers are infinite in cross section and therefore the acoustic field pattern in the y-z and x-z planes are identical because of axial symmetry. Consequently, only one such plane is shown in the figures.

Due to the high gain of the transducer, both time-averaged intensity and heat rate are well localized in the focal region with no significant energy deposited along the propagation path in the intermediate tissue layers. A small localized focus at high intensity levels and low energy levels in the transmission layers are indeed the fundamental concepts of ultrasound mediated noninvasive surgery. Once again, the developed algorithm can be used to better design therapeutic applicator transducers or treatment protocols and to fully exploit nonlinear properties of the acoustic wave that undoubtedly arise in such high intensity regimes[10] (*cfr.* Sec. 7.3.4 and Sec. 8.5).

---

[10] For temperature and lesion results pertinent to the above cases refer to Section 8.5

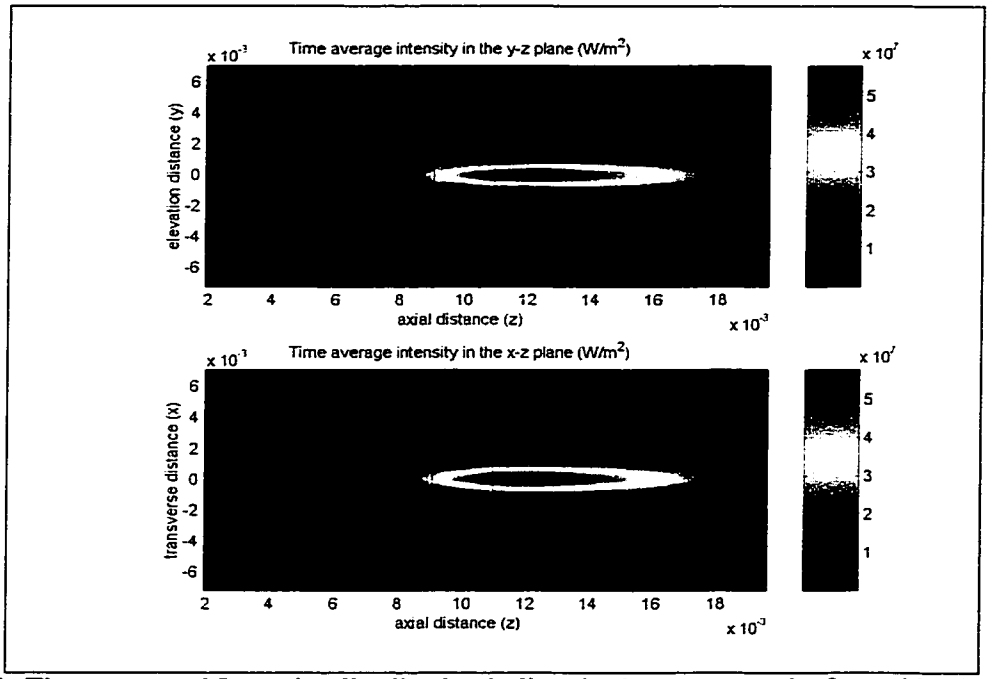

Figure 15– Time-averaged Intensity distribution in liver in the presence of a 2 mm blood vessel with 6 cm/s parabolic flow. The vessel is located right before the focal region

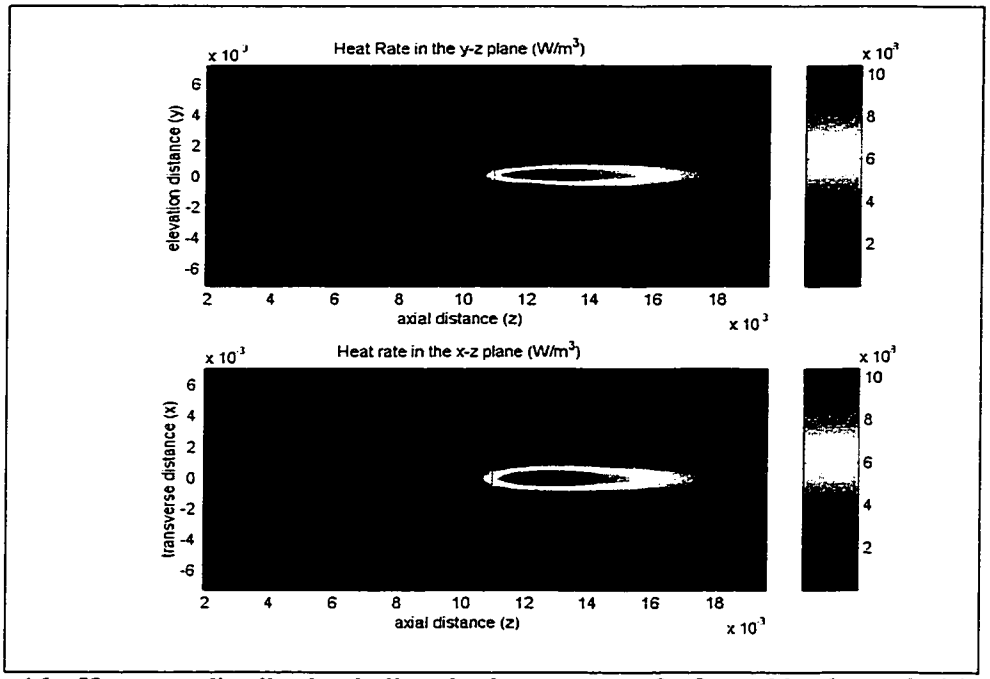

Figure 16 – Heat rate distribution in liver in the presence of a 2 mm blood vessel with 6 cm/s parabolic flow. The vessel is located right before the focal region

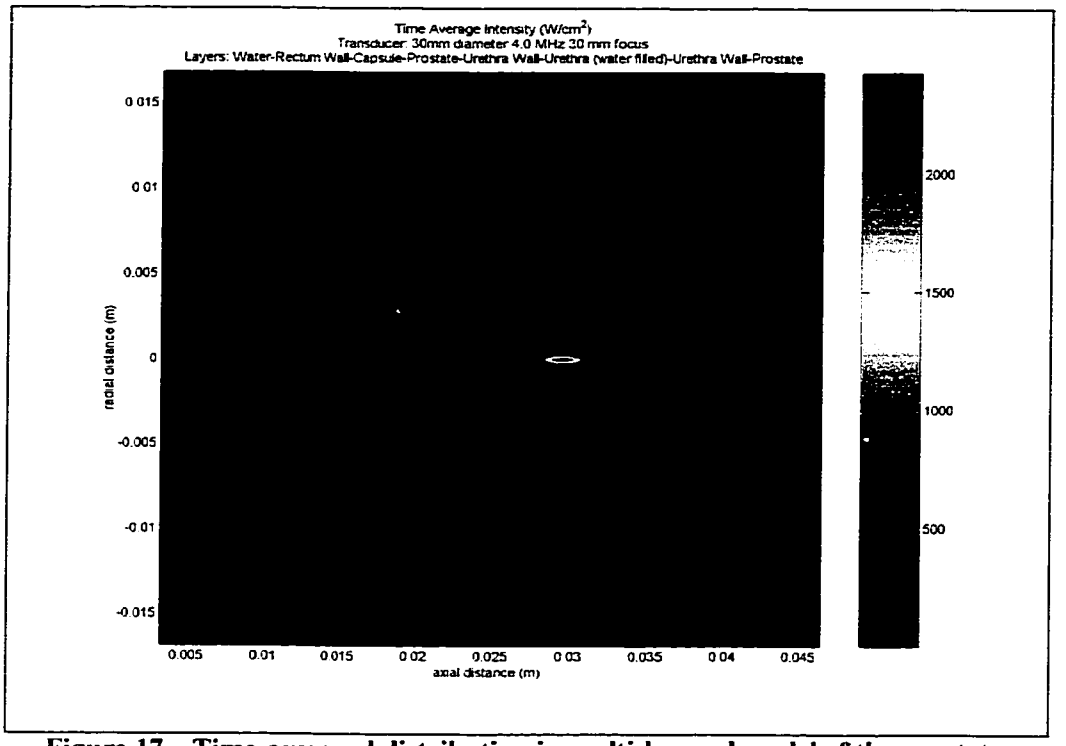

Figure 17 – Time-averaged distribution in multi-layered model of the prostate

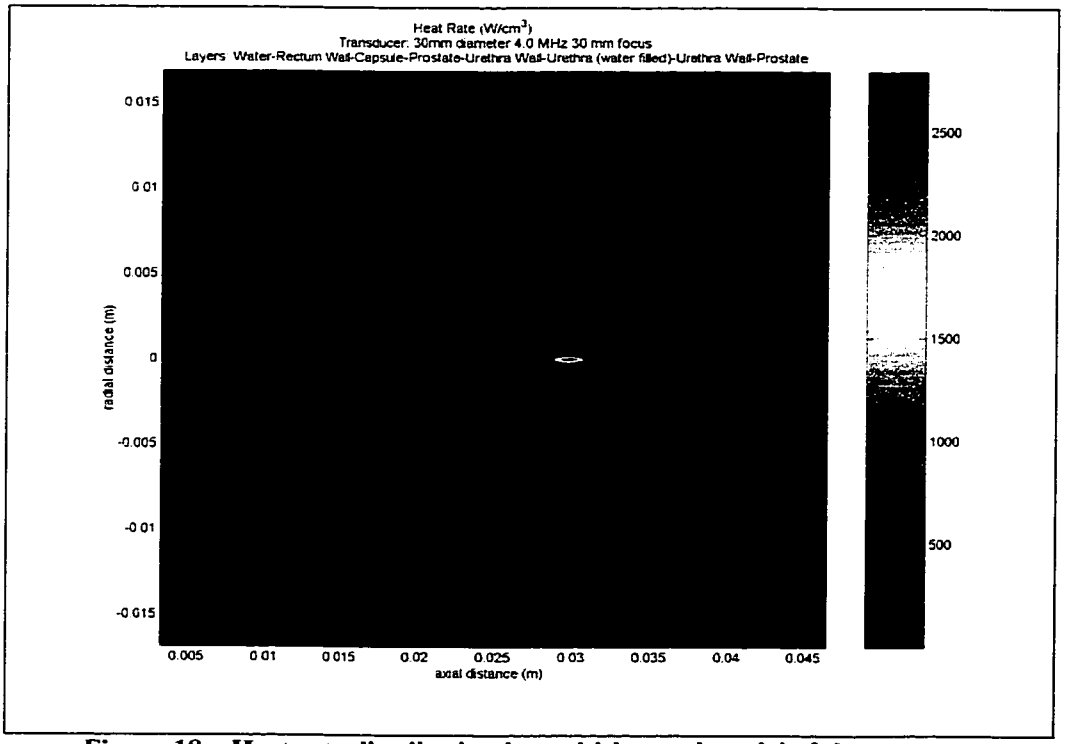

Figure 18 – Heat rate distribution in multi-layered model of the prostate

7.3.3 The experiment treatment transducer

The transducer used in the tissue experiments is a spherical single PZT element of 23 mm aperture, 35 mm radius of curvature (geometric focus) operating at a central frequency of 3.5 MHz and manufactured by Sonic Concepts, Woodinville, WA. Except for the axial beam plot data where a 5 cycles sinusoidal pulse was used, all the experiments in which a lesion was formed were carried out in continuous wave (CW) mode with 40 W electrical power applied to the transducer. The efficiency of the transducer was measured by a radiation force balance method and found to be about 60 % (*cfr.* Appendix A). The input initial conditions to the algorithm accounted for the transducer efficiency. Figure 19 shows the computed spatial distribution of the time-averaged intensity and heat rate generated by this transducer configuration in muscle. The transducer's acoustic power is mainly concentrated in the focal region and reaches a maximum value of 700 W/cm^2. The time-averaged intensity focal dimensions at the –3 dB level (approximately 70% of the maximum power corresponding to the extended red area in Fig. 15) are about 5.5 mm in length and 0.75 mm in width. The power absorbed by the tissue (heat rate) reach a maximum value of about 500 W/cm^3 and it is more tightly concentrated around the focus than the time-averaged intensity. Indeed, the heat rate focal dimensions at the –3B level only extend 3.5 mm in length and 0.4 mm in width. These values of power are smaller compared to the usual values of 1700 W/cm^2 used by several investigators to produce lesions in bovine liver or other tissues (ter Har et al.1989, Fry et al.,1995).

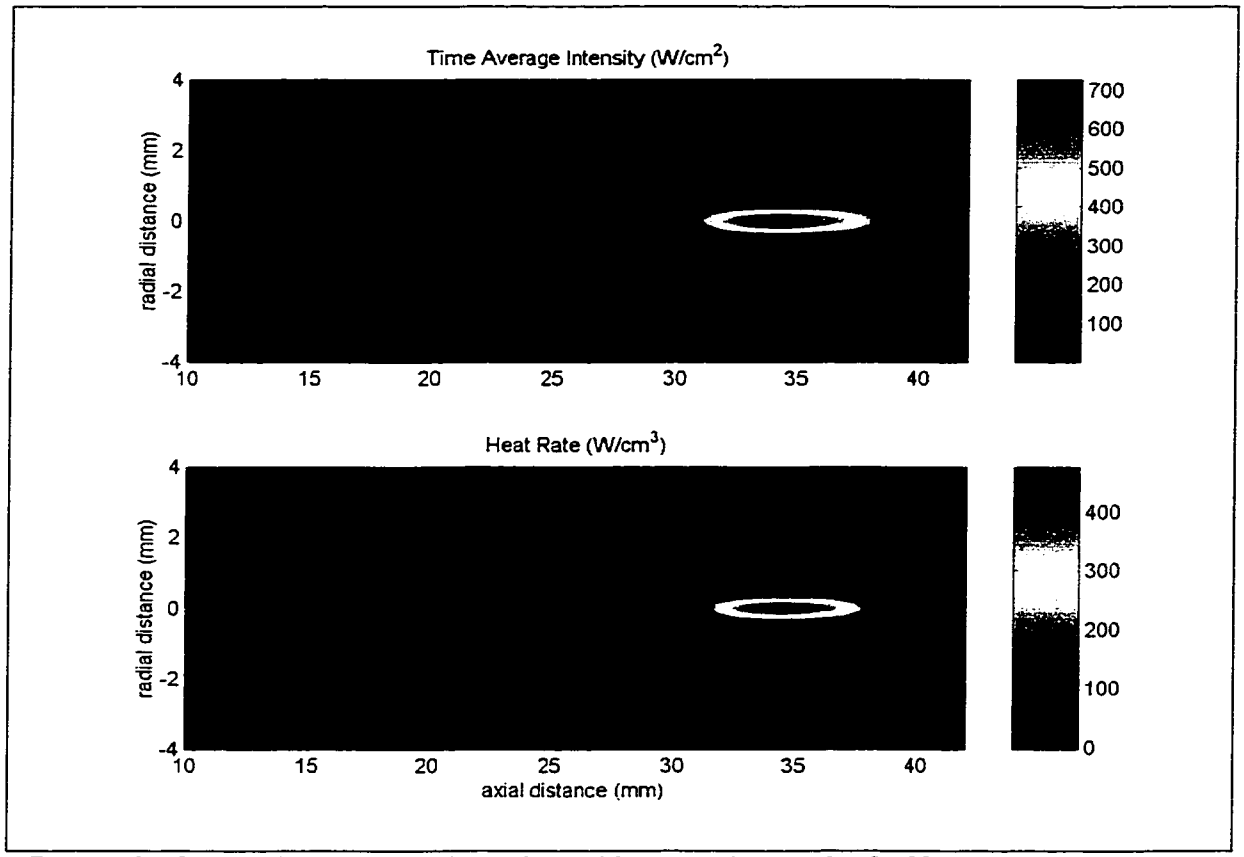

Figure 19 – Spatial time-averaged intensity and heat rate in muscle of a 23 mm aperture , 35 mm radius of curvature spherical transducer operating at 3.5 MHz.

However, they usually experience bubble activity during their treatments that drastically changes the extent and shape of the acoustically induced lesion. In this document the aim is to create extremely consistent lesions that are only a result of temperature effects. It will be shown in Chapter 8 that the level of power in Figure 19 serves this purpose well.

The numerical solution of the pressure's axial beam pattern is compared with both experiment and the analytical solution in Figures 20 and 21. As illustrated in Figure 20, the numerical curve accurately predicts the experimental curve in the focal region as well as the prefocal axial nulls. The local maxima in the prefocal region are slightly

overpredicted by the numerical solution. These discrepancies may be due to nonuniform excitation across the surface of the transducer or may be related to the short length of the pulse used (5 cycles). Similar differences are also seen in previous works (Hutchins et al., 1987; Baker, 1992). When compared with the analytical solution (O'Neill, 1945), the algorithm is capable of predicting with high accuracy also the nulls of the fast varying field close to the transducer's face; a property that most of the KZK-based models lack. The discrepancy in amplitudes in the near field maxima is due to the algorithm initial conditions. The numerical solution assumes a uniform pressure distribution on the face of the transducer while the analytical solution is based on a uniform distribution of normal velocity. How fast the two solutions converge depends on the parameter ka, k being the wave number and a radius of the transducer's aperture (see appendix B).

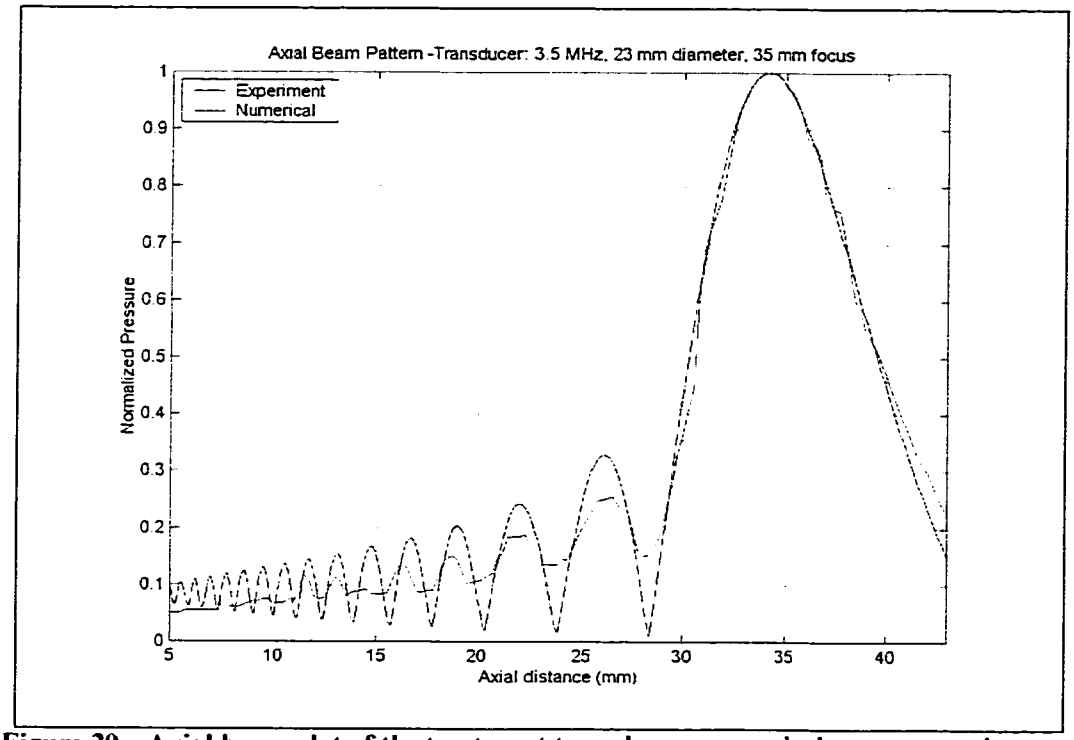

Figure 20 – Axial beam plot of the treatment transducer: numerical versus experiment

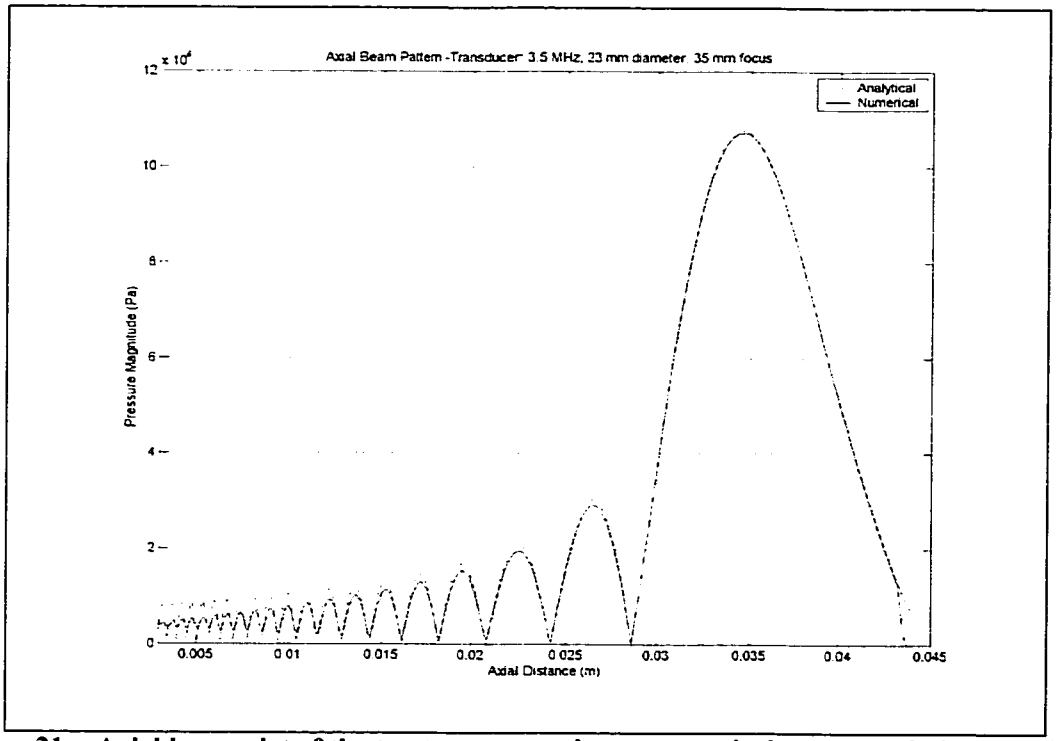

Figure 21 -- Axial beam plot of the treatment transducer: numerical versus analytical solution

7.3.4 Linear versus nonlinear propagation: quantifying the differences

Nonlinear effects, as mentioned previously, are important in correctly predicting acoustic field variables and distributions. A comparison of the predicted acoustic fields for linear and nonlinear propagation in muscle is reported in Figures 22, 23, and 24 for the HIFU treatment transducer used in the experiments and described in the previous section. The predicted axial pressure distribution is shown in Figure 22. At small-signal levels (linear case) the waveforms are sinusoidal, the positive and negative pressure amplitudes are identical and independent of position along the propagation path (the green curve describing the linear pressure field envelope is included to emphasize and better visualize the concept). In the nonlinear case, however, waveform steepening occurs and asymmetric waveforms are predicted in the transducer's focal region. The magnitude of the maximum positive pressure is about 40% higher as compared to the linear case, whereas the magnitude of the maximum negative peak is reduced by a 30% factor. This type of asymmetry is related to the interaction of nonlinearity and the dispersion properties of the tissue (Swindel, 1985).

The most important characteristics of the acoustic field for temperature and lesion predictions are, however, the intensity and heat rate distribution. Their respective axial and lateral distributions are presented in Figures 23 and 24. Figure 23 shows that the time-averaged intensity distribution is weakly affected by nonlinear propagation.

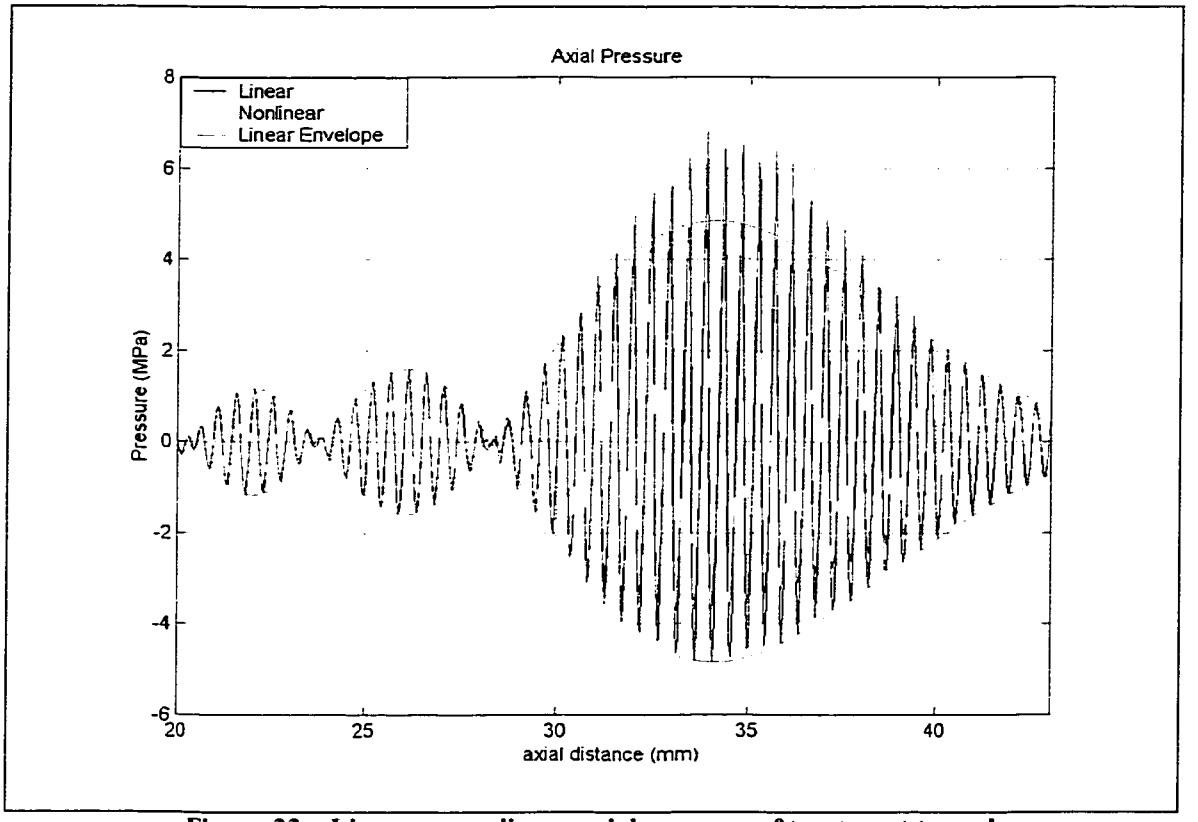

Figure 22 – Linear vs nonlinear axial pressure of treatment transducer

At the moderate power level at which the treatment transducer is driven, there is only a slight enhancement of intensity (of the order of few percentage points) due to nonlinearities and it is strongly localized at the focus. Except for this occurrence, no significant differences are found in both the axial and lateral patterns.

In contrast, the heating rate distributions in Figure 24, show a strong dependence on nonlinear effects. There is a critical increase in heating rate at the focus of about 70% more energy than predicted by linear theory. At the same time, both the axial and lateral dimensions of the focal region are reduced thus providing tighter focusing as shown by the normalized curves.

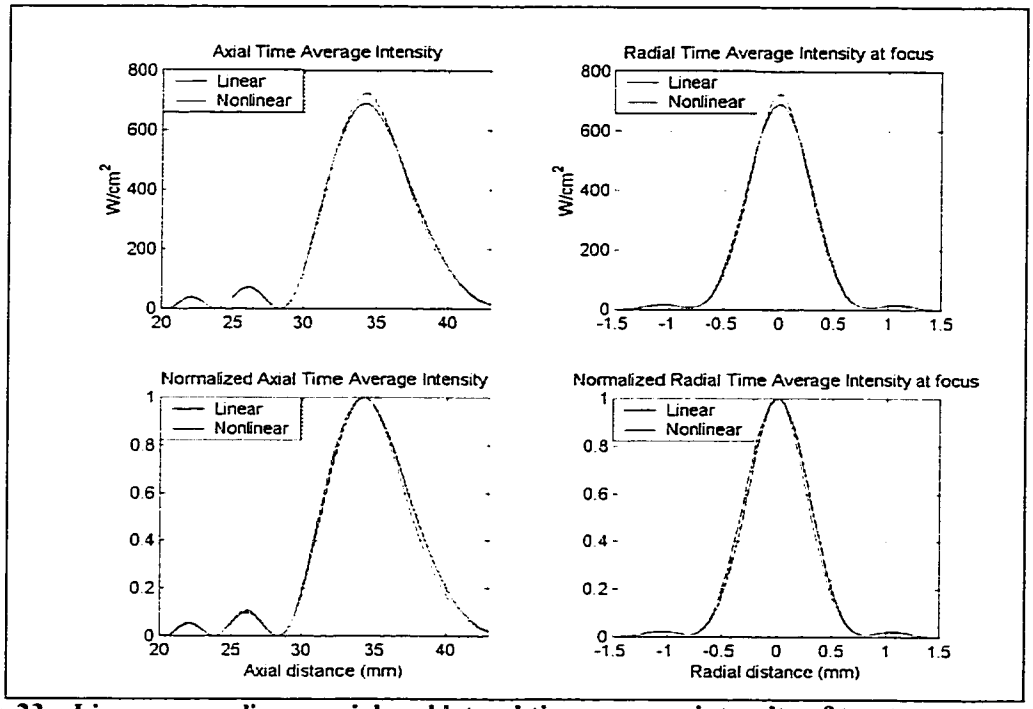

Figure 23 – Linear vs nonlinear axial and lateral time average intensity of treatment transducer

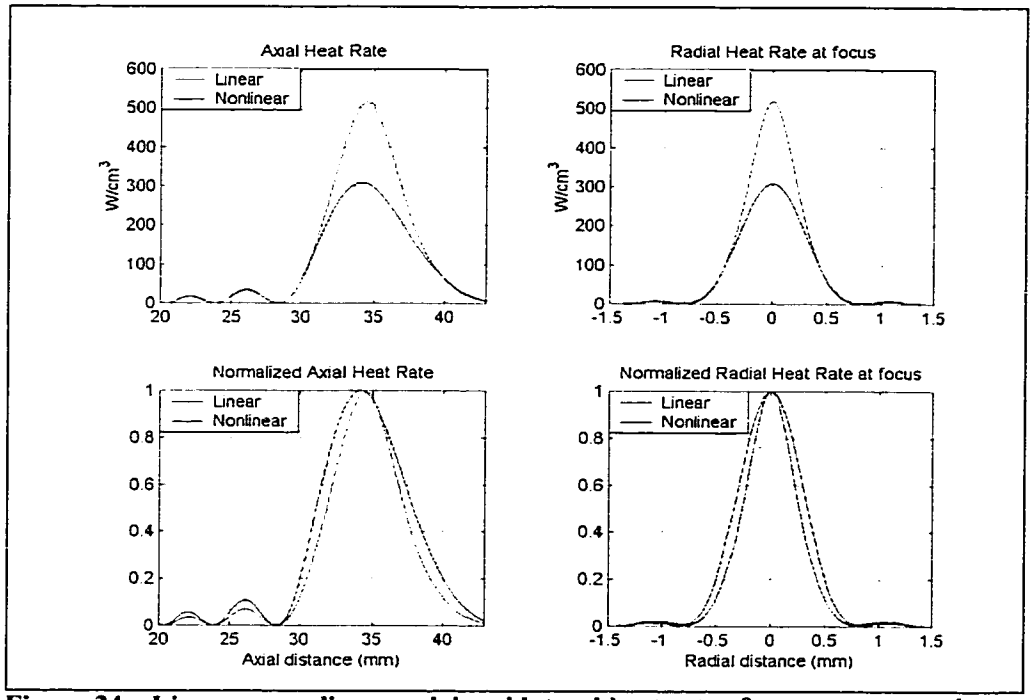

Figure 24 – Linear vs nonlinear axial and lateral heat rate of treatment transducer

The axial heat rate dimension at the –3dB level is 3.5 mm when nonlinearities are considered and 5.5 mm when ignored, resulting in approximately a 36% reduction in size. The radial dimension is reduced from the linear propagation value of 0.5 mm to the nonlinear propagation value of 0.4 mm yielding a 20% difference. Furthermore, the magnitude of the heating rate associated with nonlinear propagation also presents a one third (33%) reduction in the prefocal area when compared to that for linear propagation. From these results it is clear that nonlinear effects provide a useful method of generating a very localized thermal impact on tissue and are extremely important both for the planning and the outcome of the ultrasound treatment. For a desired energy level at the focus, they can reduce the effective dimensions of the localized region at a high energy level as well as limit the energy deposited along the propagation path.

CHAPTER 8

Temperature and Lesions Results and Validation

The main topic of this chapter is a report and a comparative analysis of HIFU-induced temperature and lesion development for both numerical and experimental results in fresh turkey breast.

The chapter begins with the definition of an acoustically induced lesion both for the experiments and for the numerical code in Section 8.1 and 8.2, respectively. A presentation of the experimental results is provided in Sec. 8.3, while a full comparative analysis between numerics and experiments is the topic of Section 8.4. Section 8.5 concludes the chapter with the illustration and discussion of selected treatment scenarios solved numerically.

8.1 Defining thermal damage and lesions

When high intensity ultrasound is absorbed by biological tissue, a lesion is produced by means of coagulative necrosis. Once a threshold temperature or thermal energy is reached, irreversible changes in the biological environment occur which render cell survival impossible. These changes may correspond to break down of enzymes, to protein denaturation, or cell membrane damage in general. Macroscopically, the region of tissue that underwent these changes appears as a discolored bright white area in contrast to the pinkish background color of the untreated tissue. This discolored, or

"cooked", region delimits the acoustically induced damage and is defined in this document as the HIFU lesion. Figure 25 shows an example.

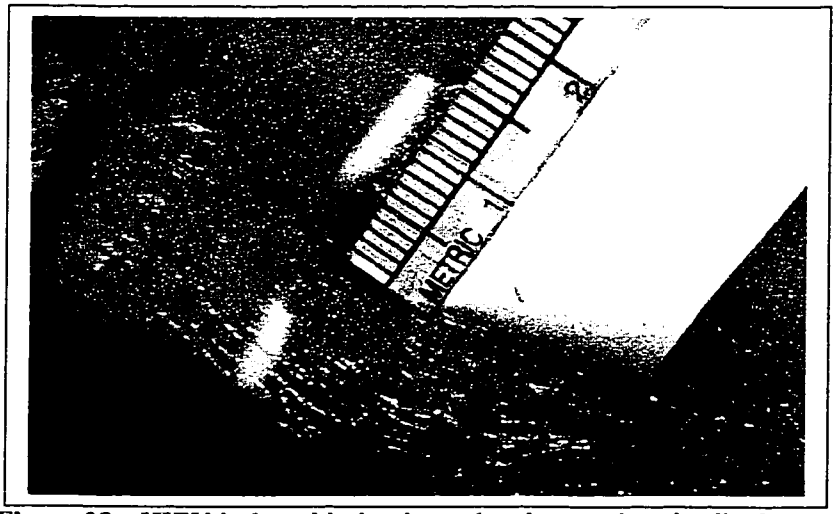

Figure 25 – HIFU-induced lesion in turkey breast: longitudinal cut.

8.2 Numerical prediction of the HIFU induced lesion: Thermal Dose

The protocol used in the numerical algorithm to estimate tissue damage and lesion formation in tissue follows the concept of thermal dose developed by Separeto and Dewey (1984). Their proposed method is based on a first order model that quantifies the dynamics of the heating of tissue and the extent of cell killing by a well defined dose parameter. Primarily developed for comparisons of different cancer therapies studies in hyperthermia applications, the method converts the temperature history of the treated tissue and its approximate reaction parameters into an equivalent thermal dose. The dose is specified by the exposure time in minutes at a given constant temperature. Their proposed equation for thermal dose, expressed in equivalent minutes at a constant temperature of 43 °C is

$$TD_{43} = \sum_{t=0}^{t=t_{final}} C^{(43-T(t))}\Delta t \qquad (8.1)$$

where $T(t)$ is the time dependent temperature in degrees Celsius for a particular spatial point, and the constant C has the value of 0.25 below the temperature of 43 °C and 0.5 above it. As expressed by Eq. 8.1 through the time integration operator, the thermal dose maintains memory of the temperature distribution during the whole length of treatment, thus providing a more accurate approximation of tissue damage than the one obtained by simply considering a single temperature threshold value[11]. In this document, a numerical lesion is formed for values of thermal dose exceeding 120 minutes at 43 °C.

8.3 *In vitro* experiments on turkey breast

In vitro experiments on fresh whole turkey breast were performed using the treatment system described in Chapter 6. Prior to experiments, the turkey breast was freed from the rib cage and stored in degassed phosphate buffered saline (PBS) maintained at a constant temperature of 37 °C. After the tissue equilibrated to body temperature, it was removed from the PBS solution on a need basis and samples of roughly 5x5x7 cm were cut and mounted in the sample holders. In order not to introduce bubbles, the mounting of the tissue was performed underwater in the holding tank. On several samples both the sound speed and attenuation were measured and found to be respectively 1578±8 m/s and 0.31±0.02 Np/cm at 3.5 MHz; very consistent between

measurements. HIFU treatment was delivered with the modalities described in Section 6.1 and power level described in Section 7.3.3 for exposure times of both five and ten seconds.

The treatment sessions were continuously monitored on different occasions by the ATL HDI 1000 real-time ultrasonic imaging system operating in B-mode. No hyperechogenic zone was observed in any of the trials implying that no bubble activity occurred. In fact, a hyperechogenic zone is usually produced by cavitation-induced microbubbles in the focal region and they can drastically change the shape and size of the HIFU-induced lesion. To further confirm this result, some lesion examples from the single lesion experimental procedure are shown in Figure 26.

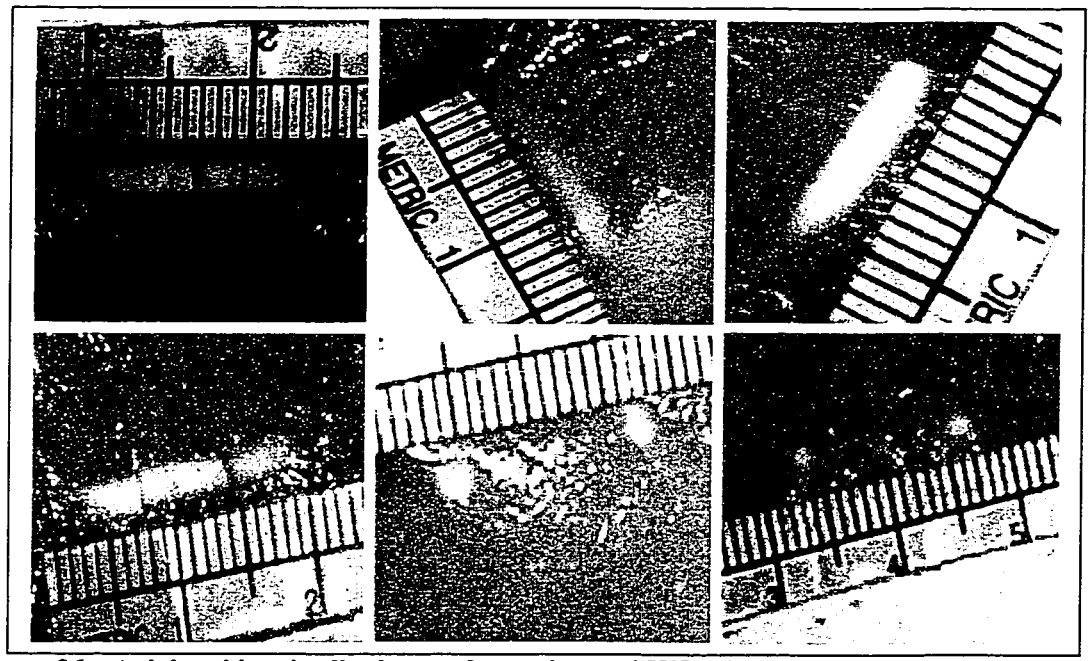

Figure 26 – Axial and longitudinal cuts of experimental HIFU-induced lesions in turkey breast

---

[11] Generally, for fast heating both the thermal dose and threshold temperature approach converge to the same lesion profile. However, if heating is slow the thermal dose method is best suited to predict a lesion.

The experiments produced uniform lesions conforming to the typical "cigar" shape correlated exclusively to thermal effects as opposed to the "tadpole" shape characteristic of cavitation mediated effects. After treatment, the tissue was removed from the sample holder and the lesion's dimensions recorded (*cfr.* Sec. 6.2).

The same procedure described above was applied in the case of multiple lesions created in the same tissue sample. Figure 27 illustrates four sequential tissue slices obtained by the second procedure detailed in Section 6.2. The horizontal lesions were created by a five seconds exposure while the vertical ones by a ten seconds exposure. Image morphology was applied to the pictures of the tissue slices and the lesions reconstructed in three dimensions for volumetric comparison to the lesions predicted by the algorithm. Figure 28 shows the process.

To maximize the experimental precision and account for animal to animal variability, experiments were carried out over several weeks. The results and conclusions from experiments as well as the validity of the computer model are detailed in the following section.

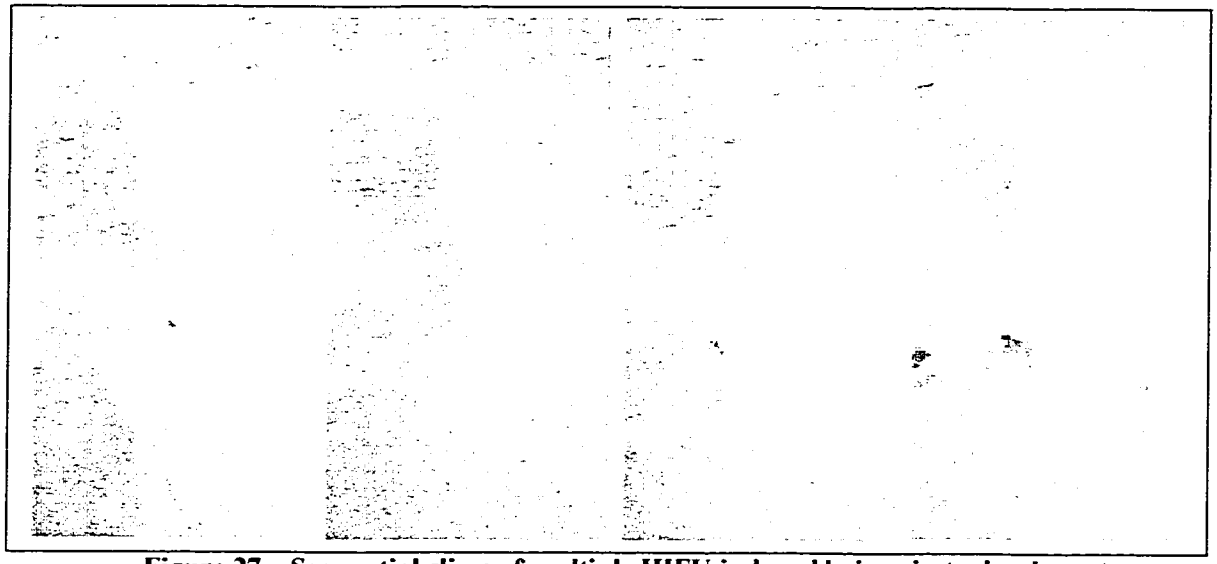

Figure 27 – Sequential slices of multiple HIFU-induced lesions in turkey breast

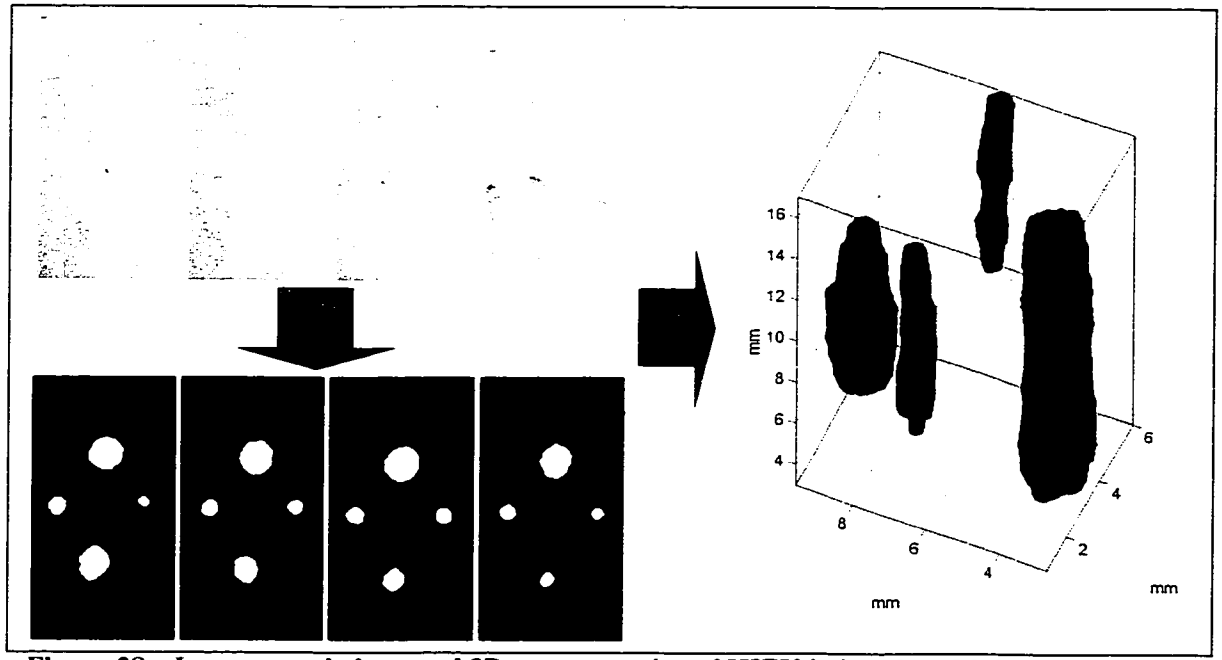

Figure 28 – Image morphology and 3D reconstruction of HIFU-induced multiple lesions in turkey breast

8.4 Numerical and experimental comparative analysis

The experimental conditions were recreated numerically by turning off both perfusion and advection effects in the bio-heat solution part of the algorithm (*cfr.* Sec. 5.2). The thermal parameters used for the simulation of muscle tissue (turkey breast) are respectively 3430 J/kg°C for the heat capacity and 0.48 W/m°C for the thermal conductivity, as reported by Duck (1990). A background temperature of 37 °C was used to initialize the model. Figures 29 and 30 show sequential temperature and lesion evolution profiles as a function of time. Although the maximum temperature reached at the focus is greater than 100 °C (especially true for the 10 seconds HIFU exposure time), the pseudocolor images in Figure 29 are allowed to saturate at 100°C to enhance the spatial extent of the temperature distribution as treatment time increases.

These sets of data illustrate that HIFU-induced lesions grow rapidly at first, and then less rapidly, as predicted by the theory. In fact, in these particular cases only heat diffusion is present which reduces the solution of the bio-heat equation to a simple exponential function of general form $1-e^{-kt}$, where k indicates the diffusion time constant and t is time. In the beginning of treatment, although stronger temperature gradients exist, diffusion processes are not fast enough to carry the heat away. Afterwards, weaker temperature gradients together with well developed diffusion tend to bring the solution towards its asymptote.

An enhancement of the thermal dose lesions and temperature contours at both 5 seconds exposure and 10 seconds exposure is illustrated in Figures 31 and 32. As depicted, in both cases a temperature contour of 57 °C is approximately equivalent to the same area predicted by thermal dose calculations and for fast heating can be used as a rule of thumb to predict lesion boundaries (*cfr.* Footnote 11). Comparing the two lesions, 10 seconds HIFU exposure produces a 45% longer axial lesion than the 5 seconds treatment. Widthwise, the minimum distance (right side, farther from the transducer) is about the same. However, the maximum width associated with 10 seconds exposure (left side, closer to the transducer) is 118% bigger that its 5 second counterpart. In fact, while the 5 seconds lesion roughly maintains it cylindrical shape, the 10 seconds one is greatly augmented in the prefocal area. Prefocal side lobes in the spatial distribution of the heat rate (*cfr.* Figure 19) are responsible for this effect. The longer exposure time allows side lobes of the beam to contribute to the thermal dose values in excess of 120 minutes at 43 °C in this region, which is not the case for the shorter treatment time. The validity of these results is confirmed both in Table 2 and Figures 33 and 34.

Table 2 reports experimental measurements of axial and cross sectional dimensions for lesions from both treatment protocols. Statistical values at the 95% interval are constructed for each variable set and compared to the numerical prediction from the model. The algorithm slightly overestimates both the length and the width of the lesion obtained by a 5 seconds HIFU exposure. The predicted lesion is about 1.24 mm longer and 0.19 mm wider than the upper limit of the confidence interval. On the

other hand, numerical results for a 10 seconds HIFU exposure agree extremely well with the experiments. The predicted values fall well inside the limits of their confidence interval with the only exception being the maximum value of the lesion cross section which is overestimated by 0.27 mm. Human measurement accuracy and metric ruler resolution (0.5 mm max resolution) is the probable cause for the submillimeter discrepancies found in the lesion' s lateral dimension. On the other hand, the differences found for the 5 seconds treatment in the lesion's axial length can possibly be explained by background temperature initial conditions. Some of the tissue samples at the time of treatment may have not yet completely equilibrated to 37 °C and therefore a lesion slightly smaller than average was produced in the samples. As a result, the estimation of the confidence interval was shifted towards a smaller mean. This concept may also be applied to account for the variance of the lateral dimension.

The numerical and experimental thermal lesions are presented in three dimensions in Figure 33 and Figure 34 for both HIFU treatment times. The volume reconstructed lesions agree quite well with each other. Indeed, the respective experimental lesions accurately match both the cylindrical shape predicted by the algorithm at 5 seconds exposure, as well as the lesion's approximate conical shape that develops after a treatment of 10 seconds. It is obvious that the experimental lesions' length in the figures is shorter than the numerically computed one. However, it is clear from the same figures that a few slices at the top of the lesions are missing. They could not be reconstructed

due to strong noise in the pictures (mostly fatty areas in the tissue that also appears white in color).

To further test the simulation model, thermocouple measurements of the temperature development in time were taken at 30 mm along the transducer axis during insonation. The chosen location corresponds to the point right after the initial rise of the main lobe in the heat rate axial pattern (*cfr.* Figure 24). The measurements were compared with numerical temperature histories at the same axial point and illustrated in Figures 35 and 36 as variation from the background temperature. As shown, an exposure to HIFU for 5 seconds results in a maximum temperature increase of about 50 °C. A maximum of 70 °C is instead obtained at the same location for a 10 seconds HIFU session. Numerical solutions agree remarkably well with the experiments for both cases, accurately predicting both the rising and decaying exponential time constants.

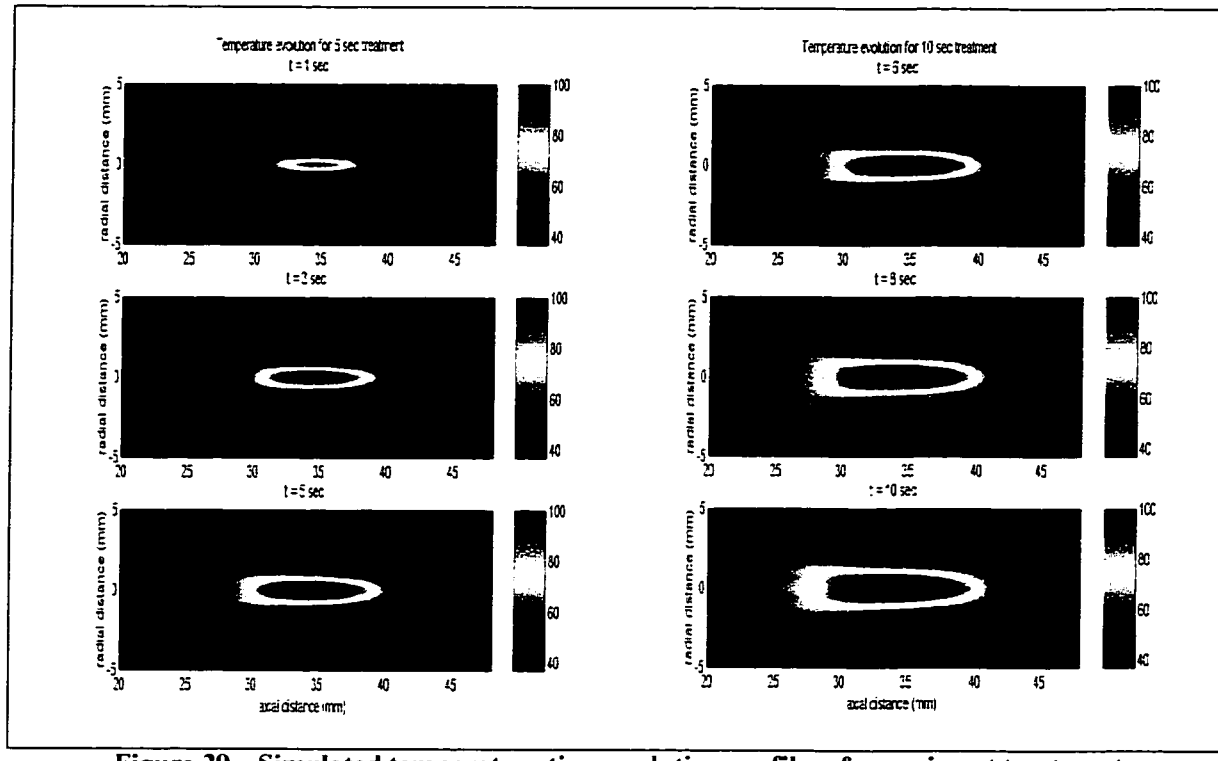

Figure 29 – Simulated temperature time evolution profiles of experiment treatments

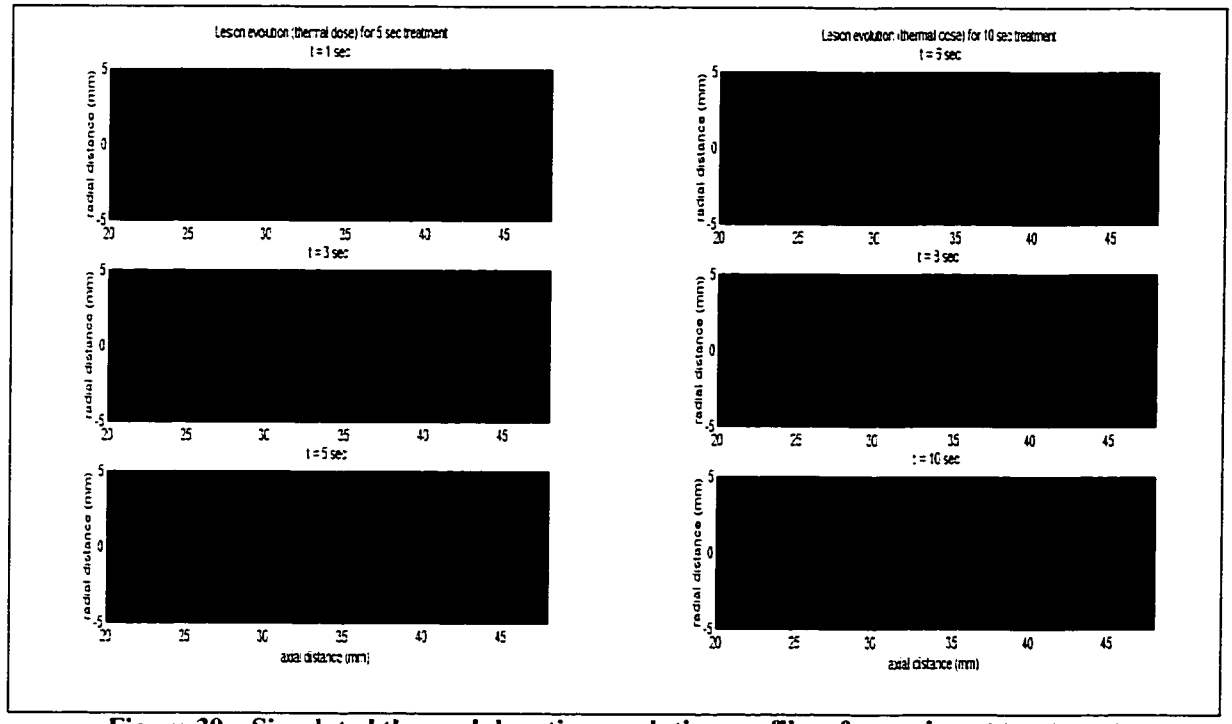

Figure 30 – Simulated thermal dose time evolution profiles of experiment treatments

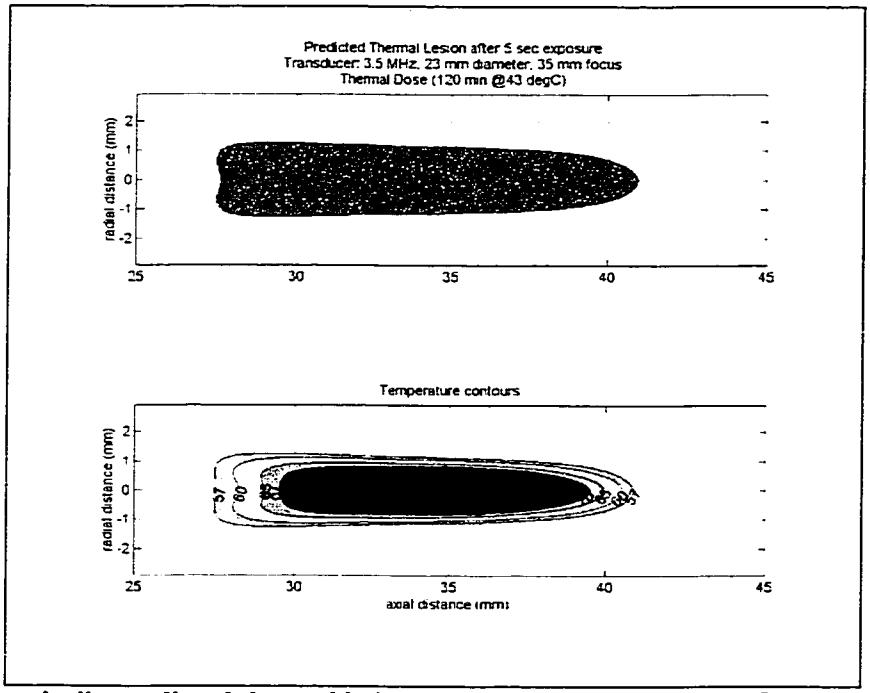

Figure 31 – Numerically predicted thermal lesion and temperature contours. Case 1: 5 seconds HIFU exposure

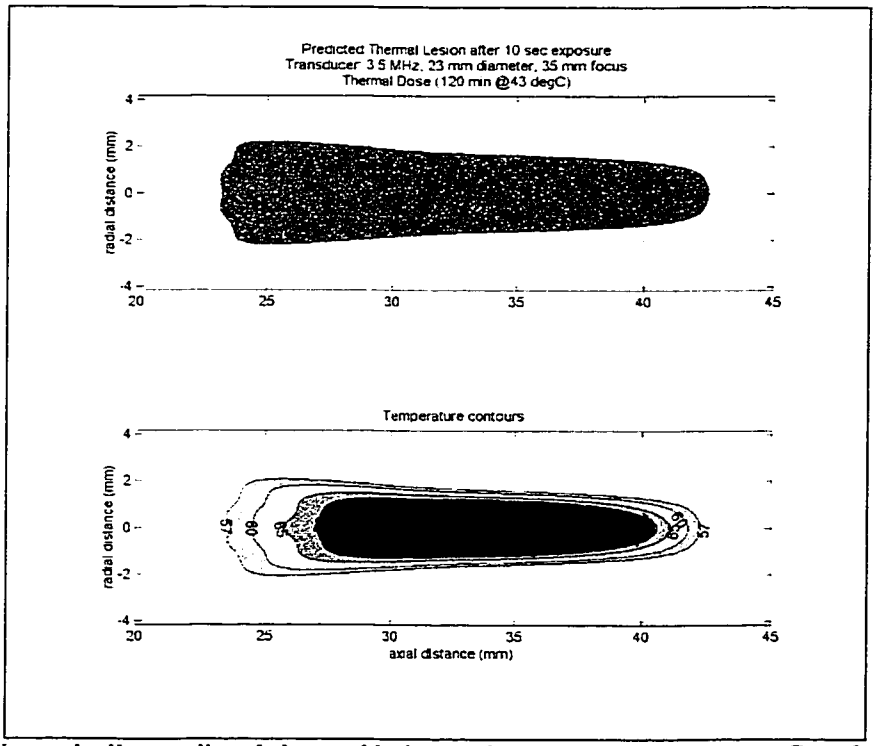

Figure 32 – Numerically predicted thermal lesion and temperature contours. Case 2: 10 seconds HIFU exposure

Table 2– Numerical and experimental lesion dimensions. Comparative analysis at the 95% confidence interval

Lesion after 5 sec exposure Experiments		Lesion after 10 sec exposure Experiments		
Length (mm)	Width (mm)	Length (mm)	Min Width (mm)	Max Width (mm)
13	1.5	19	2.5	3.5
11	2.0	17	2.0	3.5
12	1.5	18	2.2	3.3
11	1.7	17	2.1	3.3
10	1.5	21	2.0	4.2
12	1.8	18	1.9	3.5
9	1.5	22	2.1	4.2
13	2.0	23	2.3	4.3
12	1.6	20	1.9	4.1
13	2.0	21	2.0	4.2
10	1.5	21	2.0	4.2
11	1.7	22	2.0	4.1
95% Confidence Interval	95% Confidence Interval	95% Confidence Interval	95% Confidence Interval	95% Confidence Interval
10.74-12.10	1.58-1.81	18.86-20.97	1.99-2.17	3.67-4.10
Lesion after 5 sec exposure Numerical		Lesion after 10 sec exposure Numerical		
Length (mm)	Width (mm)	Length (mm)	Min Width (mm)	Max Width (mm)
13.34	2.00	19.35	1.97	4.37

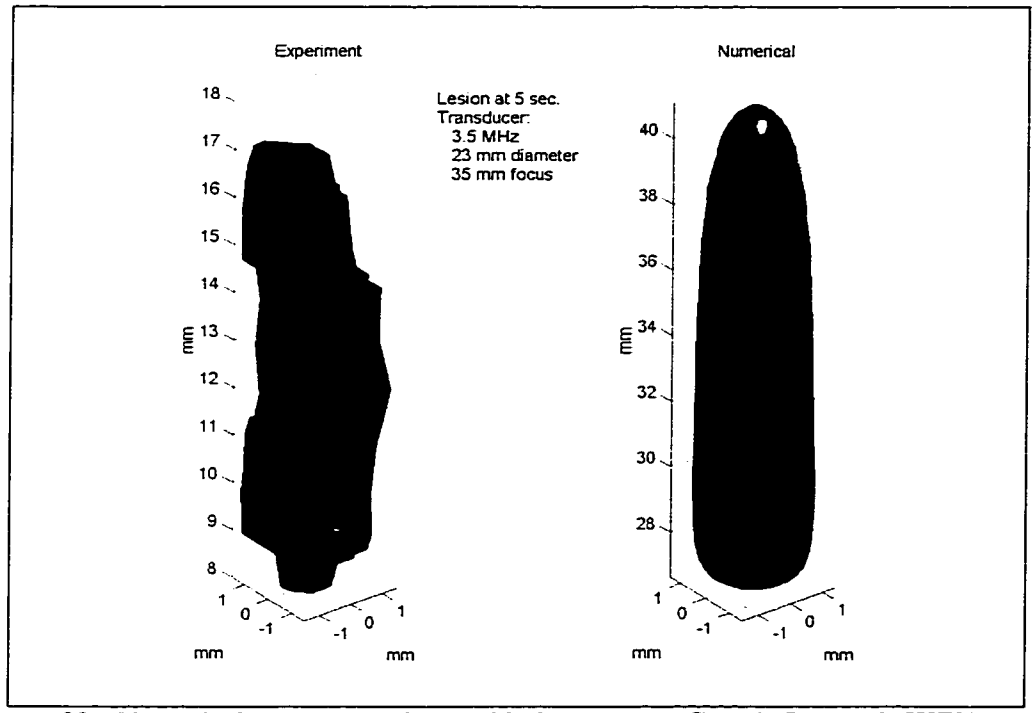

Figure 33 – Numerical versus experimental lesion volume. Case 1: 5 seconds HIFU exposure

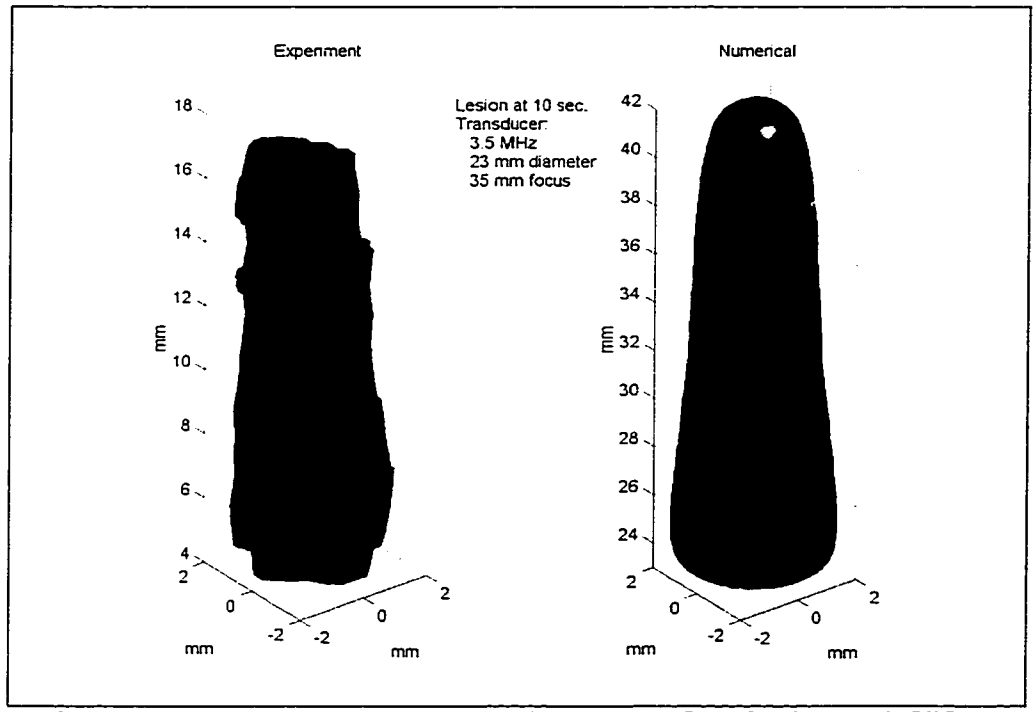

Figure 34 – Numerical versus experimental lesion volume. Case 2: 10 seconds HIFU exposure

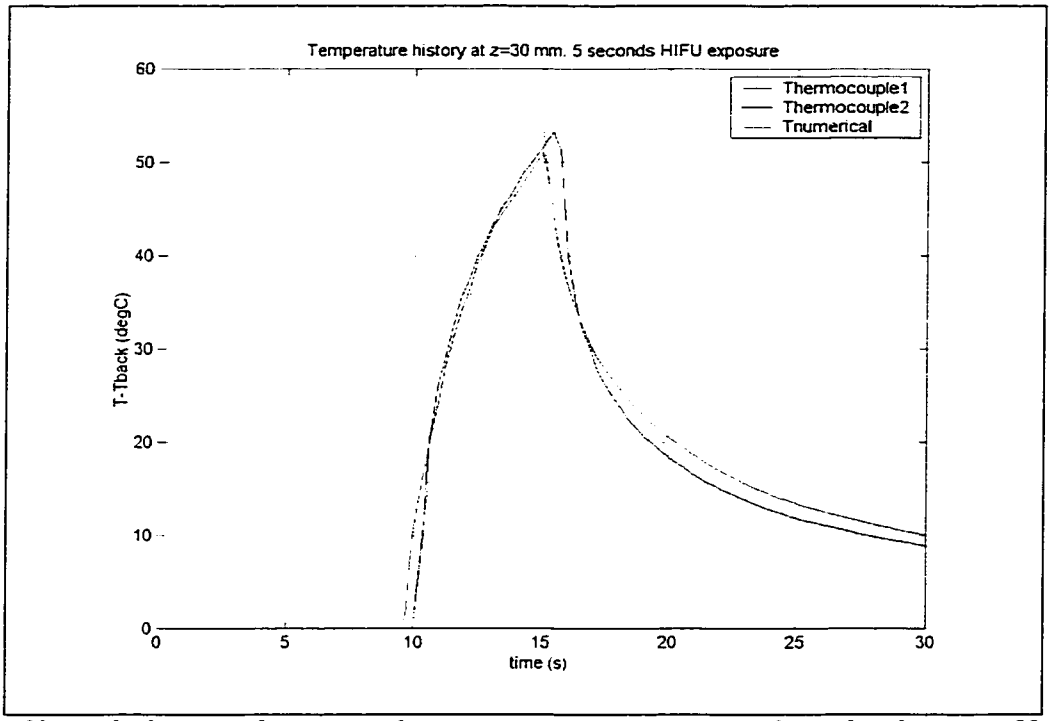

Figure 35 – Numerical versus thermocouple temperature measurement s in turkey breast at 30 mm on transducer axis. Case 1: 5 seconds HIFU exposure

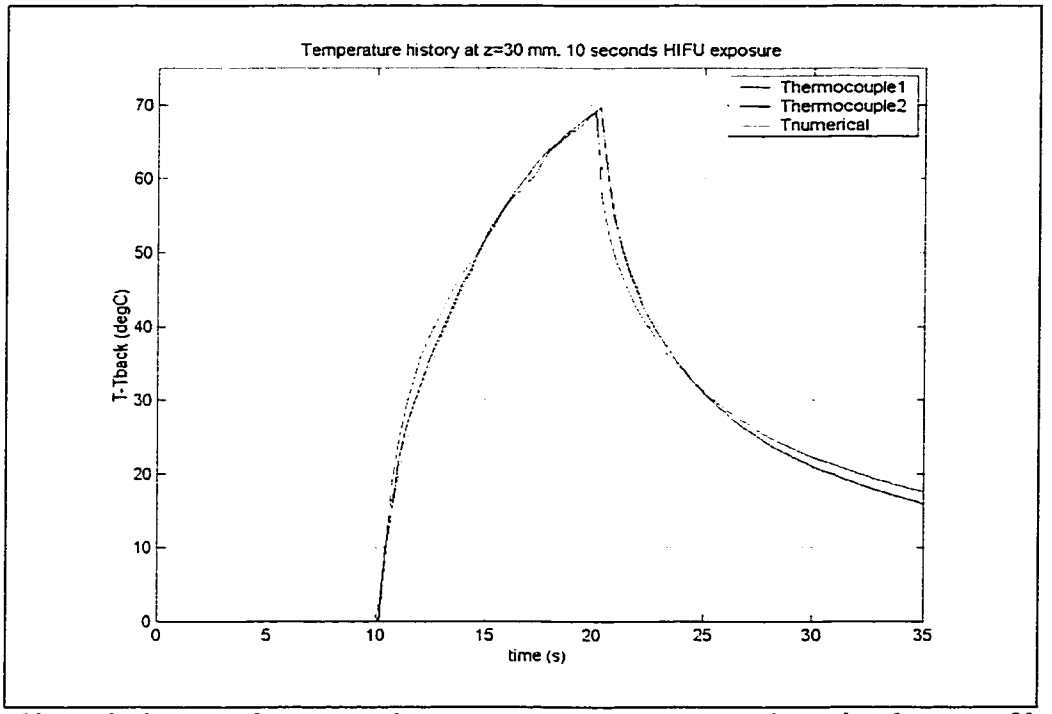

Figure 36 – Numerical versus thermocouple temperature measurement s in turkey breast at 30 mm on transducer axis. Case 2: 10 seconds HIFU exposure

8.5 Selected numerical cases

The numerical results provided in this section refer to the acoustic hemostasis and noninvasive tumor treatment examples described in section 7.3.2.

Results for the acoustic hemostasis case are illustrated in Figures 37 and 38 for two different axial locations of the blood vessel after the transducer is on for 0.35 seconds. As shown in both figures, the blood flow carries the deposited heat away and the temperature inside the vessel hardly increases. As a consequence, a steep temperature gradient is created between the vessel lumina and the surrounding tissue which draws heat away from the tissue. A closer look at the illustrations indeed shows that even when the vessel is in the middle of the focal region, the pseudocolor temperature contours very close to the vessel boundaries indicates a lower magnitude. The advection of heat by the blood also affects the spatial distribution of the temperature in the plane of the flow (x-z plane, lower panels in the figures). In fact, part of the heat carried away by the blood flow, re-enters the tissue by diffusion changing the temperature distribution symmetry.

Temperature and lesion time evolutions in the example case of noninvasive surgery are presented in Figures 39 and 40 for a single exposure. In this model, HIFU treatment is applied for 4 seconds and then stopped. At the high intensity created by this transducer configuration (*cfr.* Figure 17 and 18), the tissue temperature rises very rapidly. Figure 39 in fact shows contours in excess of 150 °C even after one second exposure. However, when the transducer is turned off, the temperature, as expected, quickly decreases although values above 60 °C are maintained up to 5 seconds after insonation is

terminated. This temperature distribution effects the development of the thermal lesion. It is evident from Figure 40 that the lesion continued to spread in width as well as in length (towards the transducer) even after the 4 seconds HIFUexposure. Recalling that thermal dose calculations account for the temperature field history (*cfr.* Sec. 8.2), this result is both logical and expected.

When the region of tissue that needs to be ablated is larger than the specific applicator's focal volume, as is usually the case in reality, either electronic or mechanical scanning is necessary to "paint" the region of interest and treat the whole volume. Electronic scanning is achieved by different phasing of the constituent elements of the array and constantly changes the acoustic field distribution. On the other hand, a single element transducer, which maintains the same acoustic field pattern, can be used in mechanical scanning where the probe itself is mechanically moved. Figure 42 shows the resulting thermal lesion obtained by mechanically moving the same transducer described above by 2 mm steps. In this particular case only three lesions were created with transducer's on/off time respectively of 4 and 12 seconds. It is interesting to notice that first, the three different lesions have merged together and at least axially is difficult to distinguish one from the other. Second, subsequent lesions tend to be bigger than previously created ones suggesting that the 2 mm step in the scanning or the 12 seconds off time are too small to avoid lesion to lesion interaction. In fact, the total lesioned volume is bigger than just the volumetric sum of the individual lesions (Figure 41).

Once again, it has been shown that the developed algorithm model could be an effective investigative mean for treatment planning even for complicated problems.

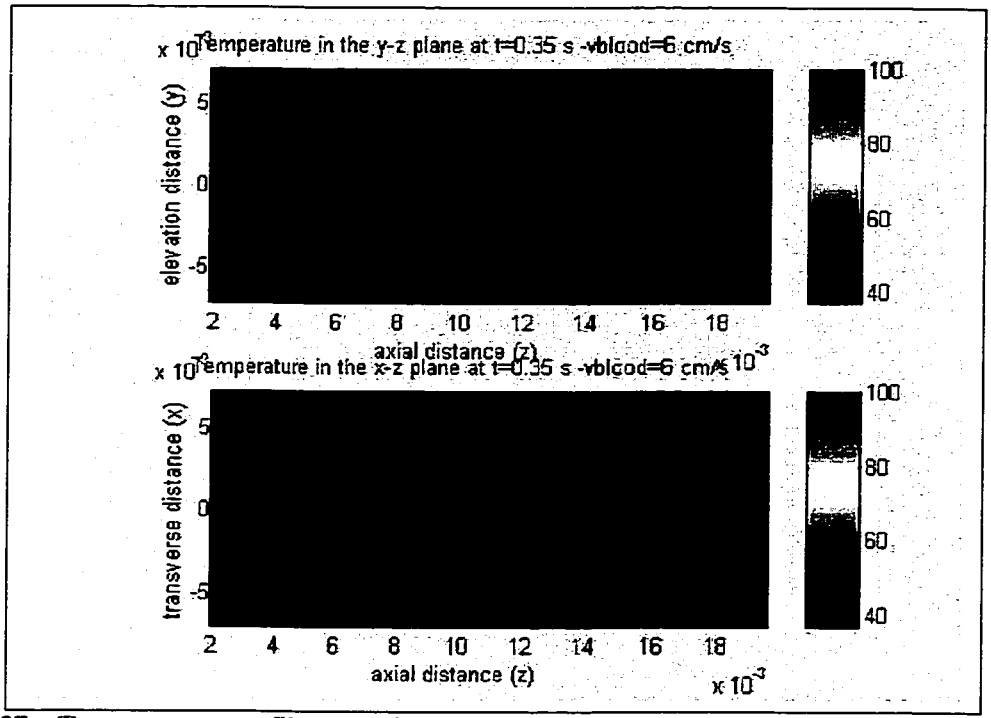

Figure 37 – Temperature profile at t=0.35 seconds in liver in the presence of a 2 mm blood vessel at with 6 cm/s parabolic flow. The vessel is located right before the focal region

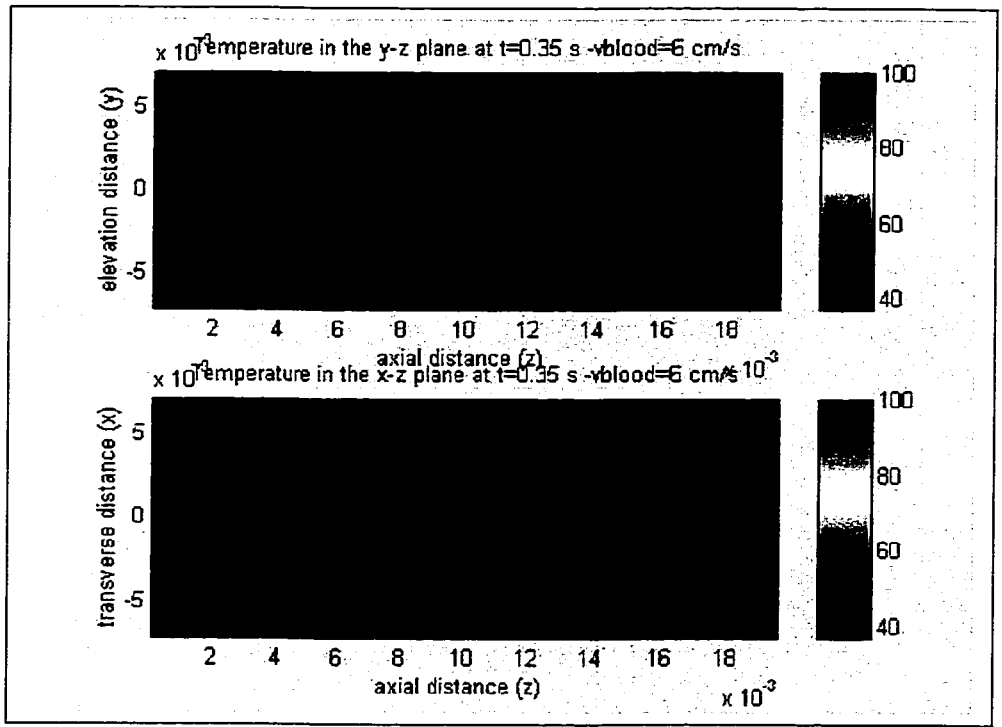

Figure 38 – Temperature profile at t=0.35 seconds in liver in the presence of a 2 mm blood vessel at with 6 cm/s parabolic flow. The vessel is located at the focal region

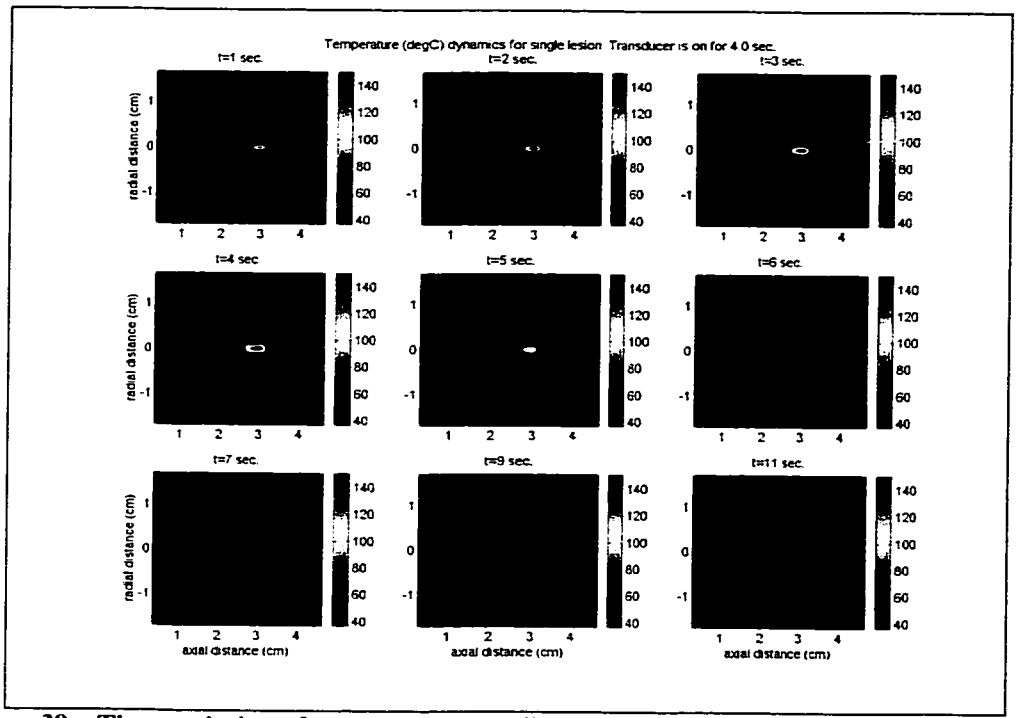

Figure 39 – Time evolution of temperature profiles in a multi-layered model of the prostate. Transducer is on for 4 seconds and then turned off.

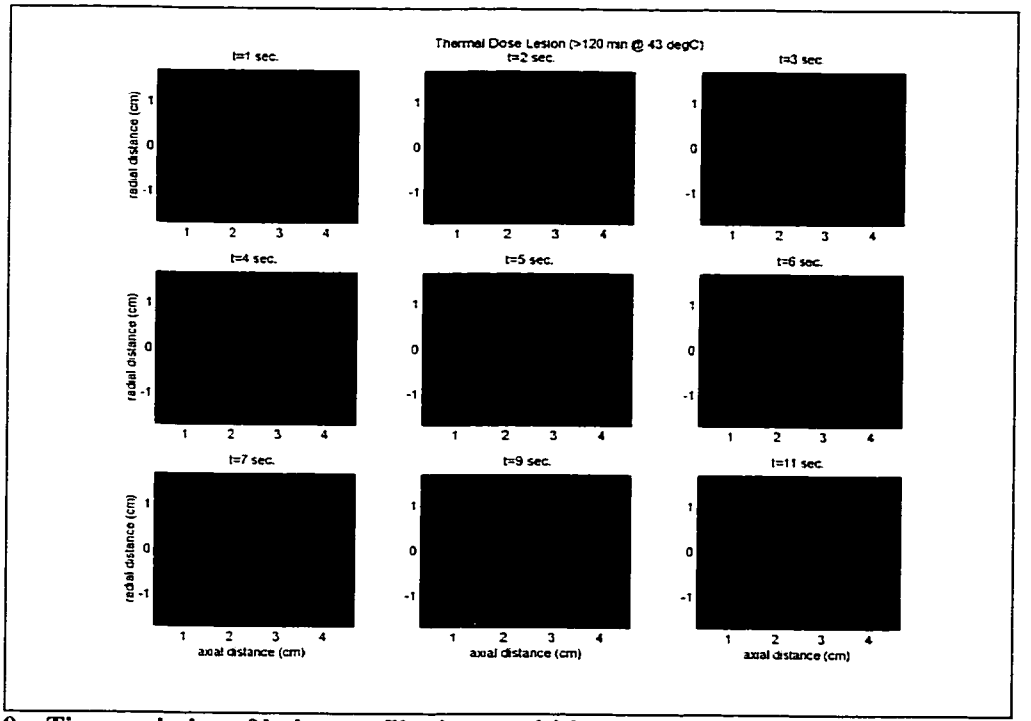

Figure 40 – Time evolution of lesion profiles in a multi-layered model of the prostate. Transducer is on for 4 seconds and then turned off.

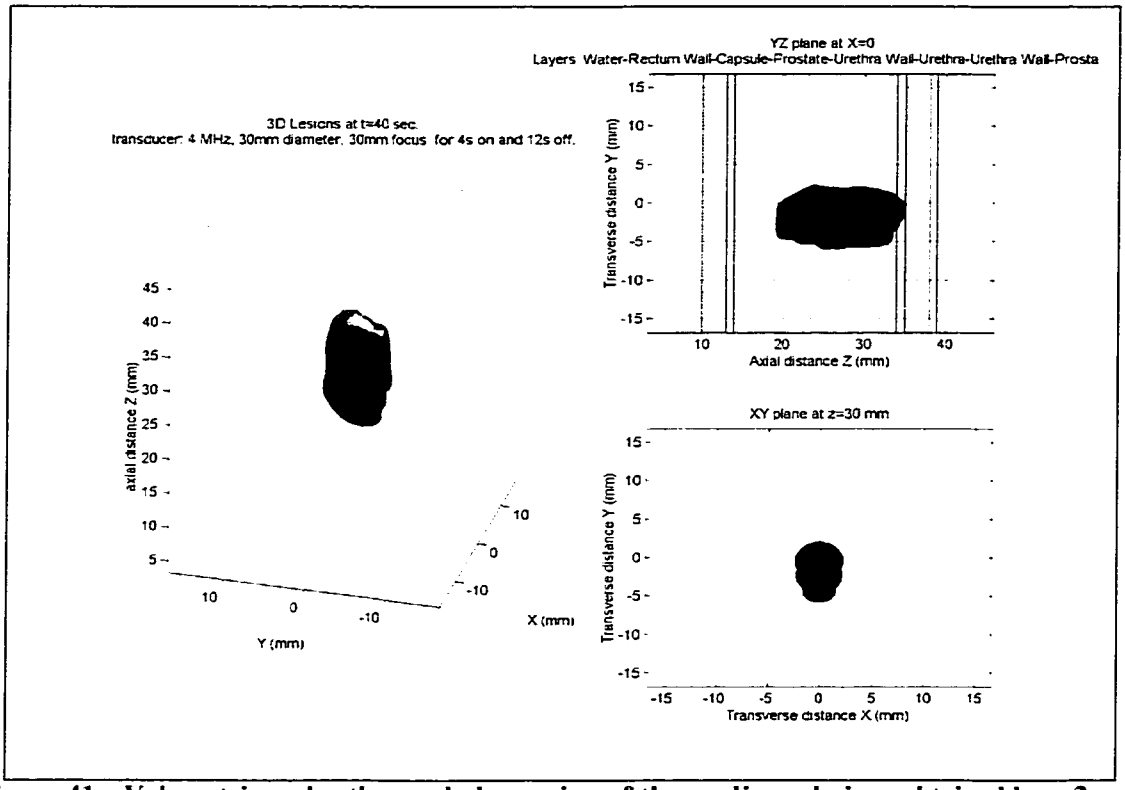

Figure 41 – Volumetric and orthogonal planes view of three adjason lesions obtained by a 2 mm mechanical scanning of the transducer.

CHAPTER 9

Conclusions and Discussion

This dissertation is basically divided into two parts. The first part, Chapter 2 through Chapter 5, is devoted to the conception and development of a computer algorithm that would accurately model ultrasound propagation and its correlated effects in biological media, with special emphasis on high intensity applications. Although the model can be used for diagnostic and imaging purposes, therapeutic ultrasound is the main concern in this document. The algorithm is based on the solution of a generalized, full wave representation of the nonlinear wave equation rigorously derived from first principles for finite-amplitude acoustics coupled to an evolution type bio-heat transfer equation (BHTE) to evaluate temperature rise.

An isentropic equation of state (the source of the quadratic nonlinearity), a continuity of mass, and a conservation law for momentum form a system of first-order partial differential equations that describe acoustic pressure and particle velocity fluctuations in an arbitrarily inhomogeneous medium. Acoustic reflections from material interfaces and generalized scattering are included. Attenuation losses are introduced through N independent relaxation mechanisms, included in the continuity of mass equation, via a time convolution operator applied to the fluid compressibility and acoustic pressure terms. This representation for the acoustic losses grants us the freedom to model arbitrary frequency dependent power laws for attenuation, which are typical of biological tissue, as well as regular thermoviscous losses.

Numerical solutions of finite-amplitude acoustic wave propagation involve several state-of-the-art techniques. A pseudospectral method (PSM) is used to evaluate spatial derivatives through global functions by a fast Fourier transform subroutine and has superior numerical accuracy compared to standard finite difference methods. Contrary to most previous acoustic propagation models where the constitutive equations are combined into a single second-order partial differential equation, here the complete first-order system is maintained in order to apply specific time integration routines and boundary conditions. Time integration is achieved by a fourth-order Adam-Bashforth interpolation on staggered grids (ABS4) where acoustic pressure exists at integer time steps and acoustic particle velocity at half time steps. The ABS4 provides increased accuracy and a greater stability domain compared to standard fourth-order Adam-Bashforth methods. The ABS4, therefore, allows the use of larger time increments in the integration process reducing the overall computational time. Radiation boundary conditions are implemented by perfectly matched layers (PML). The PML drastically reduce, if not eliminate, reflections from the edges of the numerical domain at all angles of incidence thus permitting the use of smaller numerical domains. On the other hand, the BHTE is solved by standard finite-difference techniques. This is possible because of the smoother nature of the partial differential equation and its much larger characteristic time scale compared to the time scale of the acoustic field.

The second part of this dissertation, Chapter 6 through Chapter 8, is mainly devoted to the analysis and validation of the algorithm with discussions on selected

numerical results of practical interest on specific applications of HIFU. The numerical output is compared both to existing analytical solutions and, more importantly, against experimental results. Thermal lesions were created in fresh whole turkey breast in vitro by a 3.5 MHz transducer in a well controlled environment. Two different exposure times have been investigated: a 5 seconds treatment and a 10 seconds treatment in continuous wave at 40 W input power (electrical) to the transducer. The experimental results showed very good agreement with the numerical predictions in term of lesion's length, width and volumetric shape. Furthermore, the algorithm-simulated temperature evolution during treatment was found to fit remarkably well the measured temperature in tissue acquired by needle thermocouples at both exposure protocols.

In conclusion, we have developed a software package, based on strong physics principles, that is accurate in modeling high intensity ultrasound propagation in biological media and its related bioeffects. The acoustic hemostasis and noninvasive ultrasound surgery examples presented in the text further illustrate the capability and versatility of the code to model even very complicated propagation problems that are commonly encountered in real-life HIFU applications. They also underline the usefulness of this software as an investigative tool for both transducer design and treatment protocol planning. Although the main focus of this dissertation was on therapeutic applications of ultrasound, the finite-amplitude wave propagation part of the software can as well be used for imaging and diagnostic purposes.

BIBLIOGRAPHY

Aanonsen, S. I., Barkve, T., Tjotta, N. J., and S. Tjotta, (1984) "Distortion and harmonic generation in the nearfield of a finite amplitude sound beam", *J. Acoust. Soc. Am.*,vol. 75, pp. 749-768

Bacon, D. R., and Carstensen, E. L. (1990), "Increased Heating by Diagnostic Ultrasound Due to Nonlinear Propagation", *J. Acoust. Soc. Am.*,vol. 88, pp. 26-34

Baish, J. W. (1992), "Formulation of a Statistical Model of Heat Transfer in Perfused Tissue", *Advances in Biological Heat and Mass Transfer* Vol. HTD-231, pp. 135-140, ed. J. J. McGrath, New York

Baker, A. C. (1992) "Nonlinear pressure fields due to focused circular apertures", *J. Acoust. Soc. Am.*,vol. 91, pp. 713-717

Bamber and Hill (1979) "Ultrasonic attenuation and propagation speed in mammalian tissue as a function of temperature", *Ultrasound in Med. & Biol.*, vol. 5, pp. 149-157

Berenger, J. P. (1994), "A Perfectly Matched Layer for the absorption of Electromagnetic Waves", *J. Comput. Phys.*, vol. 114, pp. 185-200.

Burgers, J. M. (1948), "A mathematical model illustrating the theory of turbulence", *Advances in Applied Mechanics* 1, pp. 171-199

Canuto, C, Hussani, M. Y., Quarteroni, A. and Zang, T., (1988) *Spectral methods in fluid dynamics*, Springer-Verlag, Ney York

Carcione, J. M., Kosloff, D., and Kosloff, R. (1988), "Viscoacoustic Wave Propagation Simulation in the Earth", *Geophysics*, vol. 53, no. 6, pp. 769-777.

Carstensen, E. L., and Schwan, H. P. (1959), "Absorption of Sound Arising from the Presence of Intact Cells in Blood", *J. Acoust. Soc. Amer.*, vol. 31, pp. 185-189.

Carstensen, E. L., McKay, N. D., Dalecki, D. and Muir T. G. (1982), "Absorption of finite amplitude ultrasound in tissues," *Acustica*, vol. 51, pp. 116-123

Carstensen, E. L. (1987), *Biological effects of transmission line fields*, Elsevier, New York

Chew, W. C. and W. H. Weedon, (1994), "A 3D perfectly matched medium from modified Maxwell's equations with stretched coordinates", *Microwave Opt. Technol. Lett.*, 7, pp. 599-604

Chew, W. C., Jin, J. M. and E. Michielssen, (1997), "Complex coordinate stretching as a generalized absorbing boundary condition", *Microwave Opt. Technol. Lett.*, 15, pp. 363-369

Christopher, T. and K. J. Parker (1991), "New approaches to nonlinear diffractive sound field propagation," *J. Acoust. Soc. Am.*, vol. 90, pp. 488-499

Christopher, T. and Carstensen, E. L. (1996), "Finite Amplitude Distortion and Its Relationship to Linear Derating Formulae for Diagnostic Ultrasound Systems", *Ultrasound in Med. & Biol.*, vol. 22, pp. 1103-1116

Cooley, J. W. and Tukey, J. W., (1965) "Algorithm for the machine computation of complex Fourier series" *Math. Comput.*, vol. 19, pp. 297-301

Damianu C. T., Sanghvi, N. T., Fry, F.J. and Maass-Moreno, R. (1997)."Dependence of ultrasonic attenuation and absorption in dog soft tissue on temperature and thermal dose", *J. Acoust. Soc. Amer.*, vol. 102, pp. 628.

Duck, F. A. (1990). *Physical Properties of Tissue, a Comprehensive Reference Book*. Academic Press. Harcourt Brace Jovanovich, London

Flannery B. P., Press, W. H., Teukolsky S. A. and W. T. Vetterling., (1988) *Numerical Recepiesin Fortran*. Cambridge University Press.

Fornberg, B., (1975) "On a Fourier method for the integration of hyperbolic equations", SIAM *J. Numer.Anal.*, vol. 12, pp. 509-528

Fornberg, B. (1996). *A Practical Guide to Pseudospectral Methods*. Cambridge University Press, New York.

Fornberg, B. (1998). "Calculation of weights in finite difference formulas", SIAM *Rev.*, vol. 40, pp. 685-691

Fry, F. J., Sanghvi, N. T. Foster, R.S. ,Bihrle, R and C Hennige, (1995) "Ultrasound and microbubbles: their generation, detection and potential utilization in tissue and organ therapy – experimental", *Ultrasound in Med. & Biol.*, 21, pp. 1227-1237.

Gerald, C. F. (1980). *Applied Numerical Analysis*. 2nd Ed., Addison-Wesley.

Gottlieb, D. and Orzag, S. A. (1977). *Numerical analysis of spectral methods*. SIAM

Ghrist, M., Fornberg, B. and Driscoll, T. A. (2000)."Staggered time integrators for wave equations", SIAM. *J. Num. Anal.*, vol. 38, pp. 718-741

Hamilton, M. F. and Blackstock, D. T. (1998). *Nonlinear Acoustics*. Academic Press, San Diego.

He, J-Q and Q-H. Liu (1999). "A nonuniform cylindrical FDTD algorithm with improved PML and quasi-PML absorbing boundary conditions", *IEEE Trans. Geoscience and Rem. Sensin.*, vol. 37, no. 2, pp. 1066-1072.

Hutchins, D. A., Mair H. D. and R. G. Taylor (1987). "Transient pressure fields of PVDF transducers", *J. Acoust. Soc. Am.*,vol. 82, pp. 183-192

Hynynen, K. (1987). "Demonstration of Enhanced Temperature Elevation Due to Nonlinear Propagation of Focussed Ultrasound in a Dog's Thigh *in vivo*", *Ultrasound in Med. & Biol.*, vol. 13, pp. 85-91

Lagarias, J. C., Redds, J. A., Wright, M. H. and Wright, P. E. (1998) "Convergence properties of the Nelder-Mead Simplex method in low dimensions", SIAM, *J. Optim.*, vol. 9, pp. 112-147.

Liu, Q-H. and J. Tao, (1997) "The perfectly matched layers for acoustic waves in absorptive media:, *J. Acoust. Soc. Am.*,vol. 102, pp. 2072-2082

Liu. Q-H. (1998). "The Pseudospectral Time-Domain (PSTD) Algorithm for Acoustic Waves in Absorptive Media". *IEEE Trans. Ultrason., Ferroelect., Freq. Contr.*, vol. 45, no. 4, pp. 1044-1055.

Luenberger. D. G., (1973). *Introduction to Linear and Nonlinear Programming*. Addison-Wesley.

Kinsler. L. A., Frey. A. R., Coppens. A. B. and Sanders J. V. (1982) *Fundamentals of acoustics*. John Wiley & Sons. New York

Kreiss H. O., and Oliger. J.(1972) "Comparison of accurate methods for the integration of hyperbolic equations". *Tellus*. vol 24. Pp.199-215

Kunz K.S. and R.J. Luebbers (1972). *Finite difference time domain methods for electromagnetics*. CRC Press Inc., Boca Raton, FL.

Makarov. S. and Ochman. M. (1996)."Nonlinear thermoviscous phenomena in acoustics. Part I". *Acustica*. vol. 82. pp. 579-606

Meaney. P. M., Cahill. M. D. and ter Harr. G. R.,(2000) "The intensity dependence of lesion position shift during focused ultrasound surgery". *Ultrasound in Med. & Biol.*, vol. 26. pp. 441-450

Nachman. A. I., Smith. J. F., and Waag. R. C. (1990). "An Equation for Acoustic Propagation in Inhomogeneous Media with Relaxation Losses". *J. Acoust. Soc. Amer.*, vol. 88. no. 3. pp. 1584-1595.

Nelder. J. A. and Mead. R. (1965). "A simplex method for function minimization". *Computer Journal*. vol. 7. pp. 308-313

Nyborg W. N. (1981) "Heat generation by ultrasound in a relaxing medium". *J. Acoust. Soc. Amer.*, vol. 70. no. 2. pp. 310-312

Nyborg. W. L. (1988). "Solutions of the Bio-Heat Transfer Equation". *Phys. Med. Biol.*,vol. 33. pp. 785-792

O'Donnel. M., Jaynes. E. T., and Miller. J. G. (1981). "Kramers-Kronig Relationship between Ultrasonic Attenuation and Phase Velocity". *J. Acoust. Soc. Amer.*, vol. 69, no. 3, pp. 696-701.

Ozisik. M.N., (1980) *Heat conduction*. John Wiley & Sons, Inc., New York

Papoulis. A. (1991) *Probability, Random Variables, and Stochastic Processes*, McGraw-Hill. New York

Pennes. H. H., (1948) "Analysis of Tissue and Arterial Blood Temperatures in the Resting Human Forearm". *J. Appl. Physiol.*,vol. 2. pp. 93-122.

Pierce. A. D. (1989). *Acoustics: An Introduction to its Physical Principles and Applications.* Acoustical Society of America. New York.

Separeto. S. A. and Dewey. W. C. (1984) "Thermal dose determination in cancer therapy" *J. of Rad. Onc., Biol., and Phys.*, vol. 10, pp. 787-800.

Swindel. W. (1985). "A Theoretical Study of Nonlinear Effects with Focused Ultrasound in Tissue: An 'Acoustic Bragg Peak'". *Ultrasound in Med. & Biol.*, vol. 11, pp. 121-130

Szabo. T.L. (1994). "Time Domain Wave Equations for Lossy Media Obeying a Frequency Power Law". *J. Acoust. Soc. Amer.*, vol. 96, no. 1, pp. 491-500.

Szabo. T.L. (1995). "Casual Theories and Data for Acoustic Attenuation Obeying a Frequency Power Law". *J. Acoust. Soc. Amer.*, vol. 97, no. 1, pp. 14-24.

Taflove A. (1995) *Computational electrodynamics: The finite difference time domain method.* Artech House. Norwood. MA

ter Harr. G. R., Sinnet. D., and I. Rivens. (1989) "High Intensity Focused Ultrasound – A surgical technique for the treatment of discrete liver tumours". *Phys. Med. Biol.* 34. pp. 1743-1750

Tjotta. N J., Tjotta. S., (1987) "Interaction of sound waves. Part I: Basic equations and plane waves." *J. Acoust. Soc. Am.* vol., 89. pp. 1017-1027

Tjotta. N J., Tjotta. S., and E. H. Vefring. "Propagation and intereaction of two collimated finite amplitude sound beams." *J. Acoust. Soc. Am.* **89** 1017-1027 (1990)

Turnbull D. H. and Foster F. S., (1991) " Beam steering with pulsed two-dimensional transducer arrays". *IEEE Trans. Ultrason. Ferroelec. Freq. Contr.*, vol. 38. pp. 320-333

Von Ramm and Smith. (1983) "Beam steering with linear arrays". *IEEE Trans. Biomed. Eng.*., vol. 30. pp. 438-452

Watkin N. A., ter Harr G. R. and Rivens I. H., (1996) "The Intensity Dependence of the Site of Maximal Energy Deposition in Focus Ultrasound Surgery". *Ultrasound Med. Biol.*, vol. 22. pp. 483-491.

Wojcik. G., Mould. J., Ayter. S., and Carcione. L. (1998). "A Study of Second Harmonic Generation by Focused medical Transducer Pulses". *Proc. 1998 IEEE Ultrason. Symposium*, Sendai. Japan.

Yee K.S. (1966) "Numerical solutions of initial boundary value problems involving Maxwell's equations" *IEEE Trans. Antennas Propagat.*, vol. AP-14. pp. 302-307

Yuan. X., Borup. D., Wiskin. J., Berggren. M., Eidens. R..and Johnson. S. A. (1997). "Formulation and Validation of Berenger's PML Absorbing Boundary for the FDTD Simulation of Acoustic Scattering". *IEEE Trans. Ultrason., Ferroelect., Freq. Contr.*, vol. 44. no. 4. pp. 816-822.

Yuan. X., Borup. D., Wiskin. J., Berggren. M., and Johnson. S. A. (1999). "Simulation of Acoustic Wave Propagation in Dispersive Media with Relaxation Losses by Using FDTD Method with PML Absorbing Boundary Condition", *IEEE Trans. Ultrason., Ferroelect., Freq. Contr.*, vol. 46. no. 1. pp. 14-23.

Zing. D. W. "Comparison of high-accuracy finite-difference methods for linear wave propagation", SIAM, *J. Sci. Comput.*, vol. 22, pp.476-502

APPENDIX A

Transducer efficiency: electrical versus acoustic power

The transducer used in the experiments was manufactured by Sonic Concepts, Woodinville, WA. The physical properties of the transducer include a 23 mm diameter aperture with a 35 mm radius of curvature. The central frequency is 3.5 MHz. Force balance measurements were acquired to determine the efficiency of the transducer in converting electrical power to acoustic power. The response of the transducer was found to be linear in the measured range from 0.7 W to 54.7 W with a mean efficiency of about 60 %. Table 3 reports the force balance measurements.

Table 3 – Transducer efficiency measurement as a function of applied electrical power

Electrical Power (W)	Force (mg)	Acoustic Power (W)	Efficiency (%)
0.7	32	0.5	0.664452
3.8	178	2.6	0.680845
8.8	392	5.7	0.647463
14.5	627	9.1	0.628508
20.8	872	12.7	0.609347
27.5	1127	16.4	0.595666
34.2	1364	19.8	0.579695
40.8	1611	23.4	0.573914
47.4	1894	27.5	0.580782
54.7	2225	32.3	0.591227

APPENDIX B

Piston source: uniform distribution of normal velocity versus uniform distribution of pressure

In this Appendix the linear axial beam patterns are derived for a piston source of both a uniform distribution of normal velocity and a uniform distribution of pressure[12]. For simplicity in the mathematics and without loss of generality, this discussion is limited to the case of a baffled plane piston.

The acoustic pressure due to a baffled piston at any point in space can be expressed by the Rayleigh integral

$$p(\mathbf{r}) = \frac{1}{4\pi}\iint [p(\mathbf{r})\nabla_s G(\mathbf{r}_s,\mathbf{r}) - G(\mathbf{r}_s,\mathbf{r})\nabla_s p(\mathbf{r}_s)]\Big|_{z_s=0} \cdot \mathbf{e}_z dx_s dy_s \qquad \text{(B.1)}$$

where the subscript s refers to the source and G is the free field Green's function. Pressure and particle velocity are related by the following linear expression

$$\frac{\partial p}{\partial z} = -\rho_0 \frac{\partial v}{\partial t} = i\omega\rho_0 v \qquad \text{(B.2)}$$

where $e^{-i\omega t}$ time dependence is implied.

Case 1: uniform distribution of normal velocity

In this case $\frac{\partial p}{\partial z} = const$ at the piston and the Green's function takes the form

---

[12] The following discussion is based on notes from Prof. Vera Khokhlova.

$$G(\mathbf{r}_s,\mathbf{r}) = \frac{e^{ikR_1}}{R_1} + \frac{e^{ikR_2}}{R_2} \tag{B.3}$$

with $R_{1,2} = \sqrt{(x_s - x)^2 + (y_s - y)^2 + (z_s \pm z)^2}$, and $k = \frac{\omega}{c_0}$ being the wave number.

Also, the quantity

$$\nabla_s G(\mathbf{r}_s,\mathbf{r}) \cdot \mathbf{e}_z = 0 \tag{B.4}$$

equals zero at z_s=0. Substituting Eqs. B.2-B.4 into Eq. B.1 the magnitude of the pressure on the acoustic axis is

$$|p| = 2p_0 \left| \sin\left(\frac{k\left(\sqrt{z^2 + a^2} - z\right)}{2} \right) \right| \tag{B.5}$$

where a is the piston radius and $p_0 = \rho_0 c_0 v_0$.

Case 2: uniform distribution of pressure

In this case, the Green's function takes the form

$$G(\mathbf{r}_s,\mathbf{r}) = \frac{e^{ikR_1}}{R_1} - \frac{e^{ikR_2}}{R_2} \tag{B.6}$$

with $G = 0$ at z_s=0.

Substituting Eq. B.6 into Eq.B.1 results in

$$|p| = p_0 \left[\left(1 - \frac{z}{\sqrt{z^2 + a^2}} \right)^2 + \frac{4z}{\sqrt{z^2 + a^2}} \sin^2\left(\frac{k\left(\sqrt{z^2 + a^2} - z\right)}{2} \right) \right]^{1/2} \tag{B.7}$$

Figure 42 shows comparative results for different values of *ka*.

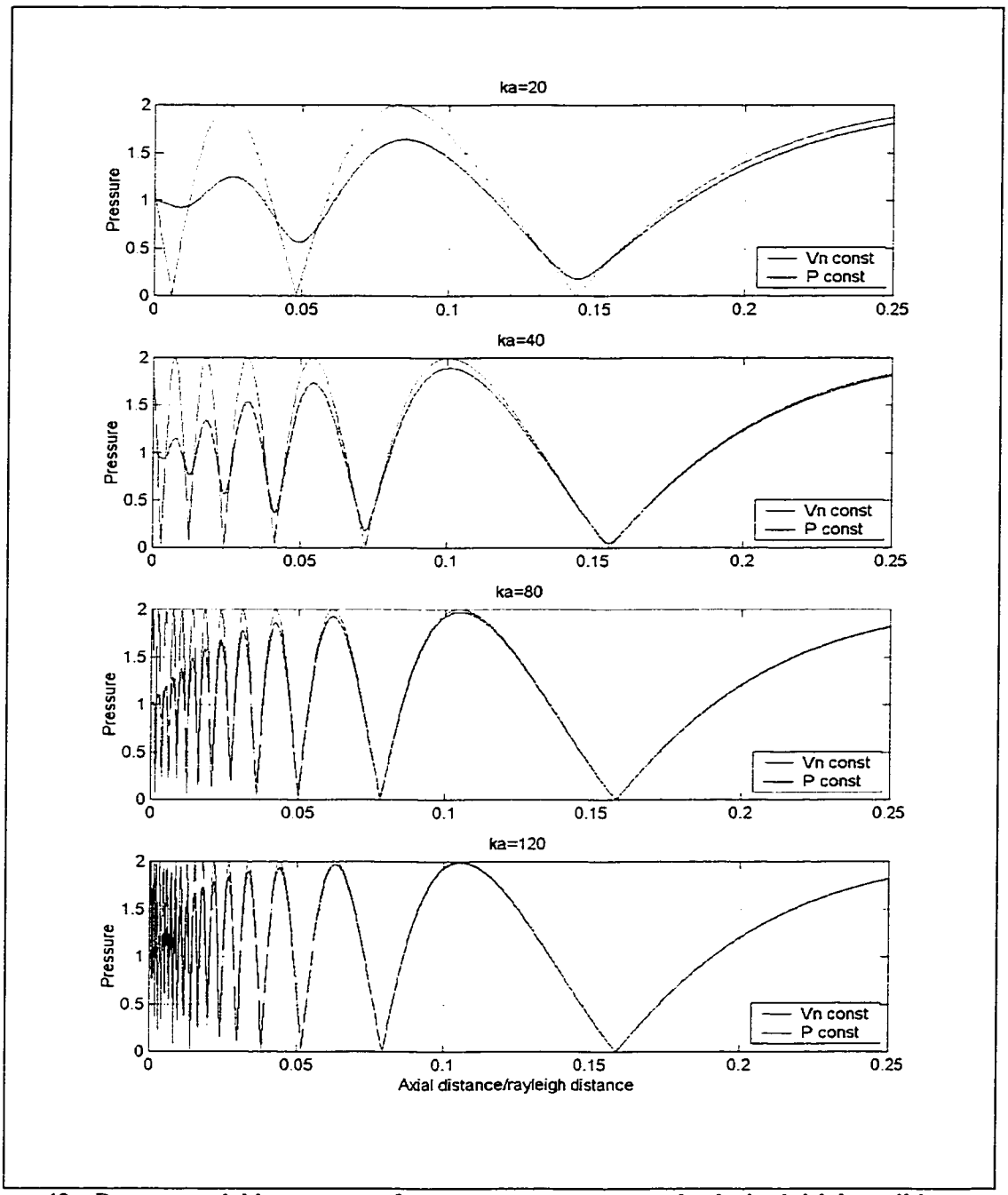

Figure 42 – Pressure axial beam patter for pressure versus normal velocity initial conditions on the transducer face.

VITA

Francesco Pasquale Curra was born in Mileto (VV), Italy, on February 13, 1969. He has lived in Rome most of his life where he graduated from high school. After two years spent at the University of Rome "La Sapienza" enrolled in Electronic engineering, he served the Italian Air Force for one year. He moved to the United States in May 1993 and finished his undergraduate studies at Syracuse University in New York where he earned a Bachelor of Science in Bioengineering in May 1996. In September 1996 he entered the Bioengineering department at the University of Washington to start his doctoral work. Here he joined the Center for Industrial and Medical Ultrasound at the Applied Physics Laboratory.